Coastal and Offshore Science and Engineering

an International
open-access Journal

5/2024
ISSN 2785-7972

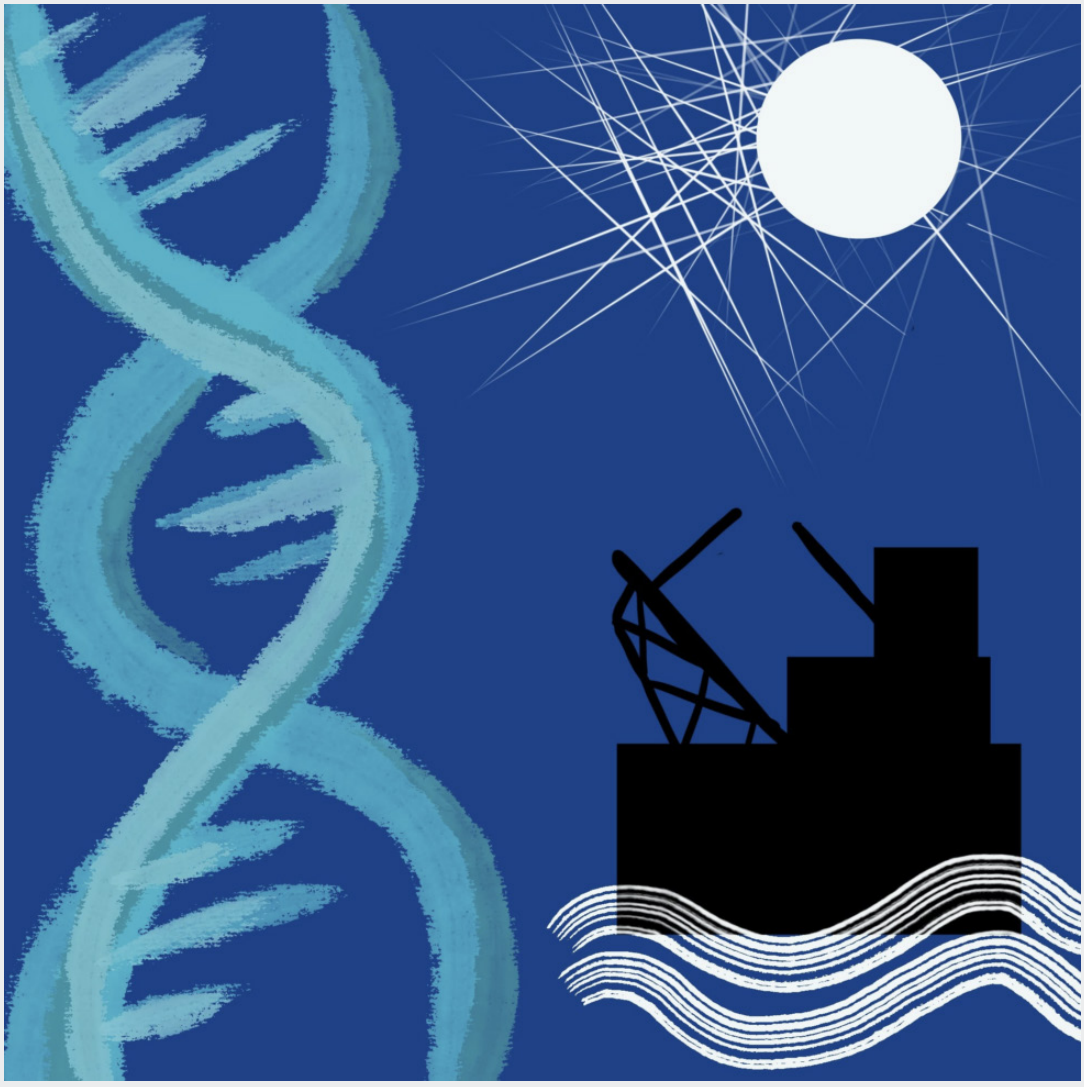

Special Issue of the 11th Short Course/Conference on Applied Coastal Research, Dubrovnik, Croatia
Edited by Roberto Tomasicchio, Felice D'Alessandro, Dalibor Carević and Damjan Bujak

STUDIUM EDITORE
eCAMPUS UNIVERSITÀ
eCAMPUS UNIVERSITY PRESS

COSE

COASTAL AND OFFSHORE SCIENCE AND ENGINEERING

An International open-access Journal

Year III - VOL. 5 - 2024

ISSN : 2785-7972

Coastal and Offshore Science and Engineering is an internationally peerreviewed open access journal of coastal science and engineering published every 6 months online by STUDIUM. Readers of the Journal include engineers, geologists, ecologists, geographers, oceanographers, scholars and specialists who interest in coastal development, ecology, management and protection. The Journal provides new insights on coastal, port and offshore processes, function, design, performance, management, monitoring and restoration from an integrated, multi-/inter- disciplinary, multi-trophic and sustainable perspective. Coastal and Offshore Science and Engineering welcomes research and field case papers based on a wide range of topics by means of field, laboratory and experimental campaigns and remote sensing technology as well as mathematical and numerical modeling. The purpose is to encourage the development and application of holistic initiatives and novel concepts, methods, models and technologies; to elucidate the impact of multiple stressors (climate change, invasive species); to enhance knowledge about the engineering, geology and ecology and integrity of the coastal and offshore systems.

INDEX

Advanced Research for Coastal Infrastructure Resilience, Data-Driven Management, and Sustainable Water Solutions

Coastal and ocean engineering is undergoing a profound transformation. Driven by increasingly frequent extreme events, rising anthropogenic pressures, accelerating climate change, and the transition toward sustainable economies, the discipline is redefining how coastal environments and marine infrastructure are designed, managed, and protected.

This Special Issue of *Coastal and Ocean Science and Engineering* brings together five scientific contributions that address, from different yet complementary perspectives, some of the most pressing challenges faced by contemporary coastal and maritime communities. Collectively, these papers underscore the importance of a multidisciplinary approach grounded in robust physical experimentation, advanced numerical modelling, accessible monitoring technologies, and sustainable environmental solutions.

The articles span a broad thematic spectrum—from wave–structure interaction to coastal monitoring based on open-access datasets; from breakwater damage evolution to advanced modelling frameworks for port navigation safety; and from infrastructure resilience to innovative treatments for environmentally harmful wastewater. Together, they provide a comprehensive snapshot of current scientific progress and offer practical tools for researchers, engineers, planners, and decision-makers.

1. Experimental advances in wave loading on crown walls

Eldrup et al. present an extensive physical modelling study—comprising more than 590 flume tests—investigating the influence of structural permeability and wave steepness on wave-induced loads acting on crown walls. By benchmarking the widely used formulations proposed by Nørgaard et al. and Molines et al., the authors deliver unprecedented insights into their accuracy, applicability, and limitations.

The results substantially expand the experimental database for non-breaking wave conditions, identify areas where existing predictive models require refinement, and provide valuable guidance for future design standards. This contribution represents a significant advancement in the understanding of wave–structure interactions in rubble-mound breakwaters.

2. Data-driven coastal management using open-access datasets

Rumenović et al. introduce a replicable and cost-effective framework for coastal monitoring and countermeasure planning based entirely on publicly available datasets. Developed within the ClimBeach project, the methodology integrates meteorological, oceanographic, and remote-sensing data to assess shoreline evolution, classify beach types, and support the selection of appropriate intervention strategies.

This work is particularly relevant for regions lacking continuous in-situ monitoring infrastructure, offering a scalable and practical pathway toward informed coastal management under increasing climate-driven pressures.

3. Breakwater damage evolution: integrating 2D and 3D insights

Lemos et al. revisit the classical Melby and Kobayashi formulation for damage evolution in rubble-mound breakwaters, extending its applicability to armour layers composed of tetrapods and explicitly incorporating three-dimensional bathymetric effects through large-scale physical model experiments.

The study proposes improved empirical coefficients and demonstrates how interactions between wave fields and three-dimensional structural geometry govern long-term damage progression. The results provide enhanced predictive capabilities for structural resilience assessment and maintenance planning.

4. Integrated modelling for ship accessibility and port safety

Pinheiro et al. propose a comprehensive numerical framework that couples multi-scale wave propagation models with three-dimensional hydrodynamic simulations to evaluate ship motions and under-keel clearance in exposed ports.

The methodology supports both planning-level assessments and real-time operational decision-making and forms the foundation of the SAFEPORT Early Warning System. Its operational application demonstrates how high-resolution modelling can significantly enhance navigational safety, reduce operational disruptions, and strengthen port resilience under challenging sea conditions.

5. Sustainable electrochemical treatment of membrane-cleaning wastewater

Licht et al. investigate electrocoagulation as a sustainable treatment solution for wastewater rich in free chlorine generated during membrane-cleaning procedures in drinking water and desalination plants. Their experimental results demonstrate high removal efficiencies and highlight the conversion of free chlorine into chloride as a key environmental benefit.

This study aligns with global efforts to reduce chemical loads and environmental impacts in water treatment facilities, offering a practical pathway toward greener and more sustainable operational practices.

Collective Themes and Emerging Directions

The contributions gathered in this Special Issue reflect a rapidly evolving discipline, increasingly shaped by the integration of scientific rigor, technological innovation, and sustainability-driven approaches. Across the papers, three overarching themes emerge.

First, experimental and numerical rigor remains fundamental for understanding, modelling, and predicting complex coastal processes—from wave loading mechanisms to interactions between three-dimensional geometries and dynamic wave fields. Second, the rise of data-driven methodologies is democratizing access to coastal monitoring, enabling informed decision-making even in regions lacking dedicated observational infrastructure. Third, the development of sustainable technological solutions is reducing environmental impacts while supporting the transition toward more responsible and resilient operational practices.

Although diverse in scope, these research directions converge toward a shared objective: enhancing the resilience of coastal and maritime systems through innovative, multidisciplinary, and future-oriented approaches.

Concluding Remarks

Taken together, the studies presented in this Special Issue reaffirm the central role of coastal and ocean engineering in protecting, managing, and enhancing coastal environments and marine infrastructure. The integration of high-quality experimentation, robust modelling, open-access data, and sustainable technologies has become a cornerstone for addressing increasingly complex societal and environmental challenges.

This Special Issue is intended not only as an up-to-date scientific reference but also as an invitation to continued interdisciplinary collaboration and innovation, with the ambition of contributing to safer, more adaptive, and more sustainable coastal futures.

Roberto Tomasicchio
University of Salento, Italy

Felice D'Alessandro
University of Milan, Italy

Dalibor Carević
University of Zagreb, Croatia

Damjan Bujak
University of Zagreb, Croatia

DOI: https://doi.org/10.53256/COSE_240101

Influence of Permeability and Wave Steepness on Wave Forces on Crown Walls for Non-Breaking Waves

M. R. Eldrup[a,*], T. Lykke Andersen[a], J. Molines[b] and J. Q. H. Nørgaard[c]
[a]*Department of the Built Environment, Aalborg University, Denmark*
[b]*Universitat Politècnica de València – Research Institute of Transportation and Territory, Spain*
[c]*Coastal Department, Niras, Denmark*

[*]*Department of the Built Environment, Thomas Manns Vej 23, 9220 Aalborg Ø, Denmark, mrel@build.aau.dk*

ABSTRACT: This study investigates how structural permeability and wave steepness affect wave-induced loads on crown walls in rubble mound breakwaters. Evaluating prediction models by Nørgaard et al. (2013) and Molines et al. (2018) against measurements from 591 new physical model tests at Aalborg University revealed that the permeability has minimal impact on the horizontal forces, while influencing significantly the vertical loads and the overturning moment. Nørgaard et al. (2013) and Molines et al. (2018) formulae provide similar agreement against the experimental data for horizontal forces. The Nørgaard et al. (2013) formula is more accurate for predicting base pressures and vertical forces. Both prediction methods show varying accuracy depending on the conditions. The experimental data shows significantly less variation in repetition tests than predicted by the formulae, indicating that further improvements of the formulae can be achieved in future work.

1 INTRODUCTION

Rubble mound structures protect harbours or the hinterland from the sea, with wave overtopping as a key design criterion. The height of the structure is determined by the allowable wave overtopping. Crown walls are commonly incorporated into rubble mound structures to provide a service road on top of the structure, and they may also be used to reduce wave overtopping.

Several studies have investigated wave-induced loads on crown walls; see Pedersen (1996), Martin et al. (1999), Nørgaard et al. (2013), and Molines et al. (2018).

Nørgaard et al. (2013) expanded the applicability of the Pedersen (1996) formulae to depth-limited waves where the wave height distributions might deviate significantly from the Rayleigh distribution. They noted that their formulae may yield unrealistic results for waves with steepness $H_{m0}/L_{m0} < 0.018$, with H_{m0} being the spectral wave height and $L_{m0} = T_m^2 g/(2\pi)$ being the deep-water wavelength calculated with the mean period from zero down crossings at the toe of the structure. Furthermore, they did not test the impact of different structural permeabilities, leaving the applicability of their findings to impermeable structures uncertain.

Molines et al. (2018) conducted tests with wave steepness defined as $H_{m0}/L_{m-1,0} > 0.011$ with $L_{m-1,0} = T_{-1,0}^2 g/(2\pi)$, which slightly expanded the database compared to the work by Nørgaard et al. (2013). However, the effects of very low wave steepness remain unexplored. Additionally, Molines et al. (2018) only examined permeable structures, leaving the applicability of their findings to impermeable structures untested.

The purpose of the present study is thus to investigate the influence of structure permeability and wave steepness on crown wall loading. Waves of lower steepness than those tested previously are also included. The new data is compared against existing formulae. For that purpose, 591 new model tests on rock-armoured mound breakwaters have been conducted at Aalborg University.

First, the formulae by Nørgaard et al. (2013) and Molines et al. (2018) are described, followed by the setup and analysis of new physical model tests. Uncertainties from wave train realisation and armour placement are then examined, before conclusions are drawn and the effects of wave steepness, permeability, and deviations from the formulae are discussed.

2 EXISTING PREDICTION METHODS FOR WAVE LOADS

2.1 *Nørgaard et al. (2013)*

Nørgaard et al. (2013) found that the original formulae by Pedersen (1996) provided reliable estimates of wave-induced loads for non-breaking waves on the foreshore and when armour units fully protected the crown wall. However, for partially unprotected walls and under shallow-water conditions, the loads were found to be overpredicted. Nørgaard et al. (2013) conducted 162 physical model tests on a rock-armoured structure with a front slope of 1:1.5 and a foreshore slope of 1:98.

To characterise the permeability of the tested structure in the present study, the notional permeability defined by Van der Meer (1988) is adopted. Based on the method developed by Eldrup et al. (2019), the notional permeability is estimated as $P \approx 0.4$. The tests consisted of approximately 1,250 waves per test, and the incident wave conditions were generated using a JONSWAP spectrum with a peak enhancement factor of $\gamma = 3.3$. Pressures were sampled at 1,500 Hz and subsequently digitally low-pass filtered to obtain an effective sampling frequency consistent with the spatial resolution of the pressure transducers and the celerity of the peak pressures. A cut-off frequency of 250 Hz was applied.

Nørgaard et al. (2013) also included data from Pedersen (1996), who tested structures with front slopes of 1:1.5, 1:2.5, and 1:3.5. The notional permeability of these structures is estimated to be $P \approx 0.2$. In those tests, the generated waves were likewise based on a JONSWAP spectrum with a peak enhancement factor of 3.3.

Nørgaard et al. (2013) extended the applicability of the original formulae to shallow-water conditions. These modifications included the use of $H_{0.1\%}$ in the run-up formulation, replacing $H_{1/3}$, following the approach proposed by Van der Meer and Stam (1992). In addition, the expressions for slamming pressures acting on the unprotected section of the crown wall and for the overturning moment induced by horizontal wave forces were revised.

The original formulae by Pedersen (1996) for horizontal wave loads, which were also adopted by Nørgaard et al. (2013), are given in Eq. (1). Compared with the original formulation by Pedersen (1996), the mean value (μ) of coefficient $b$and the standard deviations (σ) of coefficients $a$and $b$were updated.

$$
\begin{aligned}
F_{H,0.1\%} &= F_{Hu,0.1\%} + F_{Hl,0.1\%} \\
F_{Hu,0.1\%} &= a\sqrt{\frac{L_{m0}}{G_c}}\, p_m y_{eff} b \\
F_{Hl,0.1\%} &= \frac{1}{2} a\sqrt{\frac{L_{m0}}{G_c}}\, p_m V h_{prot} \\
p_m &= g\rho_w(\mathrm{R}_{u,0.1\%} - A_c) \\
\mathrm{y_{eff}} &= \min\left(\frac{y}{2}, f_c\right) \\
V &= \min\left(\frac{V_2}{V_1}, 1\right)
\end{aligned}
\tag{1}
$$

Here, $F_{\mathrm{H},0.1\%}$ denotes the horizontal force exceeded by 0.1% of the waves. $F_{Hu,0.1\%}$ and $F_{Hl,0.1\%}$ represent the horizontal forces acting on the unprotected and protected parts of the wall, respectively. The mean values and standard deviations of coefficients $a$and b are provided in Table 1. G_c denotes the horizontal width of the armour crest, and A_c is the armour crest freeboard. p_m represents the stagnation pressure, and y is the vertical run-up wedge thickness at the intersection between the front slope and the horizontal crest. f_c is the height of the unprotected part of the wall, and h_prot is the height of the protected part of the wall. y_eff denotes the effective impact zone on the unprotected wall. V_1 and V_2 are illustrated in Fig. 1. $R_\mathrm{u,01\%}$ represents the (fictitious) 0.1% exceedance value for the wave run-up, obtained by assuming an infinitely long slope. All geometric parameters are illustrated in Fig. 1.

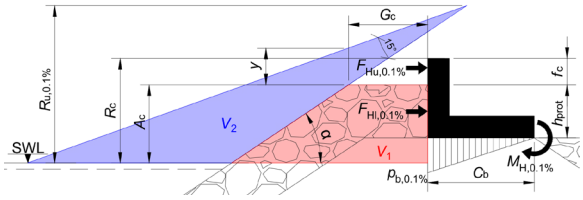

Figure 1. Parameters used in the formulae proposed by Nørgaard et al. (2013) .

The run-up formula originally proposed by Van der Meer and Stam (1992) and reformulated by Nørgaard et al. (2013) is given in Eq. (2). The formulation is subject to an upper limit of $1.388H_{0.1\%}$.

$$
\begin{aligned}
\mathrm{R}_{u,0.1\%} &= \begin{cases} 0.603 H_{0.1\%}\xi_{\mathrm{m0}}, & \xi_{\mathrm{m0}} \le 1.5 \\ 0.722 H_{0.1\%}\xi_{\mathrm{m0}}^{0.55}, & \xi_{\mathrm{m0}} > 1.5 \end{cases} \\
\xi_{\mathrm{m0}} &= \frac{\tan(\alpha)}{\sqrt{H_{1/3}/L_{m0}}}
\end{aligned}
\tag{2}
$$

Nørgaard et al. (2013) also revised the formulation of the horizontal contribution to the overturning moment at the heel of the crown wall, as expressed in Eq. (3).

$$
\begin{aligned}
\mathrm{M}_{H,0.1\%} = F_{Hu,0.1\%}&\left(h_{prot} + \frac{1}{2} y_{eff}\, e_2\right) \\
&+ F_{Hl,0.1\%}\frac{1}{2} h_{prot} e_1
\end{aligned}
\tag{3}
$$

The mean values and standard deviations of coefficients $e_1$and $e_2$are provided in Table 1.

The vertical force acting on the base slab is calculated from the pressure at the front corner, assuming a triangular pressure distribution with zero pressure at the heel. Accordingly, the vertical force can be calculated using Eq. (4).

$$P_{b,01\%} = d\,V\,p_m$$
$$F_{V,0.1\%} = P_{b,01\%}\frac{1}{2}\,C_b \quad (4)$$

where C_b denotes the horizontal length of the base slab, as shown in Fig. 1. The mean value and standard deviation of coefficient d are given in Tab. 1.

Table 1. μ and σ of the coefficients used in the formulae by Nørgaard et al. (2013).

	a	***b***	***d***	***e*₁**	***e*₂**
μ	0.21	1	1	0.95	0.4
σ	0.06	0.81	0.41	0.53	0.78

Assuming normally distributed uncertainty, the 90% confidence interval of the formulae may be estimated as $\mu \pm 1.64\sigma$, based on the values reported in Table 1.

Nørgaard et al. (2013) observed that $F_{H,0.1\%}$ does not necessarily occur simultaneously with $P_{b,0.1\%}$. Consequently, applying the maximum horizontal and vertical forces concurrently is expected to lead to overestimation of the destabilising forces. The overturning moment $M_{H,0.1\%}$ was found to be highly correlated with the moment at the instant of maximum horizontal force.

2.2 *Molines et al. (2018)*

Molines et al. (2018) used 163 experimental tests from Molines (2016) together with 111 tests from Pedersen (1996) to derive new empirical formulae for predicting wave-induced forces acting on crown walls. The tests presented in Molines (2016) comprised breakwaters with a 1:1.5 front slope, armoured with either Cubipods® in one or two layers, or with cubes in two layers. The notional permeability of these structures is estimated to range between $P \approx 0.2$ and $P \approx 0.4$. The foreshore was horizontal in all tests. The generated waves followed a JONSWAP spectrum with peak enhancement factors of 1.0 or 3.3 and had a duration of approximately 1,000 waves. The sampling frequency was 20 Hz.

Several formulae were developed using only the average wave overtopping discharge, q, as input, while other formulations included additional geometric and wave parameters. For the purpose of the present comparison, only the equations based solely on the average overtopping discharge are considered. These are presented in Eq. (5).

$$Fh = \frac{F_{H,0.1\%}}{0.5\rho g C_h^2} = c_1 + 0.6\log(Q)$$
$$Pb = \frac{P_{b,0.1\%}}{0.5\rho g C_h} = c_2 + 0.52\log(Q) \quad (5)$$
$$Mh = \frac{M_{H,0.1\%}}{\rho g C_h^3} = c_3 + 0.11\log(Q)$$

where F_h, P_b, and M_h denote the dimensionless horizontal force, the base pressure at the lower front corner, and the horizontal overturning moment exceeded by 0.1% of the waves, respectively. C_h is the height of the crown wall, and Q is the dimensionless average overtopping discharge, defined as $q/(gH_{m0}^3)^{0.5}$. c_1, c_2 and c_3 are fitting parameters, with mean values and standard deviations provided in Table 2. The remaining parameters are illustrated in Fig. 2.

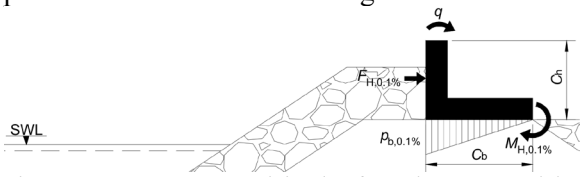

Figure 2. Parameters used in the formulae proposed by Molines et al. (2018).

Table 2. μ and σ values of the coefficients used in the formulae by Molines et al. (2018).

	***c*₁**	***c*₂**	***c*₃**
μ	3.6	4.3	0.7
σ	0.38	0.45	0.09

Regarding the vertical force, assumptions similar to those adopted by Nørgaard et al. (2013) are applied, namely a triangular pressure distribution acting on the base slab. This allows the calculation of both the vertical force and the vertical contribution to the overturning moment about the heel.

Molines et al. (2018) employed the measured average overtopping discharge obtained from the experiments. In cases where these measurements are unavailable, several empirical overtopping formulae were proposed. In the present study, the method developed by Eldrup et al. (2022) is applied to estimate the average overtopping discharge. A comparison between the estimated and measured overtopping discharges is presented in Section 3.2.

3 NEW EXPERIMENTAL DATA

3.1 *Flume layout and test methodology*

A total of 591 small-scale physical model tests were conducted to investigate a wide range of sea state conditions, water levels, and breakwater cross-sections with varying structural permeability. The experiments were carried out at Aalborg University in the Ocean and Coastal Engineering wave flume. The flume features an

active test section, extending from the mean position of the wavemaker to the start of the passive absorption zone, with dimensions of 15 m × 1.5 m × 1.5 m (length × width × height). All tests were performed over a horizontal bathymetry.

Long-crested irregular waves were generated using the second-order wavemaker theory proposed by Schäffer (1996), incorporating the modifications suggested by Eldrup and Lykke Andersen (2019a). For sea states for which the applicability criteria of Eldrup and Lykke Andersen (2019a) indicated that second-order theory was unsuitable, the ad hoc unified wavemaker approach proposed by Zhang et al. (2007) was applied. The input conditions for this method were derived from simulations performed with the Celeris model developed by Tavakkol and Lynett (2017), a numerical Boussinesq-type wave model. For all sea states, the target wave spectrum was defined using a JONSWAP spectrum with a peak enhancement factor of 3.3. Active wave absorption at the wavemaker, effective for both linear and nonlinear waves, was employed throughout the test programme (Lykke Andersen et al. (2016), (2018)). Wave generation and control were managed using the AwaSys 7 software developed by Aalborg University (2023a). Surface elevations were measured using resistance-type wave gauges manufactured by VTI. A total of 11 wave gauges were installed along the flume; however, only the seven gauges closest to the breakwater were used to estimate the incident wave conditions. Incident and reflected wave components were separated using the method described by Eldrup and Lykke Andersen (2019b). All wave data processing and analysis were performed using the WaveLab software developed by Aalborg University (2023b).

The duration of each test was adjusted according to the sea state, such that approximately 2,000 waves were generated in order to obtain reliable estimates of low exceedance wave loads. The experimental programme included six different target peak wave steepness values, s_{0p}, defined using the deep-water wavelength calculated from the peak period $T_p$and the spectral significant wave height H_{m0}. The selected peak wave steepness values were $s_{0p} = 0.005$, 0.007, 0.010, 0.020, 0.030, and 0.045. This corresponds to a range of H_{m0}/L_{m0}between 0.007 and 0.057, and $H_{m0}/L_{m-1,0}$between 0.005 and 0.050. Non-breaking wave heights in the range $H_{m0} = 0.06$–0.14 m were generated, depending on the stability constraints of the tested structures.

3.2 *Tested breakwaters*

Breakwaters with front slopes of 1:1.5 and 1:3 were tested at three different water levels, both with and without an unprotected section of the crown wall. Not all possible combinations of slope, water level, and wall configuration were investigated.

Figure 3 illustrates the geometrical dimensions of the tested breakwaters together with the corresponding tested water levels. Tests including a detachable section of the crown wall—i.e. with armour placed below the wall crest—were conducted at a water level of 86 mm. Tests without this detachable section, corresponding to configurations in which the armour crest and the crown wall crest were at the same elevation, were performed at water levels of 0 mm and 42 mm.

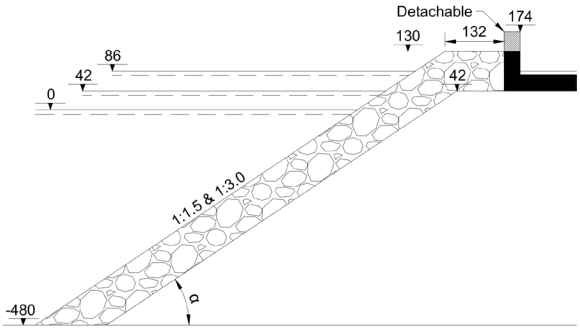

Figure 3. Breakwater dimensions and tested water levels. Measurements are given in millimetres at model scale.

Five different layer compositions were tested, as shown in Fig. 5. The majority of the experiments were carried out on the least permeable (Model A) and the most permeable (Model E) cross-sections, corresponding to notional permeability values of $P = 0.1$and $P = 0.5$, respectively, as defined by Van der Meer (1988). The notional permeability of the remaining cross-sections was estimated. In addition to Model A, an impermeable structure with a thicker filter layer and an estimated notional permeability of $P \approx 0.2$was tested (Model B). A structure with an estimated permeability of $P \approx 0.4$was also examined (Model D), as well as another structure with $P \approx 0.4$but incorporating a slightly finer core material than that proposed Van der Meer (1988) (Model C). Most tests were conducted with a fully protected crown wall ($R_c = A_c$), while a smaller subset of tests included crown walls that were not fully covered by rock armour ($R_c > A_c$).

Models A and E with a front slope of 1:1.5 were each tested six times, with the armour layer rebuilt prior to each test in order to assess the influence of armour stone placement and random

orientation. The same procedure was applied for the 1:3 front slope, although only three repetitions were performed for Model A and two for Model E. In addition, Model E with a front slope of 1:1.5 was tested using five different realisations of the wave train without rebuilding the armour layer, to investigate the influence of wave train variability.

Table 3. Range of tested conditions measured for each model.

Model	cot(α)	$H_{m0}/L_{m-1,0}$	H_{m0}/h	$h/L_{m-1,0}$	R_c/H_{m0}
A	1.5	0.005-0.050	0.10-0.23	0.02-0.46	0.84-1.95
A	3.0	0.005-0.050	0.11-0.30	0.02-0.43	0.69-1.55
B	1.5	0.005-0.049	0.10-0.22	0.02-0.46	0.88-1.72
C	1.5	0.005-0.049	0.11-0.26	0.02-0.43	0.88-1.53
D	1.5	0.005-0.049	0.10-0.26	0.02-0.46	0.86-1.55
E	1.5	0.005-0.049	0.11-0.26	0.02-0.43	0.88-1.56
E	3.0	0.005-0.049	0.15-0.26	0.02-0.32	0.80-1.54

Figure 4 presents a comparison between measured average overtopping discharges and predictions obtained using the method proposed by Eldrup et al. (2022). The results indicate no significant differences in dimensionless average overtopping among the investigated cross-sections. Consequently, a roughness factor of $\gamma_f = 0.40$is adopted for all tested configurations. Nevertheless, further research is required to quantify the detailed influence of structural permeability on the average overtopping discharge.

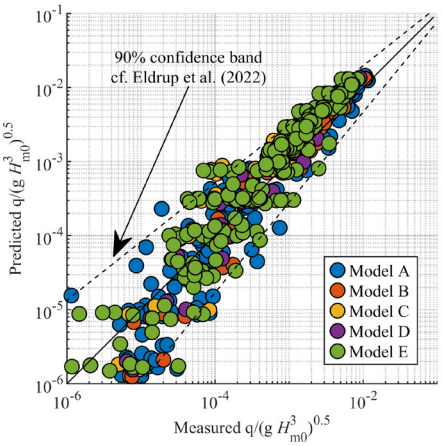

Figure 4. Comparison between measured average overtopping discharge and predictions by Eldrup et al. (2022), applying $\gamma_f = 0.40$.

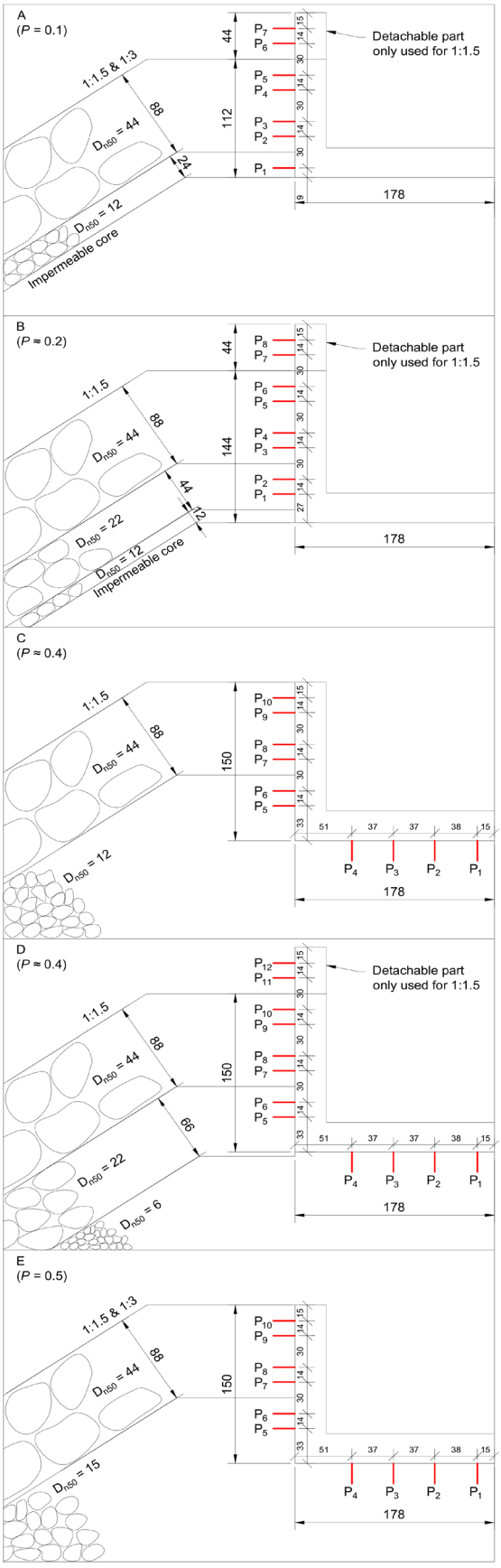

Figure 5. Layer composition of the tested breakwaters and crown wall configurations. Measurements are given in millimetres at model scale. Red lines indicate the locations of pressure transducers.

3.3 *Wall layout*

Depending on the tested breakwater configuration, between 10 and 24 Drück PMP UNIK pressure transducers with flush-mounted membranes were used to measure the pressure distribution acting on the crown wall. The pressure transducers were arranged in two adjacent vertical sections, allowing two sensors to be installed at each elevation. This configuration provides measurement redundancy and accounts for variability associated with armour stone placement. The locations of the transducers in both the fixed wall and the detachable wall sections are illustrated in Fig.5 for a representative column. The transducers have a diameter of 20 mm and a frequency response of up to 5 kHz.

3.4 *Load analysis*

In the present experiments, pressures were sampled at a frequency of 1,000 Hz. To reduce high-frequency noise and spurious pressure spikes, a moving-average filter was applied to the pressure time series, following the approach described by Lamberti et al. (2011). The smoothing window was fixed at 0.01 s for all tests. This filtering procedure effectively attenuates rapid fluctuations while preserving the impulsive pressure components of the signal.

A median filter was subsequently applied to minimise the effects of slow signal drift, using a window size of 20 s. In addition, the median filter removes the hydrostatic pressure component in tests where the transducers were fully submerged, thereby isolating the wave-induced pressure in the measurements. The combined effect of the two filtering procedures is illustrated in Fig. 6.

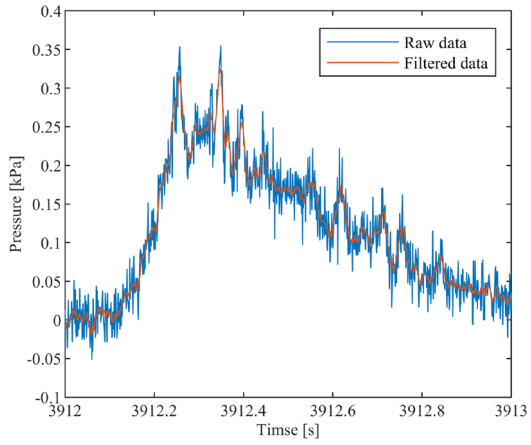

Figure 6. Example of pressure time series recorded by a single transducer before and after filtering.

The filtered pressure values were extrapolated to the edges of the crown wall, and a linear pressure variation was assumed between adjacent transducers. The resulting pressure distributions were then integrated to determine the forces and moments acting on the crown wall. The analysis procedure adopted in the present study is identical to that used by Nørgaard et al. (2013).

4 UNCERTAINTY RELATED TO SEA STATE REALISATION

The influence of wave train realisation is illustrated in Fig. 7. Six different random wave seeds were used to generate distinct sea state realisations, each comprising approximately 2,000 waves. The tests were performed on Model E with a front slope of 1:1.5. The selected wave conditions were chosen such that the estimated damage to the armour layer, calculated according to Van der Meer (1988), satisfied $S_d < 1$. This ensured that rearrangement of the armour layer was limited and did not influence the experimental results. The applied significant wave height was $H_{m0} = 0.08$m, and the water level was set to 0 mm.

The figure presents subplots of the dimensionless horizontal wave force, the base pressure at the lower front corner, the 0.1% exceedance wave height $H_{0.1\%}$, and the spectral significant wave height H_{m0}. Solid lines indicate model predictions together with their associated 90% confidence bands. While $H_{0.1\%}$ exhibits noticeable variability between different realisations, H_{m0} remains relatively stable, leading to differences in the predicted wave-induced loads.

For the horizontal force, the experimental data fall within the confidence bands of both prediction methods, although the confidence band associated with Molines et al. (2018) is noticeably wider. On average, the formulation by Nørgaard et al. (2013) underpredicts the measured horizontal forces by approximately 25%, whereas the formulation by Molines et al. (2018) overpredicts them by approximately 40%, with the experimental data showing closer agreement with the predictions of Nørgaard. For the base pressure at the lower front corner, both prediction methods overestimate the measured values. The formulation by Nørgaard et al. (2013) overpredicts the base pressure by approximately 50%, although the measurements remain within its 90% confidence interval. In contrast, the formulation by Molines et al. (2018) overpredicts the base pressure by approximately 150%, with the measurements lying outside the

corresponding confidence band. Both models reproduce the general trend of increasing load with decreasing wave steepness; however, the experimental data are systematically shifted relative to the mean model predictions.

Tab. 4 presents the coefficient of variation (σ/μ) for both the experimental data and the corresponding model predictions shown in Fig. 7. The variability observed in the experimental data is small compared with the width of the confidence bands associated with the prediction formulae. This suggests that the uncertainty of the prediction methods primarily originates from factors other than wave train realisation. With approximately 2,000 waves per test, the duration of the experiments is therefore considered sufficient to assess the influence of wave steepness and structural permeability.

Table 4. Coefficient of variation (σ/μ) for experimental data and prediction formulae shown in Fig. 7.

$s_{m-1,0}$	0.048	0.036	0.024	0.012	0.008	0.006
Fh_{data}	0.06	0.11	0.03	0.07	0.07	0.06
$Fh_{Molines}$	0.40	0.30	0.25	0.20	0.18	0.17
$Fh_{Nørgaard}$	0.29	0.29	0.29	0.29	0.29	0.29
Pb_{data}	0.06	0.06	0.03	0.05	0.03	0.02
$Pb_{Molines}$	0.22	0.20	0.18	0.16	0.15	0.15
$Pb_{Nørgaard}$	0.41	0.41	0.41	0.41	0.41	0.41

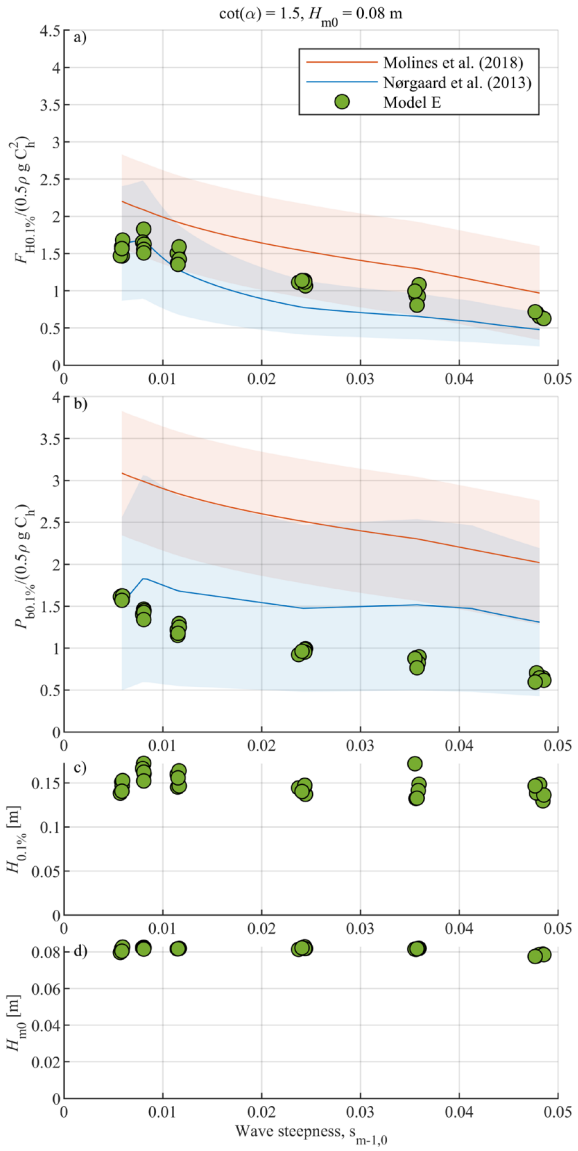

Figure 7. Influence of different wave train realisations on measured and predicted loads. Wave heights are given at model scale.

5 UNCERTAINTY RELATED TO RANDOM ARMOUR PLACEMENT

The influence of random armour placement is illustrated in Fig. 8. Experiments involving random positioning and orientation of the armour stones were conducted through six independent rebuilds of the armour layer and are analysed here for Model E with a front slope of 1:1.5. The influence of armour placement is important because pressure transducers may be fully, partially, or not covered by armour stones, thereby affecting the measured pressure signals. Rearrangement of the rubble mound, and consequently the pore structure in front of the crown wall, is therefore conceptually similar to

altering the relative position of the pressure transducers. This effect is particularly relevant when the characteristic size of the armour stones is large compared with the diameter of the pressure transducers.

As the number of pressure transducers increases, the mean load estimates are derived from a larger set of measurements, and the influence of local variations in armour placement is expected to diminish.

Figure 8 presents the dimensionless horizontal force and base pressure together with the corresponding wave heights, in a manner analogous to Fig. 7. The results show values comparable to those observed in Fig. 7 , although with a slightly increased scatter. Nevertheless, the conclusions drawn from the analysis of Fig. 7 also apply to the observations presented in Fig. 8.

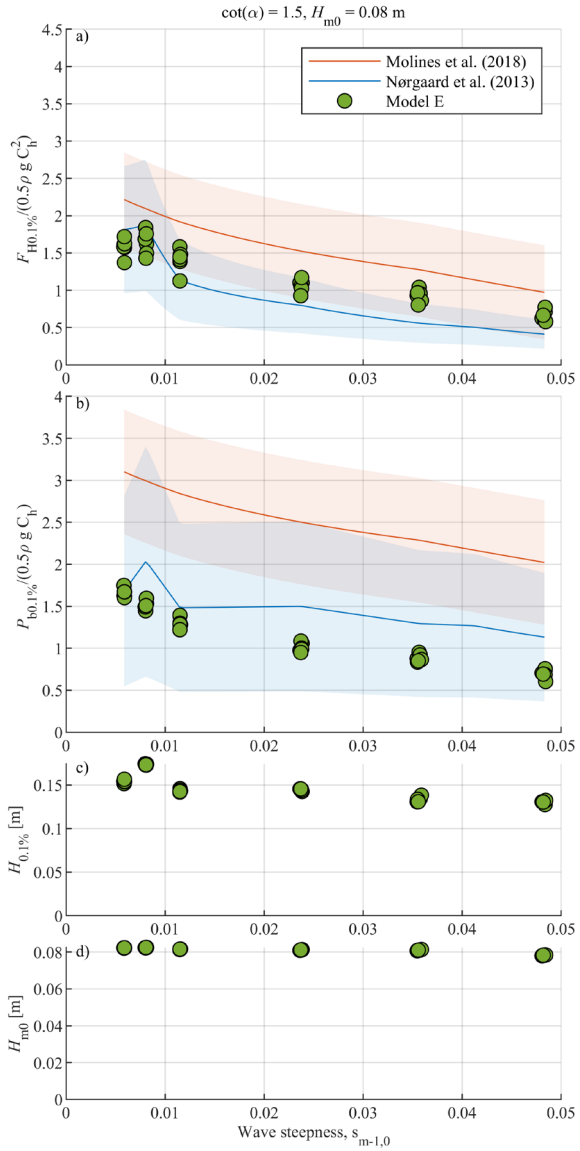

Figure 8. Influence of random armour placement on measured and predicted loads. Wave heights are given at model scale.

Tab. 5 summarises the coefficients of variation (σ/μ) for both the experimental data and the prediction formulae illustrated in Fig. 8. Similar to the influence of wave train realisation, the variability observed in the experimental data is significantly smaller than that predicted by the empirical formulae. This indicates that the uncertainty associated with random armour placement is minor compared with the overall uncertainty inherent in the prediction methods. It is therefore concluded that the spatial resolution and number of pressure transducers are sufficient to reliably capture the effects of wave steepness and structural permeability.

Table 5. Coefficient of variation (σ/μ) for experimental data and prediction formulae shown in Fig. 8.

$s_{m-1,0}$	0.048	0.036	0.024	0.012	0.008	0.006
Fh_{data}	0.11	0.09	0.08	0.11	0.10	0.07
$Fh_{Molines}$	0.39	0.30	0.25	0.20	0.18	0.17
$Fh_{Nørgaard}$	0.29	0.29	0.29	0.29	0.29	0.29
Pb_{data}	0.08	0.05	0.05	0.05	0.04	0.03
$Pb_{Molines}$	0.22	0.20	0.18	0.16	0.15	0.15
$Pb_{Nørgaard}$	0.41	0.41	0.41	0.41	0.41	0.41

Uncertainty associated with armour placement and wave train realisation has a smaller influence on the base pressure than on the horizontal force, as reflected by the lower coefficients of variation. Consequently, the vertical force is also less sensitive to these sources of uncertainty than the horizontal force.

6 INFLUENCE OF CORE PERMEABILITY WITH A FULLY PROTECTED WALL

Fig. 9 illustrates the effect of breakwater core permeability on wave-induced loads. The characteristic crown wall heights, C_h, are 112 mm for Model A, 144 mm for Model B, and 150 mm for the remaining structures; the latter value is also adopted in the formulae proposed by Nørgaard et al. (2013). Model A, which has an impermeable core, exhibits the highest non-dimensional horizontal forces, although it also has the smallest value of C_h. Model B, which is likewise impermeable but has a wall height comparable to the other structures, shows horizontal force levels similar to those of the permeable configurations.

For models with comparable wall heights, the magnitudes of the horizontal forces are nearly identical, indicating that core permeability has a negligible influence on the horizontal wave load. Instead, the results suggest that normalisation with C_h^2 is not fully appropriate, as the measured pressure distributions deviate from the assumed

triangular shape. Since the use of smaller C_h values in the formulation by Nørgaard et al. (2013) results in larger non-dimensional forces—consistent with the experimental observations—the wall height is more appropriately represented in the formulation by Nørgaard et al. (2013) than in that of Molines et al. (2018). The fundamental difference between the two approaches lies in the assumed pressure distribution: Nørgaard et al. (2013) adopt a rectangular distribution, whereas Molines et al. (2018) assume a triangular distribution.

A similar conclusion regarding the assumed pressure distribution can be drawn for the base pressure (see Fig 9b), as Model A yields larger values than the remaining structures. Nevertheless, an effect of core permeability can be observed, as Model B tends to exhibit higher base corner pressures than the permeable structures. For the permeable configurations, a reduction of approximately 30% in the base pressure is observed compared with the impermeable structures. This reduction is attributed to the ability of the pressure at the front base corner to dissipate beneath the crown wall in permeable structures. This pressure reduction is a localised effect and does not appear to significantly influence the horizontal force, provided that the wall height is sufficiently large.

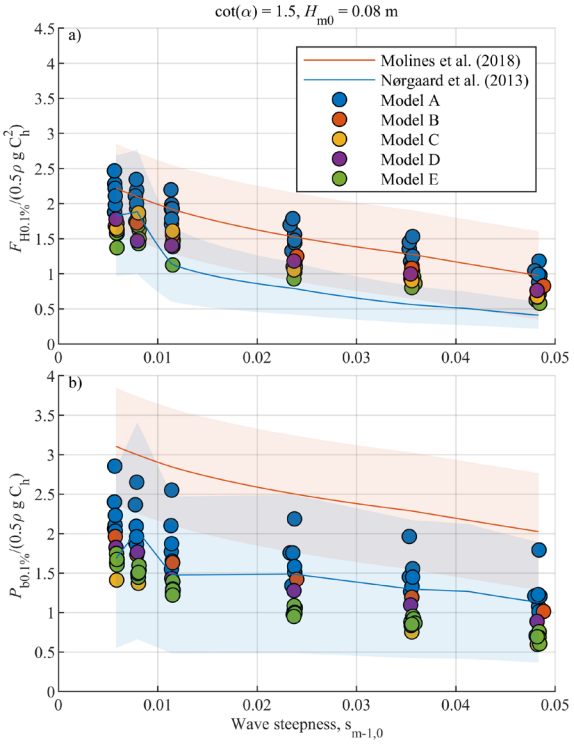

Figure 9. Influence of core permeability on horizontal force and base pressure for a fully protected wall with a 1:1.5 front slope. Identical wave trains are applied to all structures.

In terms of horizontal force prediction, the formulation by Molines et al. (2018) generally provides conservative estimates for the present dataset, whereas the formulation by Nørgaard et al. (2013) tends to be non-conservative. Conversely, for base pressure prediction, the formulation by Nørgaard et al. (2013) offers the most accurate representation, while the formulation by Molines et al. (2018) significantly overestimates the measured values. Overall, the results indicate that core permeability has a negligible influence on horizontal wave forces but may exert a modest effect on the pressure at the front base corner.

7 INFLUENCE OF PERMEABILITY WITH A PARTLY PROTECTED WALL

The influence of a partly protected crown wall is illustrated in Fig. 10. Notably, the prescribed 90% confidence bands associated with the formulation by Nørgaard et al. (2013) exhibit substantially greater uncertainty than those observed for the fully protected wall configuration, whereas the confidence bands prescribed by Molines et al. (2018) remain unchanged. The experimental data further indicate that Model A generally yields higher dimensionless load values. However, it should be noted that the wall height C_h for this model is smaller than that of Models B and D. The difference between Models B and D is less pronounced than that observed for the fully protected wall case shown in Fig. 9. The relatively small variations observed for the partly protected wall are likely attributable to the reduced extent of the wall section influenced by rock armour placement, which in turn limits data variability. In contrast to the fully protected wall configuration, where the dimensionless horizontal force is nearly independent of wave steepness, the partly protected wall exhibits a clear dependence on wave steepness.

With respect to horizontal force prediction, the formulation by Molines et al. (2018) shows the best agreement with the experimental data for wave steepness values exceeding 0.02, whereas the formulation by Nørgaard et al. (2013) provides a more accurate representation for lower wave steepness. For the base pressure at the lower front corner, the formulation by Nørgaard et al. (2013) offers the most accurate description of the measured data, while the formulation by Molines et al. (2018) consistently overpredicts the pressure.

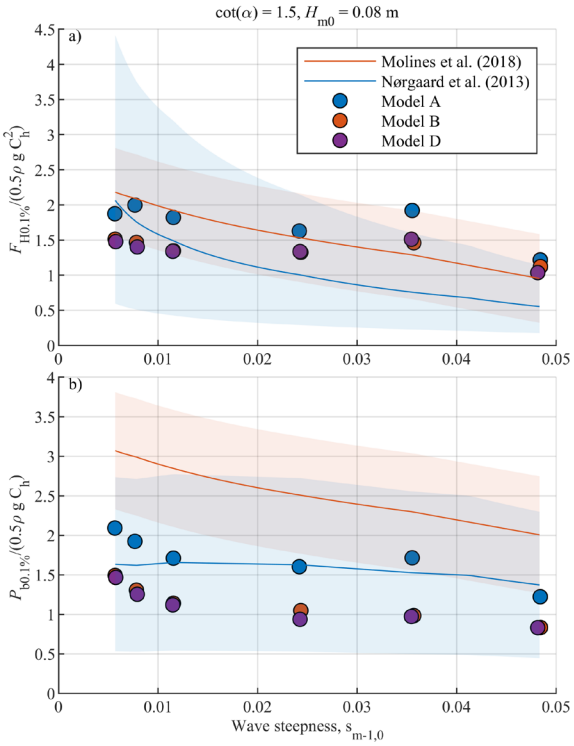

Figure 10. Influence of core permeability for a partly protected wall with a 1:1.5 front slope.

8 COMPARISON WITH EXISTING METHODS

Figure 11 presents a comparison between the measured dimensional loads and the corresponding predictions derived in the present study. The left-hand panels show predictions obtained using the formulation by Molines et al. (2018), while the right-hand panels present predictions based on Nørgaard et al. (2013). Panels (a) and (b) illustrate the horizontal force; panels (c) and (d) show the base pressure; panels (e) and (f) present the vertical force; and panels (g) and (h) depict the horizontal and vertical contributions to the overturning moment about the heel.

The prediction methods are evaluated using the following statistical indicators, where P_i denotes the predicted value and O_i the corresponding measured value:

$$MBE = \frac{1}{n}\sum_{i=1}^{n}(P_i - O_i)$$
$$\sigma_e = \sqrt{\frac{1}{n}\sum_{i=1}^{n}\left((P_i - O_i) - MBE\right)^2} \quad (6)$$
$$RMSE = \sqrt{MBE^2 + \sigma_e^2}$$

where MBE is the mean bias error, σ_e is the standard deviation of the errors, and RMSE is the root mean square error. The MBE quantifies the systematic error of the predictions; a non-zero MBE indicates a biased model. The parameter σ_e represents the random error and describes the scatter of the data, while RMSE reflects the total prediction error. The resulting statistical values are shown in Fig. 11.

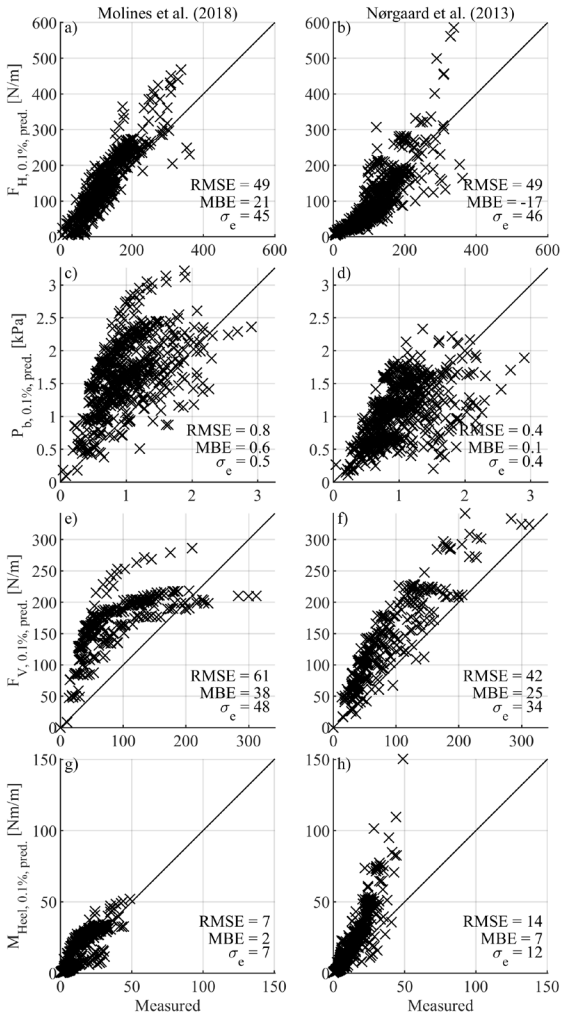

Figure 11. Comparison between measured forces and predicted values for all tested structures.

For the horizontal force, both prediction methods exhibit similar scatter and total error, as shown in Fig. 11. The primary difference lies in the bias: the formulation by Molines et al. (2018) shows a positive bias, whereas the formulation by Nørgaard et al. (2013) exhibits a negative bias.

For the base pressure, substantial scatter is observed for both methods. The formulation by Molines et al. (2018) displays a pronounced positive bias, resulting in a larger total error compared with the formulation by Nørgaard et al. (2013). Since the vertical force is assumed to follow a triangular pressure distribution and is strongly correlated with the base pressure, its prediction error reflects that observed for the base

pressure. Unlike the base pressure, the vertical force is absent for impermeable structures; these cases are therefore excluded from panels (e) and (f) of Fig. 11.

The total heel moment is best predicted by Molines et al. (2018), which exhibits the lowest scatter and total error. However, this apparent agreement results from an overestimation of the horizontal contribution combined with an underestimation of the vertical contribution. For impermeable structures (Fig. 12), where only the horizontal contribution to the moment is present, the formulation by Molines et al. (2018) underestimates the measured values (MBE < 0), whereas the formulation by Nørgaard et al. (2013) overestimates them.

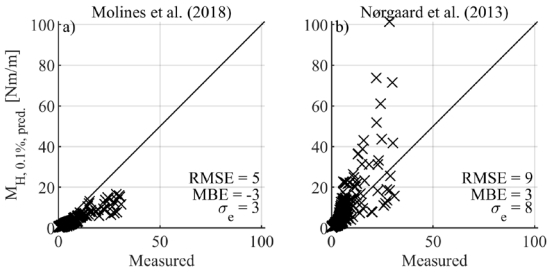

Figure 12. Comparison between measured horizontal contribution to the overturning moment and predicted values.

Table 6 summarises the ranges of parameters tested in the different experimental datasets. It is evident that the present dataset extends beyond, or deviates from, the ranges used to derive the formulae proposed by Molines et al. (2018) and Nørgaard et al. (2013). This discrepancy may partly explain the deviations observed between the measured values and the predictions in the present study.

Table 6. Tested parameter ranges for the different experimental datasets.

Datasets	$\frac{H_{m0}}{L_{m-1,0}}$	$\frac{H_{m0}}{h}$	$\frac{h}{L_{m-1,0}}$	$\frac{G_c}{L_{m-1,0}}$	$\frac{R_c}{A_c}$	$\frac{R_c}{H_{m0}}$
Present data	0.005-0.050	0.10-0.30	0.02-0.46	0.01-0.11	1.00-2.03	0.69-1.95
Nørgaard et al. (2013)	0.019-0.035	0.18-0.60	0.06-0.11	0.03-0.05	0.71-1.90	1.00-1.93
Molines et al. (2018)	0.011-0.061	0.14-0.32	0.04-0.37	0.01-0.08	1.06-2.39	1.32-2.88
Pedersen (1996)	0.016-0.071	0.16-0.35	0.08-0.32	0.03-0.19	1.00-2.64	0.61-3.63

9 CONCLUSIONS

This study extends the current understanding of wave-induced loads acting on crown walls by introducing a comprehensive experimental dataset that includes low wave steepness conditions and a wide range of structural permeabilities. The experimental results demonstrate that:

- Wave steepness has a significant influence on the measured loads, particularly for tests involving fully protected crown walls.
- Core permeability has a limited effect on horizontal wave forces but influences vertical forces and base pressures in permeable structures due to pressure dissipation beneath the crown wall.
- Existing empirical formulae remain broadly applicable, although their predictive accuracy varies depending on the load component and test conditions.
- The formulation proposed by Molines et al. (2018) provides the most accurate predictions of horizontal wave forces, albeit with a systematic positive bias. It also yields the best predictions of the total overturning moment; however, this apparent agreement results from an underestimation of the vertical moment combined with an overestimation of the horizontal moment.
- The formulation proposed by Nørgaard et al. (2013) offers more accurate estimates of base pressures and vertical forces.

Overall, the findings indicate that, while current design formulae are generally robust and the experimental data fall within the prescribed confidence bands, caution should be exercised when applying these methods to wave conditions outside the ranges for which they were originally developed. The new dataset provides valuable insight for the future refinement of design formulae, with the aim of improving guidance for structural safety assessments over a broader range of conditions. Until more reliable predictive methods become available, it is strongly recommended that crown wall designs be validated through physical model testing.

ACKNOWLEDGEMENTS

This research did not receive any specific grant from funding agencies in the public, commercial, or not-for-profit sectors.

10 REFERENCES

Eldrup, M. R. & Lykke Andersen, T., 2019a. Applicability of Nonlinear Wavemaker Theory. *Journal of Marine Science and Engineering.*

Eldrup, M. R. & Lykke Andersen, T., 2019b. Estimation of Incident and Reflected Wave Trains in Highly Nonlinear Two-Dimensional Irregular Waves. *Journal of Waterway, Port, Coastal, and Ocean Engineering,* Volume 145.

Eldrup, M. R., Lykke Andersen, T. & Burcharth, H. F., 2019. Stability of rubble mound breakwaters—A study of the notional permeability factor, based on physical model tests. *Water.*

Eldrup, M. R., Lykke Andersen, T., Van Doorslaer, K. & Van der Meer, J., 2022. Improved Guidance on Roughness and Crest Width in Overtopping of Rubble Mound Structures Along EurOtop. *Coastal Engineering.*

Lamberti, A., Martinelli, L., Gabriella Gaeta, M., Tirindelli, M., Alderson, J., 2011. Experimental spatial correlation of wave loads on front decks. *Journal of Hydraulic Research* (49), 81–90.

Lykke Andersen, T., Clavero, M., Frigaard, P., Losada, M., & Puyol, J. I., 2016. A New Active Absorption System and its Performance to Linear and Non-Linear Waves. *Coastal Engineering,* Volume 114, pp. 47-60.

Lykke Andersen, T., Clavero, M., Eldrup, M. R., Frigaard, P. B., & Losada, M. 2018. Active Absorption of Nonlinear Irregular Waves. *Proceedings of the Coastal Engineering Conference*.

Martin, F. L., Losada, M. A. & Medina, R. J., 1999. Wave loads on rubble mound breakwater crown walls. *Coastal Engineering.*

Molines, J., 2016. Wave Overtopping and Crown Wall Stability of Cube and Cubipodarmored Mound Breakwaters. PhD Thesis. *Universitat Politècnica de València*.

Molines, J., Herrera P., M. & Medina R., J., 2018. Estimations of wave forces on crown walls based on wave overtopping rates. *Coastal Engineering.*

Nørgaard, J. Q. H., Lykke Andersen, T. & Burcharth, H. F., 2013. Wave loads on rubble mound breakwater crown walls in deep and shallow water wave conditions. *Coastal Engineering.*

Pedersen, J., 1996. Wave Forces and Overtopping on Crown Walls of Rubble Mound Breakwaters - An Experimental Study.

Schäffer, H. A., 1996. Second-Order Wavemaker Theory for Irregular Waves. *Ocean Engineering,* 23(1), pp. 47-88.

Tavakkol, S. & Lynett, P., 2017. Celeris: A GPU-accelerated open source software with a Boussinesq-type wave solver for real-time interactive simulation and visualization. *Computer Physics Communications,* Volume 217, pp. 117-127.

Van der Meer, J. W. 1988. Rock slopes and gravel beaches under wave attack. *Delft hydraulics*.

Van der Meer, J. W. & Stam, C. J. M., 1992. Wave runup on smooth and rock slopes of coastal structures. *Journal of waterway, Port, coastal, and Ocean Engineering.*

Zhang, H., Schäffer, H. A. & Jakobsen, K. P., 2007. Deterministic Combination of Numerical and Physical Coastal Wave Models. *Coastal Engineering,* 54(2), pp. 171-186.

Aalborg University, 2023a. *AwaSys - Software for Wave Laboratories.*
Available at: www.hydrosoft.civil.aau.dk/awasys

Aalborg University, 2023b. *WaveLab - Software for Wave Laboratories.*
Available at: www.hydrosoft.civil.aau.dk/wavelab

DOI: https://doi.org/10.53256/COSE_240102

Integrating open-access data for beach monitoring and countermeasure planning: a case study of the southeastern Adriatic

Ružica Rumenović, Morena Galešić Divić, Toni Kekez, and Veljko Srzić
University of Split, Faculty of Civil Engineering, Architecture and Geodesy, Split, Croatia
rrumenovic@gradst.hr

ABSTRACT: In tourism-driven coastal regions, beaches provide substantial economic and ecological value but are increasingly threatened by erosion and flooding, which jeopardise their long-term sustainability. To address these challenges, data-driven monitoring and countermeasure planning are essential, particularly in areas where continuous in situ monitoring infrastructure is limited. This study, conducted within the ClimBeach project (Interreg VI-A IPA CBC Croatia–Bosnia and Herzegovina–Montenegro), investigates how publicly accessible datasets can support coastal monitoring strategies and inform the selection of appropriate countermeasures across twelve pilot sites in Croatia, Bosnia and Herzegovina, and Montenegro.

Spatially distributed meteorological data (Visual Crossing), oceanographic products (Copernicus Marine Environment Monitoring Service), and historical shoreline changes derived from Google Earth satellite imagery are analysed to assess their suitability and reliability for monitoring beach evolution. These datasets provide insights into climatic influences, erosion-prone periods, wave climate variability, and site-specific vulnerability. Such information enables the development of adaptive monitoring schedules and supports the selection of hard, soft, hybrid, or management-based countermeasures.

By linking historical data trends with targeted interventions, this study proposes a cost-effective framework for beach monitoring and coastal resilience planning in the southeastern Adriatic. The findings contribute to the development of scalable coastal adaptation strategies that balance data accessibility, intervention feasibility, and resource efficiency in vulnerable coastal areas.

1 INTRODUCTION

Beaches constitute essential economic, ecological, and social resources, particularly in regions that rely heavily on tourism and fishing. They provide a wide range of benefits, including recreational opportunities, habitat provision, and contributions to community identity (Dixon et al., 2012). However, these valuable coastal systems are increasingly threatened by challenges such as shoreline erosion, sea-level rise, and the growing frequency and intensity of extreme weather events associated with climate change (Bonaldo et al., 2020). The need for adaptive and proactive coastal protection measures is therefore urgent, especially in regions where systematic, long-term monitoring and data collection remain limited (Ewing, 2015).

The eastern Adriatic coastline, extending along Croatia, Bosnia and Herzegovina, and Montenegro, exemplifies the demand for effective and evidence-based coastal management strategies. This region is subject to a complex interplay of processes, including dynamic sediment transport, human-induced alterations to natural sediment supply, and increasing coastal development, all of which drive rapid and site-specific shoreline changes. These dynamics underscore the importance of continuous and structured monitoring to detect trends and support timely management interventions (Pikelj et al., 2017). While several studies have examined coastal erosion in the northern Adriatic in the context of climate change (Torresan et al., 2019; Gallina et al., 2019), the southern and eastern Adriatic remain comparatively underrepresented in site-specific research. Nevertheless, recent studies have begun to address these gaps through shoreline monitoring initiatives (Miličević et al., 2022) and evaluations of beach nourishment practices (Bogovac et al., 2023a).

To build on these efforts and extend practical methodologies to under-monitored coastal areas, the ClimBeach project was initiated within the Interreg VI-A IPA CBC framework (University of Split, n.d.). The project aims to enhance coastal resilience through cost-effective monitoring approaches and targeted intervention planning

across twelve pilot beaches in the three participating countries. This paper investigates how publicly available datasets—including meteorological records, wave and sea-level reanalysis products, and remote sensing imagery—can be integrated to support data-informed decision-making in beach management. In line with recent studies applying Copernicus Marine Environment Monitoring Service (CMEMS) data for wave modelling along the Croatian coast (Bujak et al., 2023), the present approach combines these data sources through a structured analytical framework designed to:

- characterise local environmental forcing and beach typologies;
- guide the placement and scheduling of in situ monitoring campaigns; and
- support the selection of appropriate countermeasures to mitigate erosion and flooding risks.

A beach classification scheme is introduced, drawing on established coastal morphology frameworks and refined through a comparative analysis of relevant literature and site-specific characteristics (Mangor et al., 2017). This classification links geomorphological features with wave exposure, sediment availability, and anthropogenic influence, based on a systematic assessment of open-access datasets encompassing meteorological, oceanographic, and shoreline change parameters.

The methodology section outlines the steps undertaken to conduct a comprehensive literature review, identify and select suitable open-access datasets, perform site-specific data analyses, and design a practical monitoring plan aligned with forthcoming procurement activities. The results section then presents a beach typology tailored to the twelve pilot sites, identifies suitable countermeasures, and describes the development of an adaptive monitoring plan. Finally, the paper discusses current limitations, including gaps in site-specific data availability, and highlights how these constraints inform priorities for future monitoring efforts and targeted coastal protection measures.

2 METHODOLOGY

This section describes the literature review, pilot sites, datasets, and analytical framework employed to support beach monitoring and countermeasure planning in the southeastern Adriatic.

2.1 Literature review

To ensure that the proposed approach is grounded in robust evidence and established practice, a comprehensive literature review was conducted as an integral component of the study methodology. The review pursued two primary objectives:

1. to evaluate the extent to which existing scientific literature reflects the coastal conditions characteristic of the eastern Adriatic; and
2. to compile a broad range of previously implemented countermeasures from other regions that may be suitable for local adaptation.

The review process combined systematic searches of major scientific journals and bibliographic databases with targeted screening of relevant project reports and coastal management guidelines. Search terms included combinations of *coastal erosion*, *beach stabilisation*, *nourishment*, *shoreline monitoring*, *hybrid countermeasures*, *Adriatic Sea*, and *under-monitored coasts*.

In total, 73 sources were systematically analysed, comprising peer-reviewed journal articles, specialised monographs, and applied technical reports. Although only a limited subset of these studies directly addresses the southern and eastern Adriatic, comparable case studies from the northern Adriatic, other Mediterranean regions, Japan, and Northern Europe provide valuable and well-documented examples. The reviewed literature encompasses both conventional hard engineering solutions and emerging nature-based or hybrid approaches, offering practical insights that inform site-specific planning for the twelve pilot beaches.

2.2 Case study sites

Twelve pilot beaches were selected across Croatia, Bosnia and Herzegovina, and Montenegro within the framework of the ClimBeach project (Fig. 1). The selected sites represent a broad range of geomorphological settings, wave exposure conditions, and levels of anthropogenic pressure. The pilot sites are as follows:

- **PS1:** Janska Bay, Dubrovnik–Neretva County, Croatia
- **PS2:** Doli Bay, Dubrovnik–Neretva County, Croatia
- **PS3:** Vučine Beach, Pelješac, Croatia
- **PS4:** Trstenica Beach, Orebić, Pelješac, Croatia
- **PS5:** Druga Strana Beach, Neum, Bosnia and Herzegovina

- **PS6:** Meredek Beach, Neum, Bosnia and Herzegovina
- **PS7:** Plavi Horizonti Beach, Montenegro
- **PS8:** Jaz Beach, Budva, Montenegro
- **PS9:** Ričardova Glava Beach, Budva, Montenegro
- **PS10:** Pizana Beach, Budva, Montenegro
- **PS11:** Utjeha Beach, Montenegro
- **PS12:** Veliki Pijesak Beach, Dobra Voda, Montenegro

The site selection aimed to capture variability in sediment characteristics (sandy, gravel, and mixed beaches), degrees of urbanisation, and exposure to dominant wave directions, primarily bora and sirocco. This diversity supported the classification of the beaches into low-, moderate-, and high-energy categories, which in turn informed monitoring priorities and countermeasure planning.

Figure 1. Case study sites (Source: Google Earth).

The Croatian sites include both open-coast and sheltered environments. Trstenica (PS4) and Vučine (PS3), in particular, are characterised by increasing urban pressure and limited natural sediment supply. Neum, the only coastal town in Bosnia and Herzegovina, features two pilot sites with contrasting orientations and wave energy regimes. The Montenegrin beaches exhibit a wide range of conditions, from relatively natural and morphodynamically active settings such as Veliki Pijesak (PS12) to highly urbanised beach segments, including Ričardova Glava (PS9).

2.3 *Data sources and processing*

This section summarises the publicly available datasets and data processing steps used to characterise environmental conditions and support monitoring and planning activities across the twelve pilot beaches. The datasets were selected based on their availability, spatial and temporal resolution, and relevance to key coastal forcing parameters, including wind, waves, sea level, sediment transport, and shoreline evolution. Trstenica Beach (PS4) (Fig. 18), located in Orebić on the Pelješac Peninsula, is used as a representative case study to illustrate the data processing and interpretation workflows applied throughout the study.

2.3.1 *Meteorological and climatological data*

Historical meteorological parameters, including air temperature, precipitation, and wind, were obtained from Visual Crossing, a platform that processes and harmonises data from multiple reputable sources and integrates observations from various local meteorological stations, thereby providing reliable and consistent reconstructions of past climate conditions (Visual Crossing, 2020). The combination of global and local datasets ensures both accuracy and completeness in historical and forecast weather records.

As no dedicated meteorological station is located at Trstenica Beach, precipitation data were retrieved from Visual Crossing using interpolated datasets for Orebić (42.9747° N, 17.1841° E), the nearest available reference location, based on observations from surrounding stations in Ploče and Lastovo. To minimise topographic bias, orographic filtering was applied by excluding stations situated at elevations exceeding 100 m within a 50 km radius (Peña Quiñones et al., 2019), as illustrated in Figure 3.

Figure 2. Location and meteorological station map for Orebić (42.9747° N, 17.1841° E) (source: Visual Crossing).

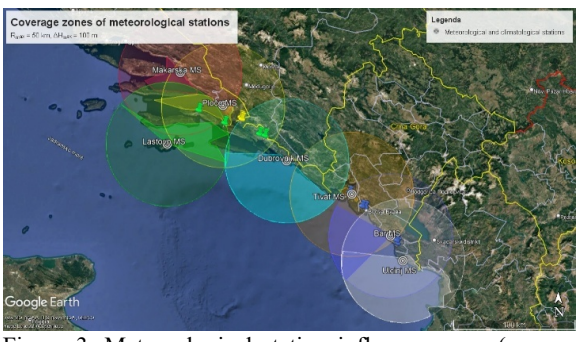

Figure 3. Meteorological station influence areas (source: Google Earth).

Visual summaries were generated to evaluate climatic conditions at Trstenica Beach for the period from 1 January 1992 to 1 January 2025, using interpolated Visual Crossing datasets as the primary data source (Figs. 2 and 3). All visualisations were produced using MATLAB® software (version R2024b). Figure 4 presents the total annual precipitation, which exhibits pronounced interannual variability, with elevated

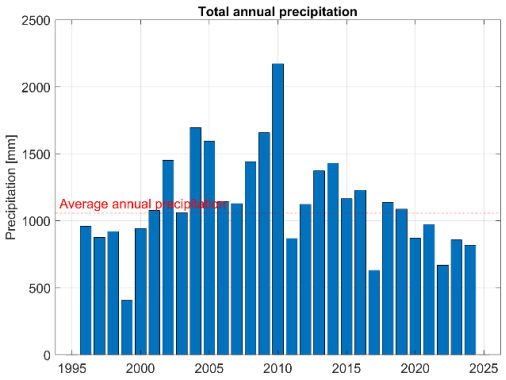

values during the period 2010–2015 and a potential slight decline in more recent years.

Figure 4. Total annual precipitation for the period 1995–2025 at Orebić (42.9747° N, 17.1841° E).

The temperature time series (Figure 5) confirms a typical Mediterranean climate, characterised by warm summers (July–August) and mild winters, with a clear and consistent seasonal pattern.

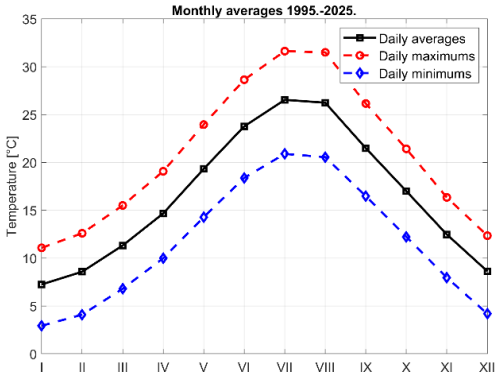

Figure 5. Average air temperature for the period 1996–2025 at Orebić (42.9747° N, 17.1841° E).

At Trstenica Beach, dominant southern (Ostro) and south-eastern winds (Scirocco, SE and SSE) play a significant role in sediment transport, driving erosion and shoreline reshaping through high-energy cross-shore and longshore processes (Aron, 2015). In contrast, Maestral and Bora winds have a comparatively limited influence on coastal morphodynamics at the site (Figure 6).

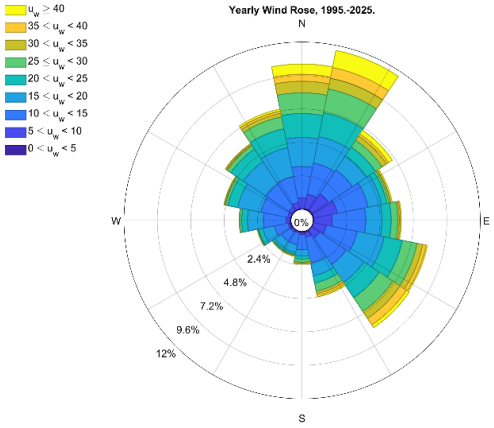

Figure 6. Annual wind rose for the period 1995–2025 at Orebić (42.9747° N, 17.1841° E)

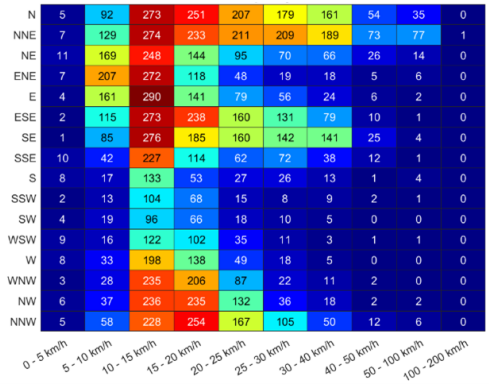

Figure 7. Wind frequency heatmap for the period 1995–2025 at Orebić (42.9747° N, 17.1841° E)

The wind frequency heatmap (Figure 7) indicates that moderate wind speeds (10–25 km h^{-1}) occur most frequently from the NE, E, and NNW sectors. Strong winds exceeding 40 km h^{-1} are comparatively rare but are nonetheless present in the long-term record.

2.3.2 *Oceanographic data*

Two distinct datasets from the CMEMS were employed:

- Wave data were obtained from the CMCC *MEDSEA_MULTIYEAR_WAV_006_012* reanalysis product based on the MEDWAM3I model (Korres et al., 2021). This high-resolution multi-year dataset covers the period from 1 January 1985 to 31 May 2023 and was extracted at the representative offshore location 42.5625° N, 17.8334° E for Trstenica Beach (indicated by the yellow marker in Fig. 1). The dataset provides hourly spectral wave parameters,

including significant wave height (H_{m0}), mean wave period (T_{m02}), and mean wave direction. Wave components are classified into locally generated wind waves and primary and secondary swell components, enabling assessment of coastal exposure and dominant energy regimes. The reanalysis incorporates satellite-derived significant wave height data through assimilation from CERSAT–IFREMER and the Copernicus Marine WAVE TAC.

The wave rose shown in Fig. 8 indicates that waves predominantly approach from the west (W) and south-southeast (SE), with SE waves exhibiting higher energy levels.

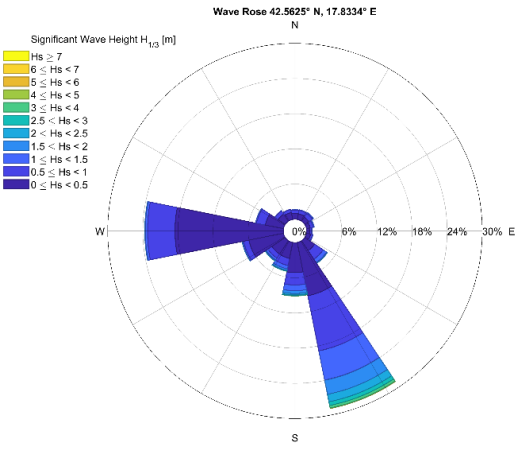

Figure 8. Wave rose for the period 1 January 1985–31 May 2023 at the representative location 42.5625° N, 17.8334° E.

Most wave conditions are characterised by significant wave heights below 2 m, with only occasional occurrences of larger events. Waves approaching from the SE sector display higher wave heights, typically in the range of 3–4 m, as indicated by the green and yellow sectors in Fig. 8. These higher-energy waves are likely associated with Sirocco winds acting over a long fetch. In contrast, waves from the W sector are more frequent but generally lower in energy, implying different sediment transport mechanisms and morphodynamic responses. The maximum significant wave height recorded in the dataset reached 6.86 m.

The scatter plot of significant wave height versus wave period (Fig. 9) reveals a clear relationship in which increasing wave heights correspond to longer wave periods. Smaller waves ($H_{m0} < 1.5$ m) typically exhibit periods of 3–6 s, characteristic of locally generated wind waves. Moderate waves ($H_{m0} = 1.5$–3 m) are associated with periods of approximately 6–10 s, indicating a mixture of wind waves and developing swell. Larger wave events ($H_{m0} > 3$ m) frequently display periods exceeding 10–15 s, suggesting the presence of well-developed swell generated by distant storm systems. This distribution highlights the coexistence of short-period local wind waves and long-period swell, governed by wind strength, storm activity, and broader regional oceanographic conditions.

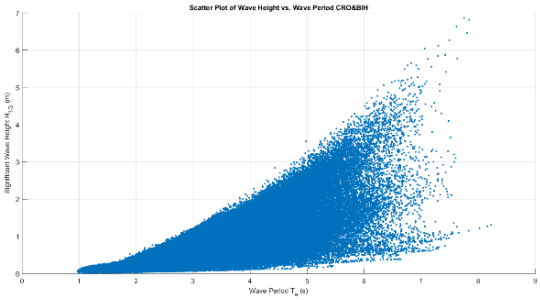

Figure 9. Scatter plot of significant wave height versus wave period for the period 1 January 2024–31 January 2025.

- Sea-level data were retrieved from the CMEMS *MEDSEA_ANALYSISFORECAST_PHY_006_013* product (Clementi et al., 2021), which provides sea surface height (zos) at 15-minute temporal resolution. To assess the reliability of the modelled sea-level data, CMEMS outputs were compared with long-term in situ measurements from the "sobr" tide gauge station (42.792° N, 17.620° E). Observed sea-level data were obtained from the European Marine Observation and Data Network (EMODnet) and are available at a 1-minute temporal resolution (Institute of Oceanography and Fisheries). These measurements are referenced to the local Mean Lower Low Water (MLLW) datum.

Comparison of the CMEMS modelled sea surface heights with the observed tide gauge records shows strong agreement in temporal variability. As the CMEMS data are referenced to a geoid while the tide gauge measurements are referenced to MLLW, a vertical offset was applied to enable direct comparison. This offset, equal to 0.35 m, was calculated as the mean difference between the two datasets over the overlapping period from 1 January 2024 to 31 January 2025 using hourly averaged values.

After applying the vertical correction, the adjusted time series exhibited high consistency, with a root mean square error (RMSE) of 0.079 m, a mean bias of 0.059 m, and a Pearson correlation coefficient (r) of 0.91 (Fig. 10). These

results confirm that, once datum differences are accounted for, the CMEMS product provides a reliable representation of local sea-level variability and is suitable for coastal applications requiring absolute sea-level information. The use of co-located tide gauge data for vertical calibration further ensures that reference levels accurately reflect local conditions, thereby increasing confidence in the model's coastal performance.

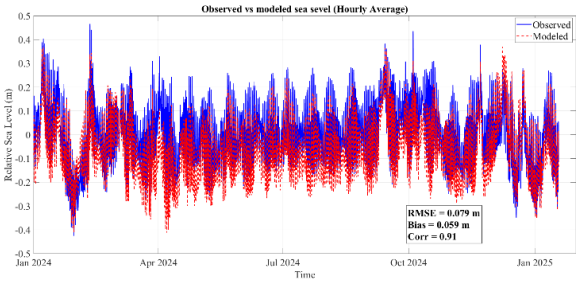

Figure 10. Comparison between observed and modelled sea level (hourly averages) for the period 1 January 2024–31 January 2025.

2.3.3 *Shoreline and morphological change*

Historical beach morphology was assessed using Google Earth satellite imagery covering the period from 2009 to 2024 (Figure 11).

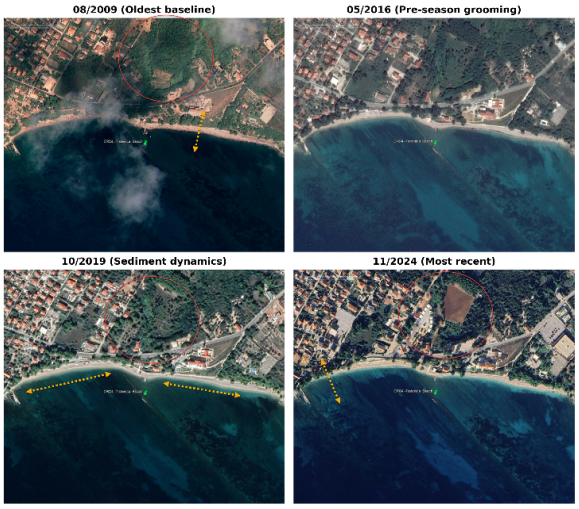

Figure 11. Satellite imagery of Trstenica Beach at selected time points (2009, 2016, 2019, and 2024).

Changes in shoreline position were identified through manual interpretation of the imagery, revealing key morphological and environmental developments over time. The 2009 image was adopted as the baseline condition and shows extensive inland vegetation. A pre-season nourishment event carried out in 2016 resulted in a widened beach profile and lighter sediment colouration. By 2019, evidence of sediment redistribution is apparent, accompanied by localised beach narrowing. The 2024 image highlights inland urban expansion (indicated by red circles), which may influence surface runoff patterns and sediment dynamics. Yellow arrows denote the inferred directions of sediment movement. It should be noted that, due to the absence of time-of-day metadata in Google Earth imagery, no correction for tidal stage was applied. However, given that the maximum tidal amplitude in the study area is less than 25 cm (Šepić et al., 2022), this source of uncertainty is smaller than the spatial resolution of the imagery and is therefore not expected to significantly affect the identification of general shoreline change trends.

2.3.4 *Bathymetry*

Baseline bathymetric data were obtained from the European Marine Observation and Data Network (EMODnet), providing regional-scale seabed depth information across the Adriatic Sea (). To achieve higher spatial resolution in Croatian coastal waters, detailed cross-shore bathymetric profiles were additionally sourced from the VEPAR project (Hrvatske vode, 2022) (Figure 13). These bathymetric datasets support:

- analysis of wave dissipation patterns;
- identification of potential sediment traps and erosional hotspots; and
- informed placement of monitoring equipment in future field campaigns.

Together, the combined bathymetric datasets enhanced the resolution of coastal morphology assessments and contributed to refining the beach typology and monitoring strategies proposed in this study.

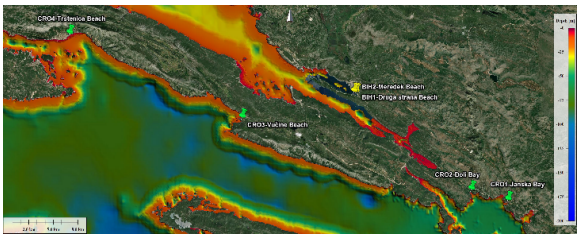

Figure 12. Regional bathymetric map showing seabed depth variations along the coastline.

Figure 13. Detailed bathymetric map of Trstenica Beach, showing isobaths representing depth contours in metres.

2.4 *Monitoring plan development*

The ClimBeach project aims to establish a cost-effective and scalable coastal monitoring plan for twelve pilot beaches across Croatia, Bosnia and Herzegovina, and Montenegro. Although full on-site implementation has not yet commenced, execution of the monitoring plan is underway through public procurement processes that have already been initiated. These processes include forthcoming photogrammetric surveys and sensor-based monitoring campaigns, which have been specified in accordance with the technical requirements, site-specific priorities, and monitoring frequencies defined within the proposed framework.

The monitoring plan was developed using a structured, data-informed methodology that integrates open-access datasets, insights derived from beach typology classification, and operational considerations shaped by available budgets and stakeholder input. Specifically, the monitoring framework was established by combining:

- publicly available datasets (as described in Section 2.3) to identify site-specific exposure conditions and data gaps;
- a typology-based classification of beaches (Section 2.2) to prioritise monitoring efforts;
- informal consultations with local experts and project stakeholders to assess site accessibility and practical relevance; and
- budgetary constraints and technical specifications defined by project partners, including predefined allowances for equipment types and monitoring campaigns.

Rather than adopting a uniform monitoring strategy across all sites, the proposed plan is designed to be adaptive, tailoring monitoring intensity and techniques to the specific characteristics, risks, and constraints of each pilot beach.

3 RESULTS AND DISCUSSION

Building on the structured methodology described in Section 2, this section presents the main outputs of the ClimBeach approach, namely: (i) a practical beach typology and classification of the pilot sites, (ii) indicative countermeasures, and (iii) a scalable monitoring plan incorporating risk mitigation measures. These results demonstrate how readily accessible, open-access, and low-cost datasets can be effectively used as a screening tool to support monitoring design and intervention planning in under-monitored coastal areas. The final subsection synthesises the key findings and discusses the current limitations of the proposed approach.

3.1 *Beach typology and classification criteria*

To structure the monitoring plan and guide countermeasure recommendations, the pilot beaches were classified into typological groups based on a synthesis of geomorphological literature, publicly available spatial datasets, and regional contextual knowledge. The principal classification parameters included:

- sediment type (sand, gravel, or mixed);
- wave exposure (low, moderate, or high, based on prevailing wind regimes and fetch length);
- degree of urbanisation or anthropogenic pressure (e.g. built surroundings, modified coastlines); and
- observed or reported erosion and flooding trends.

Although urbanisation and anthropogenic pressure were qualitatively assessed to inform the contextual understanding of each site, these factors were not used as primary axes in the final typological classification.

The qualitative typology was not derived from a single model but emerged from the comparative integration of multiple established frameworks (Mangor et al., 2017; Nordstrom, 2000), as described in Section 2.1. The resulting classification supports the design of site-specific monitoring protocols by prioritising higher-risk locations for more frequent or instrument-intensive observations. It also informs the selection of appropriate countermeasures, ensuring consistency between natural beach dynamics and proposed interventions.

Based on the defined parameters and a review of relevant literature, the following beach types are proposed:

- sediment-limited beaches;
- sediment-rich beaches;
- pocket beaches in confined settings;
- barrier islands and barrier spit beaches; and
- beaches in extreme environments (high-latitude or tropical).

Within this framework, the twelve pilot sites were assigned to the defined beach types based on the analysed literature and datasets (Section 2). Sediment-limited beaches include Janska Bay (PS1), Vučine Beach (PS3) (Figure 14**Errore. L'origine riferimento non è stata trovata.**), Meredek Beach (PS6) (Figure 14**Errore. L'origine riferimento non è stata trovata.**), Druga Strana Beach (PS5), Pizana Beach (PS10) (Trstenica Beach (PS4) (Figure 17**Errore. L'origine riferimento non è stata trovata.**, and Ričardova Glava Beach (PS9).

These sites are typically composed of coarse or mixed sediments with limited natural sediment replenishment and are often located adjacent to urbanised areas or hardened shorelines. They generally experience low to moderate wave exposure and are particularly susceptible to erosion. Consequently, they are potential candidates for protective measures such as seawalls, revetments, or localised beach nourishment.

Figure 14. Vučine beach (PS3), sediment-limited beach (Source: Adriagate).

Figure 15. Meredek Beach (PS6), sheltered sediment-limited beach, (Source: Larissa)

Figure 16. Pizana Beach (PS10), sediment-limited beach (Source: BeachSearcher).

Figure 17. Trstenica beach (PS4), sediment-limited beach (Source: Adriagate).

Pocket beaches in confined settings include Doli Bay (PS2), Plavi Horizonti Beach (PS7) (Figure 18), and Utjeha Beach (PS11). These beaches are situated within sheltered embayments or enclosed coastal formations, often characterised by restricted sediment exchange and low wave exposure. As a result, they tend to maintain relative morphological stability unless affected by human activities or episodic storm events.

Figure 18. Plavi Horizonti Beach, pocket beach with moderate sediment availability (Source: Google Earth).

Sediment/rich beaches are represented by Jaz Beach (PS8) (Figure 19) and Veliki Pijesak Beach (PS12). These sites receive continuous or episodic sediment input through natural processes such as riverine supply or slope instability. They are typically influenced by moderate to high wave exposure and exhibit dynamic shoreline behaviour. In such environments, passive management strategies combined with continuous monitoring are generally preferred in order to preserve natural sediment transport processes.

Figure 19. Jaz Beach (PS8), Montenegro (Source: Guide to Europe).

The remaining typological groups—barrier islands and barrier spit beaches, and beaches in extreme environments—are included in the proposed classification framework to ensure completeness and applicability to future studies. However, none of the selected pilot sites fall within these categories.

To facilitate comparative interpretation, Figure 20 provides a simplified overview of the twelve pilot sites in terms of wave energy and sediment availability. This representation illustrates the relative positioning of the sites along these two primary axes and complements the descriptive typology presented above.

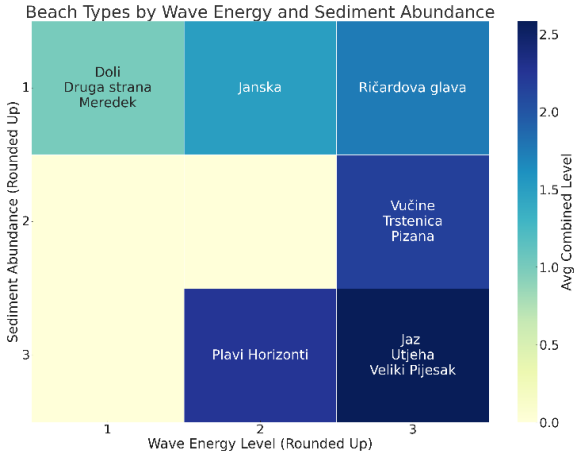

Figure 20 Beach types classified by wave energy and sediment abundance for the twelve pilot sites. Qualitative factors such as urbanisation and erosion trends, discussed in the text, are not included in this visualization.

Overall, this site-based classification enables the tailoring of monitoring intensity and countermeasure strategies to local conditions, thereby enhancing the effectiveness and long-term sustainability of the proposed interventions.

3.2 *Countermeasures categories*

To address beach erosion and coastal flooding, coastal protection strategies can be broadly grouped into four main categories: hard engineering, soft engineering, hybrid solutions, and management and policy-based approaches (Fig. 21).

Hard engineering measures, such as breakwaters and groynes, rely on engineered structures to provide immediate and often robust protection against wave action and sediment loss. Soft engineering measures, including beach nourishment and dune restoration, employ nature-based or nature-inspired solutions that aim to work with natural coastal processes and are generally more sustainable in the long term. Hybrid approaches combine elements of both hard and soft engineering to enhance resilience and adaptability under varying environmental conditions. In parallel, management- and policy-based strategies—such as Integrated Coastal Zone Management (ICZM) and ecosystem-based adaptation—seek to embed technical interventions within broader planning, governance, and decision-making frameworks.

These categories provide a structured reference for aligning the selection of future countermeasures with the typological vulnerabilities identified through the ClimBeach project, thereby supporting context-sensitive and sustainable coastal management.

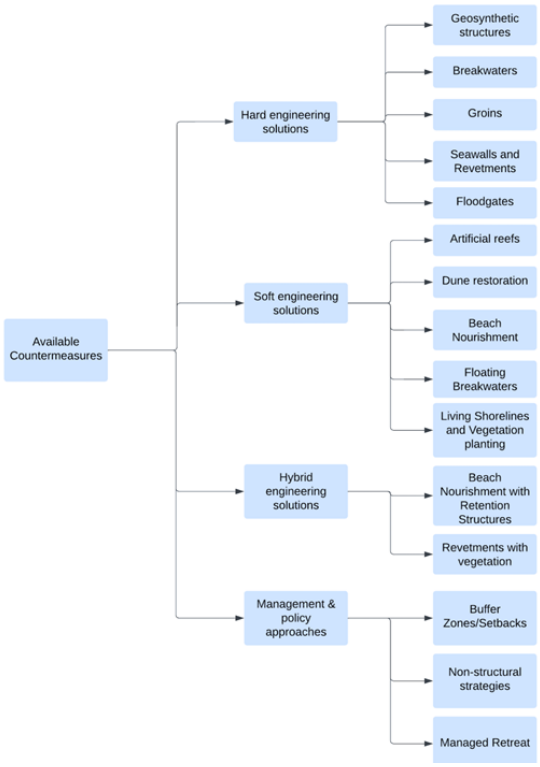

Figure 21 Available countermeasures (adapted from the ClimBeach Countermeasure Review Report, 2024)

3.3 *Monitoring framework and implementation plan*

The structured methodology described in Section 2.4 was applied to develop a scalable, multi-site monitoring framework tailored to typology-specific vulnerabilities and available resources. The framework identifies appropriate monitoring tools and observation strategies based on environmental forcing conditions, logistical feasibility, and cost efficiency.

The selected monitoring instruments and techniques include:

- Acoustic Wave and Current Profilers (AWACs) for high-resolution measurements of wave and current dynamics at high-energy beaches;
- drone-based photogrammetry to monitor shoreline position and beach volume, applicable to both aerial surveys and nearshore morphological assessments; and
- meteorological stations to improve the spatial resolution and accuracy of climate forcing data in under-monitored regions.

The placement of meteorological stations was guided by an analysis of station influence zones using topographic information from Google Earth and meteorological coverage from the Visual Crossing dataset (Figure 3). Particular attention was paid to areas where existing station coverage is limited due to elevation effects or remoteness. The Pelješac Peninsula, and Trstenica Beach in particular, was identified as a priority location for the installation of a new meteorological station owing to its exposure to prevailing wind regimes and the lack of nearby low-elevation data sources. Similarly, in Montenegro, sparse coverage in mountainous and coastal fringe areas informed the proposed deployment strategy.

Monitoring intervals were defined as either seasonal or event-driven, allowing intensified observation following major storm events or periods of rapid morphological change. Public procurement procedures for several monitoring components, including photogrammetric surveys and the installation of two meteorological stations, have already commenced and are expected to support implementation within the current project year.

A tentative deployment schedule has also been developed for AWAC instruments across pilot sites in Croatia, Bosnia and Herzegovina, and Montenegro. These deployments are staggered by location, duration, and energy exposure, with instruments rotated among sites based on historical wave exposure and monitoring priority. Aerial and photogrammetric surveys are planned at four to six epochs per site, adjusted to site-specific sediment dynamics and visibility constraints. Together, these measures ensure that data collection captures key events and periods of heightened morphodynamic activity.

3.4 *Risk mitigation strategy*

Recognising the operational challenges associated with coastal monitoring in dynamic and often harsh environments, a layered risk mitigation strategy was developed to ensure continuity of operations, data reliability, and efficient use of resources.

- Sensor reliability: Instruments such as Acoustic Wave and Current Profilers (AWACs) and meteorological stations may malfunction or sustain damage during severe weather events. To mitigate this risk, regular inspection and maintenance schedules are предусмотрен, and spare components are planned. In the event of sensor failure, data gaps may be addressed through interpolation or supplemented using open-access datasets, including products from the Copernicus Marine Environment Monitoring Service (CMEMS) and EMODnet.
- Extreme weather and data gaps: Severe storm conditions may prevent scheduled

data acquisition. In such cases, numerical model outputs and satellite-based observations—such as those from the Moderate Resolution Imaging Spectroradiometer (MODIS) and Sentinel-3 missions—are proposed to reconstruct missing measurements.

- Deployment limitations: Delays in instrument deployment due to restricted site access or limited technical support will be mitigated through flexible deployment windows and coordination with other project activities to optimise fieldwork efficiency.
- Survey contingencies: Financial constraints or adverse environmental conditions affecting planned surveys will be addressed through the use of alternative data sources, including satellite-derived bathymetry (SDB), Sentinel-2 imagery, and Unmanned Aerial Vehicle (UAV)-based surveys. Additional technical or logistical support may be sought through institutional collaborations where necessary.

Through this flexible and anticipatory approach, the monitoring programme aims to maintain the integrity, continuity, and scientific value of the collected data under a wide range of external constraints.

3.5 *Indicative countermeasure planning*

Beaches characterised by high wave exposure and limited sediment availability—such as steep pocket beaches or highly urbanised coastal stretches—may benefit from hybrid or soft engineering solutions, including beach nourishment, vegetative buffers, or submerged structures designed to attenuate wave energy. In contrast, sites with moderate exposure and sufficient sediment supply may be adequately managed through periodic monitoring combined with adaptive maintenance strategies.

The proposed recommendations are indicative and will be further refined based on the outcomes of forthcoming monitoring campaigns and subsequent numerical and physical modelling efforts. Integrating real-time observations with historical data trends is expected to improve the assessment of feasibility and prioritisation of site-specific coastal protection strategies, ensuring that implemented interventions are aligned with both prevailing environmental conditions and available financial and technical resources

3.6 *Discussion*

Open-access and low-cost datasets, when combined with relatively simple analytical methods, can effectively support beach classification and preliminary countermeasure planning in under-monitored coastal regions. Nevertheless, several limitations affect the precision and reliability of the resulting assessments.

First, shoreline mapping based on Google Earth satellite imagery introduces inherent uncertainty, as sea level, tidal stage, and wave conditions at the time of image acquisition are generally unknown. These factors can lead to apparent shifts in shoreline position, particularly on narrow or steep beaches.

Second, reanalysis products from the Copernicus Marine Service are well suited to capturing regional wave and sea-level trends but often lack sufficient nearshore resolution to fully resolve local wave energy gradients and site-specific exposure conditions.

Third, meteorological data derived from national weather stations may not adequately represent local forcing, especially in areas where topographic sheltering or coastal orientation significantly modifies wind and storm exposure.

Although the developed beach typology and indicative countermeasure framework provide a valuable baseline for planning, they require refinement through in situ shoreline monitoring, higher-resolution numerical modelling, and site-specific measurements to ensure effective and reliable local implementation.

4 CONCLUSIONS AND FUTURE WORK

This study demonstrates how open-access and low-cost datasets can be used to support practical coastal monitoring and protection planning in data-scarce regions. By linking wave exposure, sediment availability, and coastal morphology, a beach typology was developed to guide site-specific monitoring priorities and indicative countermeasure selection across twelve pilot beaches in the southeastern Adriatic.

The proposed methodology was primarily applied as a screening tool to structure monitoring plans and prioritise intervention needs under limited financial and technical resources. Clear spatial patterns emerged: sediment-limited and urbanised sites, such as Trstenica and Ričardova Glava, exhibit higher susceptibility to erosion and flooding, whereas sediment-rich and

morphodynamically active beaches, such as Jaz and Veliki Pijesak, demonstrate greater natural resilience.

These findings directly support the development of *BeachCloud*, the ClimBeach project's open-access decision-support platform for adaptive coastal management. BeachCloud will integrate the typological framework with site-specific monitoring data, numerical and physical modelling outputs, and practical guidance to assist local authorities in planning resilient and cost-effective coastal protection measures.

Importantly, the ClimBeach project has already initiated activities to refine and expand the proposed screening framework. Public procurement, installation of in situ monitoring systems for shoreline position, waves, and sea level, and deployment of additional meteorological sensors are currently underway across the twelve pilot sites. These efforts will generate high-resolution datasets for validating observed shoreline trends and calibrating advanced numerical models, including planned XBeach simulations and selected physical modelling, to test and optimise proposed countermeasures under realistic forcing conditions.

In the longer term, the integration of UAV-based shoreline monitoring, community-based data collection, and the implementation and evaluation of nature-based and hybrid solutions will further strengthen adaptive coastal management. The structured approach presented in this study, together with the ongoing ClimBeach activities, aims to provide a replicable and transferable framework for enhancing beach resilience planning in under-monitored coastal regions facing increasing climate-driven risks.

ACKNOWLEDGEMENTS

This work was supported by the Interreg VI-A Croatia–Bosnia and Herzegovina–Montenegro 2021–2027 programme (Priority Axis: Green investment in environmental protection and efficient risk management) through the European Regional Development Fund, as part of the project *"Improving Coastal Areas' Resilience to Climate Change Impacts and Setting up Guidelines for Sustainable Beach Stabilisation and Management"* (ClimBeach).

REFERENCES

Adriagate (n.d.). *Trstenica Beach, Orebic, Croatia*. Available at: https://www.adriagate.com/Croatia-en/Trstenica-beach-Croatia (Accessed: May 2, 2025).

BeachSearcher (n.d.). *Pizana Beach, Budva, Montenegro*. https://beachsearcher.si/sl/beach/499201056/pizana-beach (Accessed: April 4, 2025).

Bonaldo, D., Bucchignani, E., Pomaro, A., Ricchi, A., Sclavo, M., & Carniel, S. (2020). Wind waves in the Adriatic Sea under a severe climate change scenario and implications for the coasts. *International Journal of Climatology*. https://doi.org/10.1002/joc.6524

Croatian Hydrographic Institute (HHI), 2019. *Tide tables - Adriatic Sea - East coast*.

Direct-Croatia.com. *Vučine Beach*. https://www.direct-croatia.com/apartments/vucine-beach-zuljana (Accessed: June 2, 2025).

Dixon, A., Oh, C., & Draper, J. (2012). Access to the beach. *Journal of Travel Research*, https://doi.org/10.1177/0047287512451136

ERA5-Assimilation module https://help.marine.copernicus.eu/en/articles/5327052-is-era5-data-used-in-copernicus-marine-products

European Marine Observation and Data Network (EMODnet)https://emodnet.ec.europa.eu/en/physics%23approach

Ewing, L. (2015). Resilience from coastal protection. *Philosophical Transactions of the Royal Society A: Mathematical, Physical and Engineering Sciences*. https://doi.org/10.1098/rsta.2014.0383

Gallina, V., Torresan, S., Zabeo, A., Rizzi, J., Carniel, S., Sclavo, M., & Critto, A. (2019). Assessment of climate change

impacts in the North Adriatic coastal area. https://doi.org/10.3390/w11061300
Google Earth (2022). *Plavi Horizonti Beach, Montenegro – Historical Imagery*. https://earth.google.com
Guide to Europe (n.d.). *Jaz Beach, Montenegro*. Available at: https://guidetoeurope.com (Accessed: June 2, 2025).
H Miličević, D Carević, D Bujak (2022). Učinkovitost detekcije obalne linije pomoću video sustava: primjer plaže Ploče u Rijeci. *8. simpozij doktorskog studija građevinarstva*.
Korres, G., Ravdas, M., Denaxa, D., & Sotiropoulou, M. (2021). *CMCC/MEDSEA_MULTIYEAR_WAV_006_012_MEDWAM3I* https://doi.org/10.25423/cmcc/medsea_multiyear_wav_006_012 (Accessed: March 3, 2025).
Larissa (2016). *Exploring Ravno, Neum & Beaches of Bosnia & Herzegovina (incl. Meredek Beach)*. https://fromlarissawithlove.com/2016/09/16/via-dinarica-exploring-ravno-neum-beaches-bosnia-herzegovina/ (Accessed: February 20, 2025).
Mangor, K., Drønen, N.K., Kærgaard, K.H., Kristensen, S.E. (2017). *Shoreline management guidelines*. DHI ebooks.
Marinas.com, *Janska Marina, Janska, Croatia*. Retrieved June 2, 2025, from https://marinas.com/view/marina/g9c8jr1_Janska_Marina_Janska_Croatia
Mathworks Inc. (2024). *MATLAB, version R2024b*.
Nordstrom, K. F. (2000). Beaches and Dunes of Developed Coasts. Cambridge University Press. https://doi.org/10.1017/CBO9780511549519
Pikelj, K., Ružić, I., Ilić, S., James, M. R., Kordić, B. (2017). Implementing an efficient beach erosion monitoring system for coastal management in Croatia. *Ocean & Coastal Management*, 148, 243–256. https://doi.org/10.1016/j.ocecoaman.2017.11.019
Roland, A. (2015). *Analysis of the morphodynamics of Orebic and perspectives for the future coastal protection and coastal management*. https://doi.org/10.13140/RG.2.2.23175.75682
Sveučilište u Zagrebu, Građevinski fakultet (2022). *Studija upravljanja rizicima od poplava mora (VEPAR) – UPRIMO: Završno izvješće*, p. 30. Hrvatske vode.
Šepić, J., Pasarić, M., Međugorac, I.,Vilibić, I.,
Karlović, M., & Mlinar, M. (2022). Climatology and process-oriented analysis of the Adriatic sea level extremes. Progress in Oceanography, 209, 102908. https://doi.org/10.1016/j.pocean.2022.102908.T Bogovac, D Carević, D Bujak, V Novaković (2023). Analysis of beach nourishment and construction in Croatia. *Građevinar*.
Torresan, S., Gallina, V., Gualdi, S., Bellafiore, D., Umgiesser, G., Carniel, S., & Critto, A. (2019). Assessment of climate change impacts in the North Adriatic coastal area. https://doi.org/10.3390/w11061157
University of Split, Faculty of Civil Engineering,Architecture and Geodesy. Available at: https://gradst.unist.hr/eng/research/projects/interreg/climbeach
Visual Crossing (2020). *How We Process the NOAA Integrated Surface Database Historical Weather*. (Accessed: May 2, 2025)

DOI: https://doi.org/10.53256/COSE_240103

Damage Evolution Formulation: A New Approach

Rute Lemos[a*], Ana Mendonça[a], Conceição J.E.M. Fortes[a], Carolina Martinez[a], Helder Girão[b] Tiago Lopes[b], Lucas Brito[c]
[a] *LNEC - National Laboratory for Civil Engineering, Lisbon, Portugal*
[b]*ISEC - Instituto Superior de Educação e Ciências, Lisbon, Portugal*
[c]*ISEL - Instituto Superior de Engenharia de Lisboa, Lisbon, Portugal*

[*] *Corresponding author: Address: LNEC, Avenida do Brasil 101, 1700-066 Lisboa, Portugal; email: rlemos@lnec.pt*

ABSTRACT: One of the most influential contributions to damage progression formulations was introduced by Melby and Kobayashi. Their initial model was published in Melby and Kobayashi (1988a, b) and subsequently reformulated in Melby and Kobayashi (1999) to allow for non-zero initial damage values. A comprehensive description of these developments is provided in Melby (1999). The formulation predicts damage evolution in rubble mound breakwaters (RMBs) with rock-armoured layers, based on erosion measured in physical scale-model tests and on the characteristics of the incident wave conditions. However, the applicability of this formulation is limited to rock armour layers and to the range of sea states investigated in the original experiments.The present work revisits the Melby and Kobayashi damage evolution formulation and investigates its extension to rubble mound breakwaters armoured with tetrapods. A first approach was previously undertaken using a two-dimensional scale model of a section of the Ericeira breakwater (Lemos et al., 2023), leading to the calibration of new coefficients for the Melby formulation ($a_p = 0.03$ and $b = 0.16$). The objective of the present study is to further adjust these coefficients for comparable sea states while accounting for three-dimensional effects on damage evolution, including frontal wave attack.To this end, a long-duration test series (Series A) and two additional series with limited test durations (Series B and C) were conducted using a 1:65 three-dimensional physical model of the Ericeira harbour breakwater. The eroded volume of a selected section of the armour layer was measured using a Kinect position sensor. The damage parameter values obtained from the three-dimensional experiments are higher than those predicted by the formulation derived from the two-dimensional tests (Lemos et al., 2023).Based on the three-dimensional experimental results, new values of the coefficients $a_p$and $b$for the Melby and Kobayashi formulation were determined by minimising the root mean square error between measured and predicted damage. The predictive relationships proposed by Melby and Kobayashi (1988a, b), calibrated with $a_p = 0.025$and $b = 0.30$for the present test programme and accounting for three-dimensional effects associated with bathymetry, are shown to provide a reasonable description of damage evolution, with deviations remaining within an acceptable standard deviation

1 INTRODUCTION

Rubble-mound breakwaters are the most common type of breakwaters in Portugal, being suitable for regions with severe wave conditions. They have an approximately trapezoidal cross-section, consisting of a core of stones covered by large rock armor or concrete blocks (Fig. 1). The progressive nature of their failure, mainly in the armour layer, is one of their characteristics, allowing for timely repairs.

Given the unpredictable nature of wave impacts on RMBs, the potential effects of climate change, the significant investment required for their construction, and their important role in safeguarding ports, it's essential to monitor the performance of RMBs regularly. This helps to identify maintenance and repair needs, avoiding higher risks or costs.

Figure 1. Breakwater armour layers composed of: (a, b) concrete units (Ericeira and Sines); (c) rock units (Vila Praia de Âncora)

The study of damage progression in rubble-mound breakwaters has advanced considerably over recent decades, driven by improvements in theoretical modelling, empirical research, and experimental techniques. Damage assessment in RMBs is influenced by factors such as structural geometry, design specifications, and the type of armour units employed. Damage is typically characterised by the degree of reshaping within the armour layer and is associated with the prevailing failure mode. Quantification may be based on the volume of eroded material or the number of displaced armour units (Campos et al., 2020).

To accurately evaluate breakwater stability, an appropriate damage descriptor must be selected. One widely used approach is displacement counting, in which damage (D) is related to different types of armour unit movement, including rocking. The number of displaced units is commonly normalised by the total number of units within a vertical strip of width equal to the nominal diameter (D_n), extending from the toe to the crest of the armour layer. Van der Meer (1988) introduced the parameters N_{od}(units displaced out of the armour layer) and N_{or}(rocking units); however, these parameters are limited by their dependence on slope length and strip geometry (CEM, 2011).

An alternative and widely adopted damage descriptor is the dimensionless damage parameter

$$S = \frac{A_e}{D_{n50}^2},$$

originally introduced by Broderick (1983), where $A_e$represents the eroded area and $D_{n50}$is the nominal median armour diameter.

Early insights into breakwater stability were provided by Hudson (1958), whose formula offered a basic static method for determining armour unit size as a function of wave height and structure slope. While foundational, Hudson's approach assumes a deterministic structural response and does not account for the progressive accumulation of damage, thereby limiting its applicability for long-term performance assessment under sustained wave loading.

A major advancement was achieved by Van der Meer (1988a), who proposed a semi-empirical model capable of capturing gradual damage accumulation due to repeated wave action. This approach incorporated key parameters such as wave height, wave period, and structural permeability, with the damage parameter Sserving as a central indicator of armour unit displacement. This marked a transition from static to dynamic damage assessment.

Further progress was made by Melby and Kobayashi (1999), who developed a wave-by-wave damage accumulation model that explicitly accounts for the stochastic and cumulative effects of individual wave impacts. Their formulation recognises that each wave contributes incrementally to structural deterioration. A comprehensive description of this methodology is provided in Melby (1999).

More recently, Lemos et al. (2023) conducted several test series using a two-dimensional physical scale model of a section of the Ericeira breakwater. Following the methodology proposed by Melby (1999), that study revisited the damage evolution formulations of Melby and Kobayashi and extended their applicability beyond rock armour layers by developing a predictive formulation for tetrapod armour units. Long-duration tests were performed using a 1:50 scale model of the quay section of the Ericeira Harbour breakwater, with eroded armour volumes measured using a Kinect position sensor. The measured damage values were lower than those predicted by formulations calibrated for rock armour, reflecting the smoother and slower damage progression typically observed in tetrapod armour layers.

Based on those results, new coefficients a_p and b for the Melby formulation were calibrated for the tested tetrapod armour layer by minimising the root mean square error between measured and predicted damage. The adjusted coefficients were $a_p = 0.030$and $b = 0.16$.

The present study aims to further refine these empirical coefficients by conducting tests under comparable sea states using a three-dimensional physical scale model, thereby accounting for three-dimensional effects associated with bathymetry and wave attack. To this end, three test series were performed using a 1:65 three-dimensional scale model of the Ericeira Harbour breakwater. Although bathymetric changes in the vicinity of rubble-mound structures located in the surf zone can significantly influence damage evolution (Yuksel and Kobayashi, 2022), as is the case for the Ericeira breakwater, the present model was constructed on a fixed bottom. This represents a common simplification in stability

studies when sedimentological processes are not the primary focus.

In addition, three-dimensional surveys of the armour layer were conducted using a Kinect position sensor to characterise damage evolution with high spatial resolution.

Following this introduction, the Materials and Methods section describes the Melby-based methodology, the experimental setup, and the measurement procedures adopted in the physical model tests of the Ericeira breakwater. The experimental results are presented and discussed in Section 3, and the main conclusions of the study are summarised in Section 4.

2 MATERIALS AND METHODS

2.1 *Formulae for Armour Layer Damage Evolution*

Burcharth and Hughes 2011 explain that the stability of an armour layer can be assessed through the ratio between destabilising and stabilising forces. This ratio is expressed by the stability number N_s, a dimensionless indicator of armour stability that should be kept as low as possible to ensure a stable armour layer. Based on laboratory experiments, the stability number can be written:

$$N_s = \frac{H}{\Delta D_{n50}} < f(K, p_1, p_2, \dots, p_n) \quad (1)$$

where:

- H is a characteristic wave height of the incident sea state;
- Δ is the submerged density of the armour layer material;
- D_{n50} is the median nominal diameter of the armour layer units;
- p_1 to p_n are dimensionless parameters associated with the n+3 physical quantities considered in the tests
- K is an experimentally determined coefficient that reflects the influence of physical quantities not considered in the tests (Munson et al. 2009).

The most widely recognised empirical stability model was introduced by Hudson (1958), based on scale-model tests with regular, non-overtopping waves and armour layers composed of rock or tetrapod units:

$$N_s = (K_D \cot\alpha)^{1/3} \quad (2)$$

where α is the angle of the armour layer slope relative to the horizontal plan and K_D is the stability coefficient, a tabulated constant specific to each armour unit type and corresponding to a given percentage of damage at the end of the test. Damage in Hudson's formulation is defined by the volume of armour units displaced from the active zone of the breakwater, which extends from the mid-crest down the seaward slope to a depth approximately equal to the wave height.

Building on Hudson's formulation, Van der Meer (1985, 1988a) introduced a stability model for rock-armoured slopes that incorporates wave period effects through the Iribarren number (ξ_0), the number of waves (N_W), and core permeability (P):

$$N_s = 6.2\,\xi_o^{-0.5} P^{0.18} \left(\frac{S}{\sqrt{N_W}}\right)^{0,2} \quad for\ plunging\ waves \quad (3)$$

$$N_s = 1.0\,\xi_o^{P} \sqrt{\cot\alpha}\ P^{-0.13} \left(\frac{S}{\sqrt{N_W}}\right)^{0,2} \quad for\ surging\ waves \quad (4)$$

In both equations the dimensionless damage parameter, $S=A_e/(Dn_{50})^2$ is used, where A_e is the eroded area of the profile and Dn_{50} is the equivalent cube length.
Subsequently, Van der Meer (1988b) developed formulations applicable to cubes, tetrapods, and accropodes. Since the parameter S is not the most appropriate damage descriptor for these armour elements, Van der Meer adopted the parameter N_0, defined as the number of units displaced from the armour layer within a strip of width equal to one equivalent cube length, following the approach originally proposed by Hedar (1960).
In 1999, Melby developed a damage evolution model based on long-duration laboratory tests to predict the progression of damage in a rock-armoured layer starting from an undamaged state ($S = 0$) at time $t = 0$, when exposed to constant wave conditions characterised by significant wave height H_s and mean period T_m.

$$S = a \left(\frac{H_s}{\Delta D_{n50}}\right)^5 \left(\frac{t}{T_m}\right)^b \quad (5)$$

In this expression, a and b are empirical parameters calibrated from scale-model test results. To extend the model to sequences of sea states with variable wave conditions, Melby and Kobayashi (1999) differentiated Eq. (5) with respect to time and integrated the result over a finite interval $t_n \le t \le t_{n+1}$, during which the wave parameters can be assumed constant (or characterised by spectral parameters H_{m0} and T_p):

$$S(t) = S(t_n) + a_p \left(\frac{H_{m0}}{\Delta D_{n50}}\right)^5 T_p^{-b}\left(t^b - t_n^b\right)$$

$$\text{for } t_n \le t \le t_{n+1} \quad (6)$$

This formulation allows for non-zero initial damage, with $S(t_n)$representing the accumulated damage at time t_n. The coefficients $a_p$and $b$are empirical parameters obtained from experimental data. Based on scale-model tests of a rock-armoured rubble-mound breakwater, Melby (1999) proposed values of a_p=0.0202 and b=0.25.

Melby's experimental programme comprised three test series with peak wave periods of 2.48 s and 2.59 s and significant wave heights ranging from 0.098 m to 0.158 m. The longest series (Series A) aimed to verify damage stabilisation under successive sea states with constant characteristics. Each test condition, defined by a specific combination of wave height and period, was repeated until the number of displaced armour units remained unchanged in two consecutive tests. The programme then progressed to conditions with higher wave energy to assess long-term structural response.

Test Series B and C were of shorter duration. Series B examined increasing water levels and peak periods, whereas Series C investigated decreasing values of these parameters, with the aim of evaluating damage development under varying wave conditions.

The tested breakwater had a slope of 1:2 and an armour layer composed of rock units weighing 0.128 kgf (1.25 N), with a nominal diameter $D_{n50} = 0.034$m. Damage assessment was performed using a mechanical profiler equipped with eight arms to survey individual cross-shore profiles. The damage parameter S for each test was computed as the average value obtained from the eight profiles. This approach becomes less reliable as the number of surveyed profiles decreases, whereas increasing the number of profiles covering the entire slope reduces associated uncertainties.

In comparison with the Van der Meer formulations (Eqs. 3 and 4), Melby's formulation (Eq. 5) does not include the Iribarren number. Consequently, the slope of the armour layer is not explicitly accounted for, and the empirical coefficients $a_p$and $b$must be recalibrated to represent damage evolution for different slopes and armour types. Furthermore, when armour units other than rock are employed, coefficients calibrated for rock armour layers are not directly applicable.

As a first step towards adapting Melby's coefficients to armour layers composed of units other than rock, a procedure based on the derivation of Eq. (6) presented in Melby (1999) was adopted. Within the time interval $t_n \leq t \leq t_{n+1}$, assuming constant wave conditions, the following expressions can be written:

$$S_{n+1} = a_p \left(\frac{H_{m0}}{\Delta\, \mathrm{D_n}}\right)^5 \left(\frac{t_{n+1}}{T_p}\right)^b \quad (7)$$

$$S_n = a_p \left(\frac{H_{m0}}{\Delta\, \mathrm{D_n}}\right)^5 \left(\frac{t_n}{T_p}\right)^b \quad (8)$$

Dividing S_{n+1} by S_n and applying logarithms to calculate b yields:

$$b = \frac{\ln\left(\frac{S_{n+1}}{S_n}\right)}{\ln\left(\frac{t_{n+1}}{t_n}\right)} \quad (9)$$

In terms of Melby´s expression, the coefficient a_p can then be determined as:

$$a_p = \frac{S_{n+1} - S_n}{\left(\frac{H_{m0}}{\Delta\, \mathrm{D_n}}\right)^5 \left[\left(\frac{t_{n+1}}{T_p}\right)^b - \left(\frac{t_n}{T_p}\right)^b\right]} \quad (10)$$

For tests conducted under similar wave conditions, the estimated values of b and a_p should exhibit limited variability. Averaging the values obtained across all test conditions provides an initial estimate of the coefficients for the tested structure. Subsequently, the optimal values of a_p and b can be determined by minimising the root mean square error between measured and predicted damage.

The present study focuses on recalibrating these empirical coefficients to improve damage evolution predictions for breakwaters armoured with tetrapods. In particular, the coefficients previously adjusted by Lemos et al. (2023) are validated and refined under wave conditions influenced by bathymetry, using experimental data from three-dimensional surveys of the Ericeira breakwater, which serves as a representative case study for similar coastal structures.

2.2 *Case study: Ericeira breakwater*

The Ericeira breakwater, constructed in the 1970s, is located on the western coast of Portugal and serves as a key coastal defence structure, protecting the town's harbour from Atlantic wave action and storm events (Fig. 2). Situated in a region renowned for fishing and surfing activities, Ericeira relies on the breakwater to safeguard both critical infrastructure and maritime operations.

Over the years, the structure has undergone several major repair interventions, particularly following severe storm events in the 1990s, 2001, 2007, 2013, and 2018. These rehabilitation works included the replacement of displaced armour units, replenishment of core materials, and reinforcement of the breakwater to improve resistance to future wave impacts. Continuous

maintenance remains essential to ensure the long-term effectiveness of the structure in harbour protection.

2.3 *Experimental set-up and test conditions*

The experimental study was carried out at the Ports and Maritime Structures Unit (NPE) of the Hydraulics and Environment Department of the National Laboratory for Civil Engineering (LNEC), in Lisbon, Portugal. Experiments were conducted in a wave basin measuring 46.6 m in length, 20.6 m in width, and 1.5 m in depth, equipped with a piston-type wave generation system. The physical model represents the port basin up to the harbour entrance (Fig. 2).

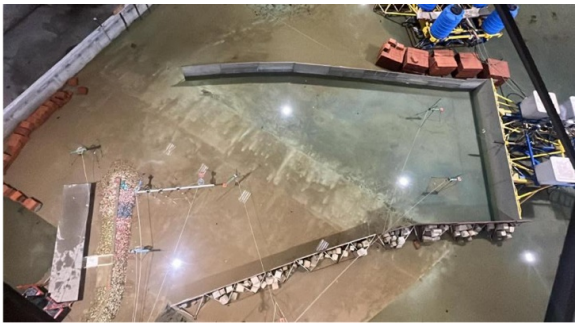

Figure 2. Physical model of the Ericeira breakwater.

The model was constructed and operated at a geometric scale of 1:65, following Froude similarity. The tested breakwater has a 2:3 slope and a two-layer rock filter covering the core. The armour layer of the breakwater sections (Fig. 3a) is composed of:

- Trunk: 300 kN tetrapods with a nominal diameter of 0.034 m and a porosity of 0.45;
- Head: 550 kN Antifer cubes with a nominal diameter of 0.042 m and a porosity of 0.30.

The selected scale of 1:65 reflects a compromise between the dimensions of the experimental facility and the spatial extent of the coastal area of interest.

Dissipative beaches were installed along the basin sidewalls to minimise unwanted wave reflections.

The experimental instrumentation included eight resistive wave gauges (Fig. 3b) used to measure free-surface elevation. A Kinect position sensor was employed to survey the armour layer geometry at the beginning of the test programme and after each individual test, allowing detailed assessment of damage evolution.

a)

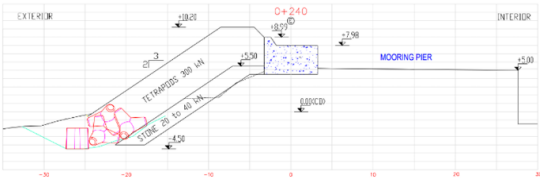

b)

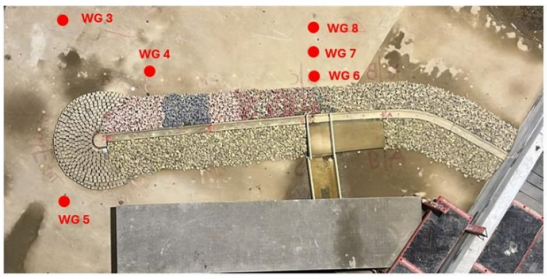

Figure 3. a) Trunk cross-section. b) three-dimensional scale model and wave gauge locations

2.4 *Wave conditions*

The tested wave conditions were defined based on hindcast data and buoy measurements. They correspond to peak wave periods of $T_p = 14$s and $T_p = 16$s, associated with High Water Level (HWL) and High Water Level with set-up (HWLS), respectively. Significant wave heights of $H_s = 5$, 6, and 7 m were considered, with a north-westerly (NW) wave direction, corresponding to an almost frontal wave attack on the breakwater (Fig. 4).

These conditions encompass the expected range of sea states acting on the structure, including extreme events and potential effects of climate change on wave characteristics and water levels.

Three test series were conducted in the experimental programme (Table 1). Test Series A, with a duration of 30 hours (model scale), was designed to provide insight into the long-term deterioration of the structure, up to near-failure conditions.

Given the characteristics of the armour layer units (tetrapods), their interlocking capacity, and the durability required throughout the structure's service life—particularly before emergency intervention becomes necessary—the tests were extended slightly beyond the failure threshold defined by Melby and Kobayashi (1998). In their study, failure was defined as exposure of the underlayer through a hole with a diameter of at least D_{n50}. In the present study, the adopted criterion lies between the Initiation of Damage and Destruction, as defined by Losada et al. (1986) and Vidal et al. (1991).

In Test Series A, testing was interrupted when the analysed section of the breakwater approached a

condition in which it no longer complied with its required level of service. At the end of this series, approximately four to five armour units from the lower layer had been displaced, and the underlayer was partially exposed to wave action.

Table 1. Water levels and wave conditions for test series A, B, and C (model scale values)

Series	Test	T_p (s)	Hm0 (m)	Depth at the toe (m)	Number of test runs
A	1	1.74	0.08	0.14	Until damage stabilisation
	2	1.74	0.09	0.14	
	3	1.74	0.10	0.14	
	4	1.99	0.09	0.17	
	5	1.99	0.10	0.17	
B	1	1.74	0.08	0.14	1
	2	1.74	0.09	0.14	4
	3	1.74	0.10	0.14	4
	4	1.99	0.09	0.17	4
	5	1.99	0.10	0.17	2
C	4	1.99	0.09	0.17	4
	5	1.99	0.10	0.17	2
	1	1.99	0.08	0.14	4
	2	1.74	0.09	0.14	4
	3	1.74	0.10	0.14	4

The model structure was exposed sequentially to wave conditions 1 to 5 until damage stabilisation was observed. Wave conditions 1 to 3 correspond to HWL, whereas conditions 4 and 5 correspond to HWLS. In both cases, wave height increased progressively from condition 1 to 3 and from condition 4 to 5. Transitions between wave conditions were implemented once the damaged armour profile exhibited stabilisation.

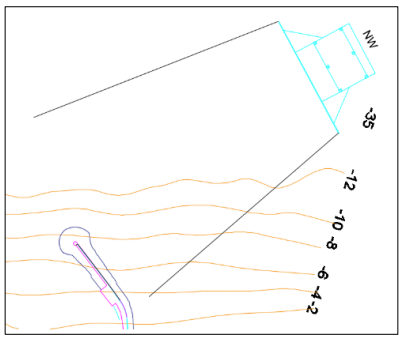

Figure 4. Detail of the three-dimensional model installation in the wave basin, including bathymetry.

2.5 *Methodology for damage evolution quantification*

In the present study, the dimensionless damage parameter, $S = Ae/D_n^2$ was adopted, where A_e represents the eroded area of the armour profile and D_n denotes the nominal diameter of the tetrapod units. The parameter Smay be interpreted as the number of squares with side length D_{n50} required to cover the eroded area.

Recent advances in three-dimensional survey techniques, including LiDAR, photogrammetry, and artificial vision algorithms, have enabled the combined use of multiple damage descriptors. Given the complexity of defining representative surface profiles for tetrapod armour layers, damage parameters based solely on two-dimensional profiles are less suitable. To overcome this limitation, the mean eroded area was computed from the total eroded volume of the armour layer.

Specifically, the section-averaged eroded area (A_e) was obtained by dividing the eroded volume (E_v) measured at the end of each test by the width of the analysed stretch (X).

The dimensionless damage parameter S was subsequently calculated from this averaged eroded area. To minimise errors associated with spatial averaging, the analysis was restricted to the zone exhibiting the highest damage concentration.

Damage assessment was based on eroded volume measurements derived from surveys performed using a Kinect V2 position sensor. The sensor was mounted on a tripod and positioned approximately 2 m from the crest of the structure (Fig. 5a). The survey parameters included a voxel resolution of 512 points along each of the three spatial axes (x, y, z), corresponding to 256 voxels per metre. As a result, each scanned scene covered a volume of 2 m × 2 m × 2 m. The effective acquisition range of the sensor was between 0.5 m and 8 m.

Kinect surveys were carried out without water in the wave tank at the beginning of the test programme and at the end of each test series, and with water in the tank at the end of each intermediate test. In addition, traditional visual counting of rocking and displaced armour units was performed, when possible, to support calibration of the grid resolution used during point-cloud post-processing.

To reference the point clouds obtained from the Kinect surveys—i.e. to transform coordinates from the sensor reference frame to a coordinate system fixed to the flume bottom—70 ground control points (GCPs) were employed. These GCPs consisted of coloured markers placed on the flume bottom in front of the toe of the structure and on the superstructure (Fig. 5b). Their coordinates were measured using a total station prior to the start of the experimental programme.

Figure 5. (a) Kinect position sensor; (b) ground control points

This referencing procedure also facilitates correction of distortions caused by light refraction at the air–water interface during surveys conducted with water in the tank. Such refraction correction is only possible when submerged GCPs are detected by the sensor, enabling correction of rotational misalignment. A similar approach was adopted by Musumeci et al. (2018) in their Kinect-based surveys of scale-model rubble-mound breakwaters.

Post-processing of the surveys conducted with water in the flume also included a fine alignment of the resulting point clouds with reference clouds obtained without water. This alignment was performed using the iterative closest point (ICP) algorithm (Chen et al., 1992), implemented in the open-source software CloudCompare (Girardeau-Montaut, 2006). For each point in the cloud obtained with water, the ICP algorithm identifies the closest corresponding point in the reference cloud and estimates the optimal combination of rotation and translation that minimises the root mean square (RMS) point-to-point distance.

The algorithm iterates until a stopping criterion is met, defined either by an RMS threshold or a maximum number of iterations. In the present study, an RMS tolerance of 10^{-5}m was adopted, corresponding to a near-complete final overlap, as recommended by the software.

Eroded volume computation was based on gridding of the point clouds, which defines the size of the elementary cells used in volume estimation. CloudCompare computes the eroded volume by summing the volumes of elementary parallelepipeds whose base area corresponds to the grid cell area and whose height equals the vertical difference between corresponding points in the two clouds (*dV = grid step * grid step * distance)*.

Prior to final volume computation, calibration of the grid size was performed using tests involving the removal of a small number of armour units. This procedure aimed to identify a grid resolution yielding eroded volume estimates consistent with visually counted displaced units. After testing grid steps ranging from 1.0 mm to 2.0 mm, an optimal grid size of 1.4 mm was selected, providing the best compromise between point density and depth resolution.

The novelty of the present damage evaluation methodology lies in the use of three-dimensional surface models of the armour layer to compute eroded volume from differences between successive surveys and, from this, derive the eroded area (A_e) and the dimensionless damage parameter S. In this study, A_e was obtained by dividing the total eroded volume by the length of the analysed stretch. This simplification is justified for structure sections where damage is spatially homogeneous, as in the present case. Although damage parameters could alternatively be derived from individual profiles extracted from the point clouds, the homogeneous nature of damage observed in the study area motivated the use of a volume-based approach rather than profile-based estimates.

Interactions among individual concrete armour units under breaking wave action are highly complex (Xiang et al., 2022). Consequently, the use of eroded volume and area as proxies for damage may introduce uncertainties in the calculation of S. Accurate knowledge of armour layer porosity—particularly at the beginning of the test programme—and careful calibration of the grid resolution are therefore essential to minimise potential over- or underestimation of the damage parameter.

3 RESULTS AND DISCUSSION

The results presented in this section refer to test series A and B. Test series C is currently under analysis. Table 2 summarises the number of tests performed for each test series.

Damage evaluation in this study focuses on the most severely affected zone of the breakwater, corresponding to a stretch of the trunk located near the head of the structure. Owing to wave transformation induced by the local bathymetry, this area experienced the highest damage levels. The analysed stretch had a width $X$of 0.53 m for test series A and 0.64 m for test series B (Fig. 6**Errore. L'origine riferimento non è stata trovata.**).

Table 2. Number of tests for each test series

Series	Test	Test repats until stabilization	Test names
A	1	3	T1-T3
	2	19	T4-T22
	3	26	T23-T45
	4	7	T46-T52
	5	2	T53-T54
	1	1	T1
	2	4	T2-T5

B	3	4	T6-T9
	4	4	T10-T13
	5	2	T14-T15

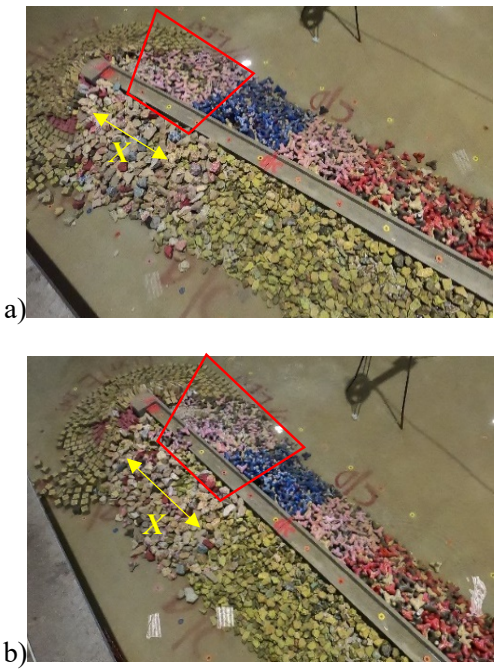

a)

b)

Figure 6. Overview of the model at the end of test series A (a) and B (b)

It should be noted that the eroded area represents an average value; individual profiles may exhibit variability due to the spatial heterogeneity of damage distribution. Figures 7 and 8 present the point clouds obtained from Kinect© sensor surveys conducted at the beginning and end of test series A (T3, T22, T45, and T54) and test series B (T4, T8, T12, and T15), respectively. Corresponding distance maps between the initial and final surveys are also shown.

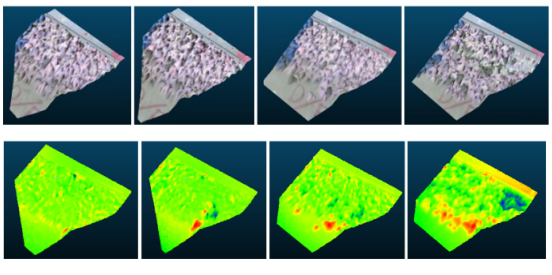

a)

b)

Figure 7. Surveys for tests T3, T22, T45, and T54 of test series A: (a) point clouds; (b) distance map (blue: erosion; red: deposition)

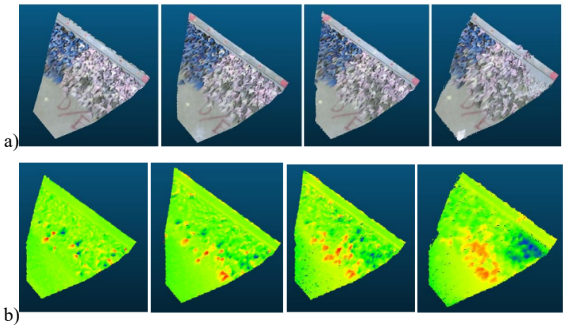

a)

b)

Figure 8. Surveys for tests T4, T8, T12, and T15 of test series B: (a) point clouds; (b) distance map (blue: erosion; red: deposition)

For test series A (Fig. 9a), damage progression increased with rising water levels and peak wave periods. At the end of the high-water level (HWL) tests, and according to the qualitative damage thresholds defined by Losada et al. (1986) and Vidal et al. (1991), the damage level remained within the *Damage Initiation* category. However, following the high-water level with set-up (HWLS) tests, the damage escalated to the *Destruction* category.

In test series B, damage evolved more gradually, influenced by both water level and peak period, and increased with significant wave height (Fig. 9b). At the end of the HWL tests, the damage corresponded to the *Iribarren damage* classification, characterised by significant exposure of the lower tetrapod layer. As in test series A, the HWLS tests led to damage reaching the *Destruction* category. In both test series, damage was predominantly concentrated in the upper portion of the armour layer.

Figure 11 compares measured and predicted values of the dimensionless damage parameter S, using coefficients $a_p = 0.03$and $b = 0.16$proposed by Lemos et al. (2023) for test series A. These coefficients were derived from two-dimensional scale model tests with similar prototype wave conditions and identical cross-sectional geometry.

As expected, results from the three-dimensional physical model do not converge with those obtained from the two-dimensional formulation. Predicted values consistently underestimate the measured damage, particularly towards the end of the test programme. This discrepancy is primarily attributed to:
(a) three-dimensional effects associated with bathymetric reproduction in the physical model; and
(b) differences in armour unit scaling and stability.

The 2D model was conducted at a 1:50 scale, with armour units equivalent to 105 kN in the prototype, deliberately resulting in a less stable armour layer. In contrast, the 3D model was built at a 1:65 scale, with armour units corresponding to their actual prototype weight (300 kN). This led to lower stability numbers and higher damage progression in the 3D model.

To recalibrate the Melby damage evolution coefficients for three-dimensional conditions, constant sea-wave conditions at the structure toe were defined using average values of peak period and significant wave height for each test sequence.

Table 3 summarises the start and end times of each sequence, corresponding damage values, and averaged wave characteristics.

Table 3. Average sea-wave characteristics at the toe of the structure and corresponding damage parameters

Test series A							
Test	Tp (s)	Hm0 (m)	tn (s)	Sn	tn+1 (s)	Sn+1	Nm_0
1	1.67	0.05	0	0	5208	0.6	0.85
2	1.69	0.08	5208	0.5	38192	0.9	1.30
3	1.73	0.10	38192	0.8	78120	1.2	1.57
4	1.63	0.07	80105	1.6	92015	2.6	1.14
5	1.59	0.09	92015	3	99955	3.9	1.45
Test series B							
1	1.73	0.07	0	0	1736	0.5	1.13
2	1.72	0.09	1736	0.50	8680	0.8	1.46
3	1.73	0.10	8680	0.80	15624	1.5	1.59
4	1.75	0.08	15624	1.50	23564	2.4	1.22
5	1.75	0.09	23564	2.40	27534	3.9	1.44

By minimising the root mean square error (RMSE) between measured and predicted damage values over various combinations of $a_p$and b, optimal coefficients were identified within the range defined by the standard deviation of the measured S values (Fig. 9). The standard deviation was computed using all measured damage values obtained at the end of each test run.

An initial optimisation yielded coefficients $a_p = 0.03$and $b = 0.27$for test series A, corresponding to an RMSE of 0.7. Despite this adjustment, the predicted damage trend did not fully reproduce the measured progression.

Analysis of Fig. 9a shows that, during HWL conditions, predicted damage values match measured values reasonably well up to approximately 25,000 waves. Beyond this point, and until the end of the HWL tests (around 45,000 waves), the formulation tends to overestimate the stabilised measured damage. When transitioning to HWLS conditions, the predicted curve fails to capture the abrupt increase in measured damage, resulting in underestimation.

This rapid damage escalation is likely related to increased wave run-up and rundown caused by higher water levels and longer wave periods, leading to energy concentration in the upper part of the slope—where damage was most localised. Such effects are not explicitly accounted for in the formulation and contribute to faster damage evolution than predicted.

Although the formulation was originally intended for life-cycle cost forecasting and not expected to exceed the *Initiation of Destruction* level, the rapid damage progression observed is representative of the Ericeira breakwater case. Consequently, the authors deemed it necessary to further adjust the coefficients to account for rapid damage evolution.

To capture this behaviour, RMSE minimisation was performed separately for HWL and HWLS conditions, maintaining $a_p = 0.03$. The final coefficients obtained were:

- HWL: $a_p = 0.03$, $b = 0.27$(RMSE = 0.33);
- HWLS: $a_p = 0.03$, $b = 0.47$(RMSE = 2.5).

The recalibrated coefficients provide a reasonable agreement between predicted and measured damage values for test series A (Fig. 9b).

Validation using test series B confirmed the applicability of the proposed coefficients. As shown in Fig. 10, predicted damage values exhibit reasonable agreement with measured data, with RMSE values of 1.7 for HWL and 4.18 for HWLS.

Regarding damage initiation, the formulation underestimates damage in test series A but performs satisfactorily for test series B.

a)

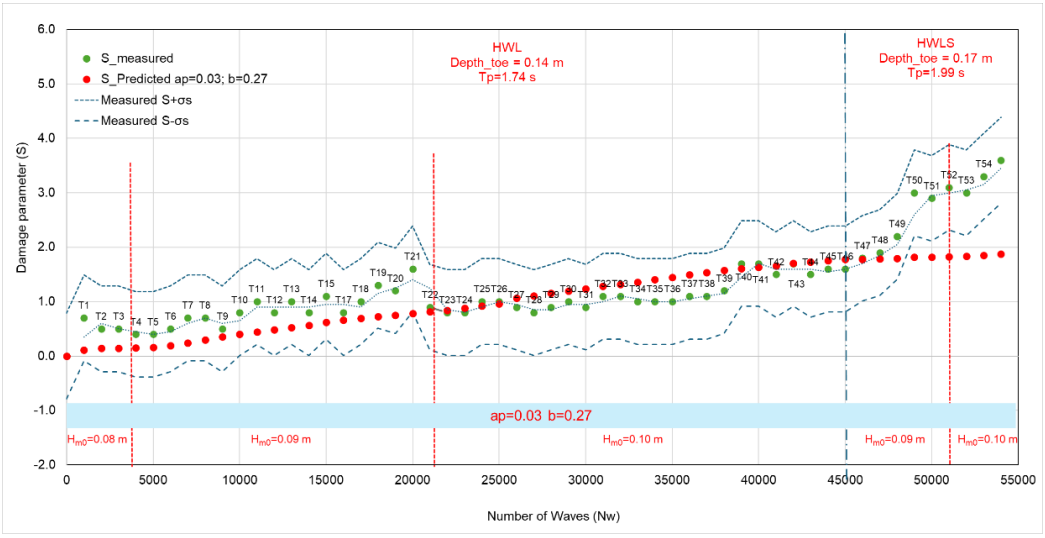

b)

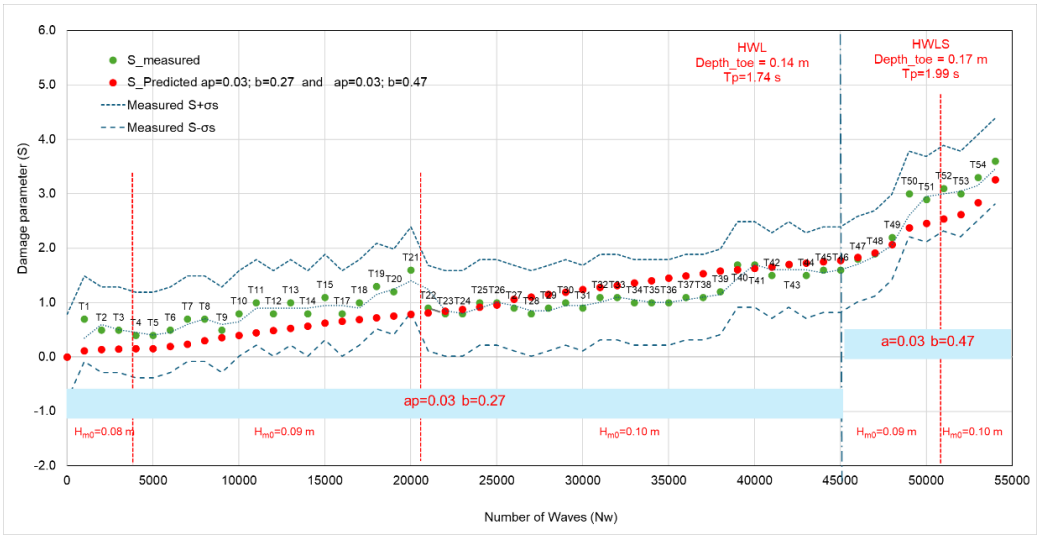

Figure 9. Measured and predicted damage parameter (S) with fitted a_p and b parameters for test series A a) using the same a_p and b parameters for tests with HWL and HWLS b) using readjusted b parameter for tests with HWLS

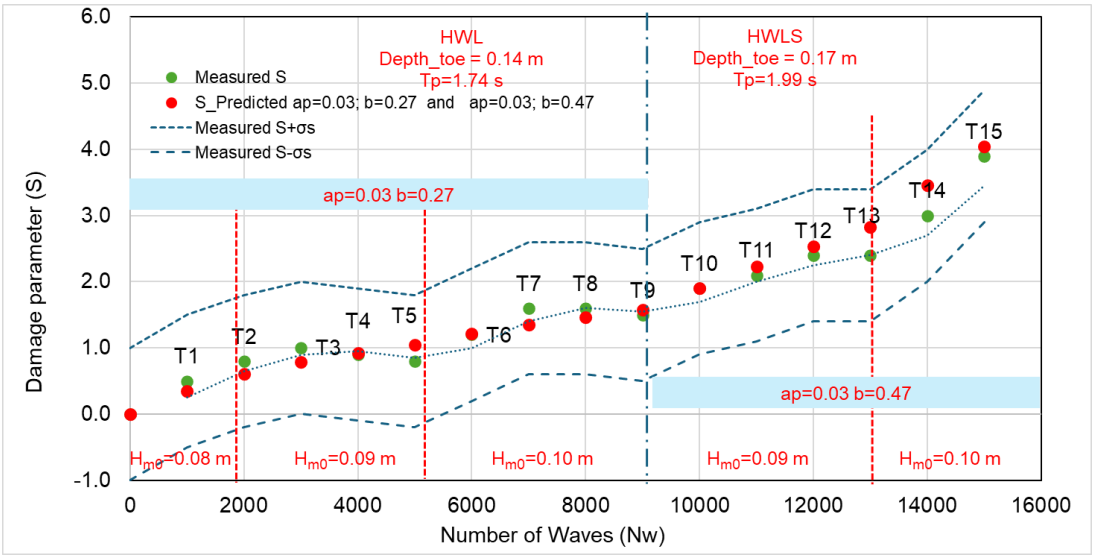

Figure 10. Measured and predicted damage parameter (S) for test series B using readjusted a_p and b parameters

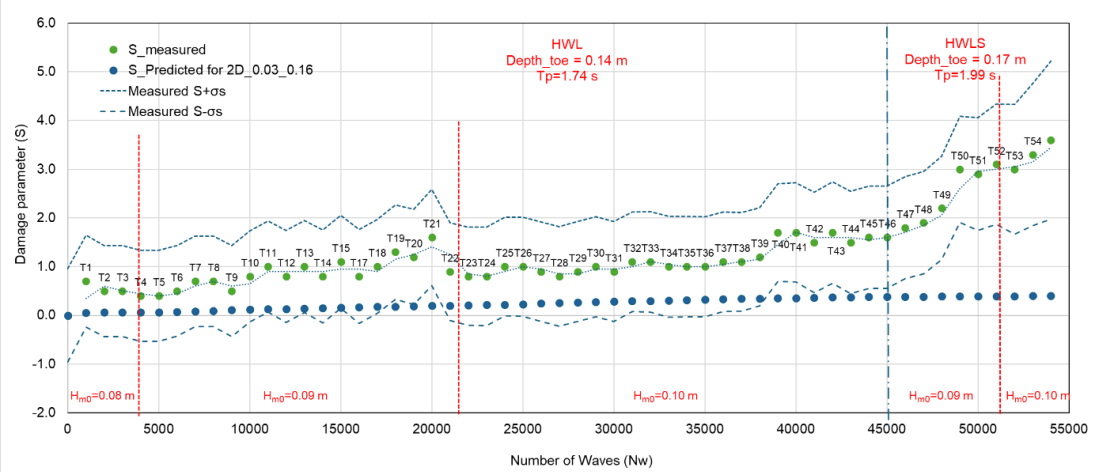

Figure 11. Measured and predicted damage parameter (S) with a_b and b parameters from Lemos et al, 2023

The Melby and Kobayashi predictive model assumes a continuously increasing damage progression at a decreasing rate. In theory, prolonged exposure to small waves between storms may contribute to incremental damage. This behaviour was observed in both test series; however, in test series A, an abrupt increase in damage occurred at the onset of HWLS conditions.

Overall, the Melby and Kobayashi (1988a,b) formulation, fitted for the present test programme, armour layer type, and bathymetric influence, with coefficients $a_p = 0.03$ and $b = 0.27$, adequately describes damage evolution for the relatively low damage levels observed under HWL conditions. For higher damage levels under HWLS conditions, the coefficients $a_p = 0.03$ and $b = 0.47$also provide a reasonable representation of damage trends, despite the associated increase in RMSE.

4 CONCLUSIONS

The present work revisits the damage evolution formulations proposed by Melby and Kobayashi, with the aim of establishing an equivalent formulation for the armour layer damage evolution of rubble-mound breakwaters protected by tetrapods. An initial approach was previously developed using a two-dimensional scale model of a section of the Ericeira breakwater (Lemos et al., 2023). In the present study, those coefficients were further refined by explicitly accounting for three-dimensional effects on damage progression, through three sets of three-dimensional physical model tests.

The characterisation of armour layer damage was based on surveys performed using a position sensor. The use of this sensor proved to be effective in generating three-dimensional surface models of the armour layer, enabling the quantification of damage indicators such as eroded volume and mean eroded area. Although the interaction between individual armour units was not explicitly considered—an inherent simplification that may influence the calculation of the damage parameter S—the adopted methodology provided consistent and reliable damage estimates.

The Melby and Kobayashi (1988a, 1988b) formulation, when recalibrated with the updated coefficients $a_p = 0.03$ and $b = 0.27$, was found to describe the damage evolution satisfactorily for relatively low damage levels, with predictions lying within one standard deviation of the measured values. For higher damage levels, the coefficients $a_p = 0.03$ and $b = 0.47$were shown to capture the overall trend of damage evolution reasonably well, albeit with an increase in the root mean square error (RMSE).

The study demonstrates that long-duration tests can represent a valuable extension of conventional hydraulic stability tests conducted in wave flumes or wave basins, which are typically focused on assessing the behaviour of a proposed rubble-mound breakwater cross-section under design conditions. Using the same experimental setup, the procedure presented herein enables the derivation of the empirical coefficients a_p and b governing armour layer damage evolution.

Once these coefficients are calibrated and combined with knowledge of the local wave

climate at the site of interest, the proposed methodology allows the forecasting of future armour layer damage evolution over the time interval following the most recent periodic inspection. This capability provides a useful tool for supporting maintenance planning and long-term performance assessment of rubble-mound breakwaters protected with concrete armour units.

ACKNOWLEDGEMENTS

This work was supported by the Instituto Superior de Educação e Ciências (ISEC-Lisboa) through the project ProCoast 3D/CPISEC/PID/001/2023-24, within the framework of the COASTLIFE project financed by the Fundação para a Ciência e a Tecnologia (FCT). Additional support was provided by the projects SAFEPORT and WISER, developed within the scope of the *Risk and Safety in Ports and Maritime Structures* Programme of the Research and Innovation Strategy (E2I) 2021–2027 of LNEC

REFERENCES

Broderick, L. (1983). *Riprap Stability*, a Progress Report. In Coast. Struct; ASCE: Reston, VA, USA, 1983; pp. 320–330

Burcharth, H.F.; Hughes, S.A. (2011). Fundamentals of Design. In Coastal Engineering Manual; USACE Publications: Hyattsville, MD, USA.

Campos, A.; Castillo, C.; Molina-Sanchez, R. (2020). Damage in Rubble Mound Breakwaters. Part I: Historical Review of Damage Models. J. Mar. Sci. Eng. 2020, 8, 317.

Chen, Y.; Medioni, G. (1992). Object modelling by registration of multiple range images. *Image and vision computing*, 10.3: 145-155.

Girardeau-Montaut, D. (2006). *Détection de changement sur des données géométriques tridimensionnelles*. PhD Thesis. Télécom ParisTech.

Hedar, P.A. *Stability of Rock-Fill Breakwaters* (1960). Ph.D. Thesis, University of Gothenburg, Gothenburg, Sweden.

Hudson, R.Y. (1958). *Design of Quarry-Stone Cover Layers for Rubble-Mound Breakwaters*; WES: Vicksburg, MS, USA.

Lemos R., Santos J.A., Fortes C.J.E.M. (2023). Damage Evolution Prediction during 2D Scale-Model Tests of a Rubble-Mound Breakwater: A Case Study of Ericeira's Breakwater. *Modelling* 2023 4, 1–17. https://doi.org/10.3390/ modelling4010001

Losada, M.A.; Desire, J.M.; Alejo, L.M.(1986). Stability of Blocks as Breakwater Armor Units. *J. Struct. Eng.* 112, 2392–2401.

Melby, J.; Kobayashi, N. (1998a). Progression and Variability of Damage on Rubble Mound Breakwaters. *J. Waterw. Port., Coastal, Ocean. Eng*, 124, 286–294

Melby, J.A.; Kobayashi, N. (1998b). Damage Progression on Breakwaters. *In Proceedings of the 26th International Conference on Coastal Engineering*, Copenhagen, Denmark, 22–26 June 1998; Volume 2, pp. 1884–1897.

Melby, J.A.; Kobayashi, N. (1999). Damage Progression and Variability on Breakwater Trunks. *In Proceedings of the Coastal Structures*, Santander, Spain, 7–10 June 1999; Volume 1, pp. 309–315.

Melby, J.A. (1999). *Damage Progression on Rubble-Mound Breakwaters*; US Army Corps of Engineers: Washington, DC, USA.

Munson, B.R.; Young, D.F.; Okiishi, T.H.; Huebsch, W.W (2009). *Fundamentals of Fluid Mechanics*, 6th ed.; John Wiley & Son, Inc.: Hoboken, NJ, USA.

Musumeci, R.; Moltisanti, D.; Foti, E.; Battiato, S. (2018). 3-D monitoring of rubble-mound breakwater damages. *Measurement,* 117, 347–364.

United States Army Corps of Engineers (2011). *Coastal Engineering Manual*, USACE: Washington, DC, USA

van der Meer, J.W. (1985). Stability of Rubble Mound Revetments and Breakwaters under Random Wave Attack. *In Proceedings of the Breakwaters Conference*, London, UK, 2–4 October 1985.

van der Meer, J.W. (1988a). *Rock Slopes and Gravel Beaches under Wave Attack*. Ph.D. Thesis, Faculty of Civil Engineering and Geo-sciences, Delft, The Netherlands, 26 April 1988.

van der Meer J.W. (1988b). Stability of Cubes, Tetrapodes and Accropode. *In Proceedings of the Breakwaters Conference*, Eastbourne, UK, 2–4 May 1988; pp. 71–80

Vidal, C.; Losada, M.; Medina, R. (1991). Stability of Mound Breakwater's Head and Trunk. *J. Waterw. Port Coast. Ocean* Eng., 117, 570–587.

Xiang, J., Latham, J.-P. and Higuera, P. (2022). Numerical study of Core-Loc™ breakwater stability under storm wave sea state using a fast wave proxy approach. COSE, Year 1, Volume 2, 6-18.

Yuksel, Z. T., & Kobayashi, N. (2022). Numerical modeling of revetment and sill in reducing shore erosion. COSE, Year 1, Volume 1, 8-19.

DOI: https://doi.org/10.53256/COSE_240104

Numerical Simulation of Ship Accessibility and Safety in Exposed Ports

Pinheiro[a,*] L. V., Fortes[a] C.J., Santos[a] J., Zózimo[a] A. C.
[a]*National Laboratory for Civil Engineering, Lisbon*
[b]*Centre of Marine Technology and Ocean Engineering, Instituto Superior de Engenharia de Lisboa, Lisbon*

[*]*Corresponding author: lpinheiro@lnec.pt*

ABSTRACT: A numerical methodology is presented to assess ship accessibility and navigational safety in exposed ports through the simulation of wave propagation and three-dimensional hydrodynamic flow around the ship hull, accounting for the effects of wind and currents. The proposed methodology is applicable during both the planning and operational phases of port management and provides a quantitative basis for evaluating navigational constraints under adverse environmental conditions.

1 INTRODUCTION

Ports are increasingly challenged to balance economic growth, climate change adaptation, and the ongoing energy transition. The demand for larger vessels requires deeper and wider access channels, while climate change is increasing the frequency and intensity of extreme weather events that directly affect port operations. At the same time, the push towards decarbonisation and sustainable activities—such as offshore wind and other marine renewable energy developments—places additional pressure on ports to adapt and expand their infrastructure. Furthermore, stricter ship safety regulations are being implemented in response to a rising number of maritime incidents. In this context, numerical modelling has become an essential tool for accurately assessing the complex interactions between the ocean environment, port structures, and ships.

During the planning phase, the minimum safety depths and widths of port entrance channels can be defined based on the local wave climate and the characteristics of the vessels using the port. Numerical wave models are used to propagate offshore wave conditions to locations along the access channel, thereby defining the operational wave regime. Three-dimensional simulation models are then employed to evaluate the effects of waves on ship motions. The maximum vertical ship motions are assessed as a function of wave characteristics, allowing the establishment of operability thresholds and the determination of minimum channel dimensions required to satisfy under-keel clearance (UKC) criteria.

During the operational phase, the proposed methodology is applied to evaluate safety conditions for vessels entering or leaving the port. This assessment is based on short-term forecasts of wind, wave, and sea-level conditions. Numerical models, such as SWAN and Boussinesq-type models, are used to propagate waves from offshore regional scales to nearshore and port basin scales. Ship responses are quantified through the computation of six-degrees-of-freedom (DoF) response amplitude operators (RAOs) using a three-dimensional hydrodynamic panel model. Among the motion components, heave and pitch are the main contributors to the vertical displacement of the ship hull and govern the maximum vertical motion at the stern.

This numerical methodology has been implemented in the HIDRALERTA-SAFEPORT Operational Forecast and Early Warning System (EWS) for navigation safety. The Port of Aveiro is presented as a case study. Located in a rapidly developing economic region, the port is exposed to the energetic Atlantic wave climate and is experiencing increased activity related to offshore wind and marine renewable energy projects. The proposed methodology enhances navigational safety and accessibility in ports exposed to energetic seas and supports more resilient and competitive port operations, particularly through the development and application of operational early warning systems.

2 SAFEPORT EARLY WARNING SYSTEM FOR NAVIGATION IN PORTS

2.1 *General Structure*

An effective Early Warning System (EWS) must be capable of predicting both the occurrence and the severity of hazardous events. Such systems reduce port vulnerability by enhancing planning capabilities and enabling timely and efficient responses to emergency situations. The SAFEPORT system—*Safety System for Manoeuvring and Moored Ships* (Pinheiro et al., 2020, 2022)—is an integral component of the HIDRALERTA EWS, which operates on a daily basis to issue emergency alerts related to wave overtopping, ship navigation safety, and operational constraints affecting port activities. The system currently covers seven ports and coastal zones in mainland Portugal, as well as three ports in the Azores Islands.

SAFEPORT employs a suite of numerical models running in near real time to simulate wave propagation and to compute ship motions and mooring forces. The modelling framework uses forecasts of offshore regional wind and wave conditions, combined with astronomical tidal data, as input to the numerical simulations. These simulations produce 3-hourly forecasts for a 3-day prediction horizon, which are subsequently evaluated against predefined operational and safety thresholds.

A probabilistic assessment of threshold exceedance is then performed to determine risk levels. Based on the forecasted risk, potential emergency situations and operational limitations can be anticipated in advance, enabling the timely issuance of appropriate warning alerts to support safe and efficient port operations.

The current architectural framework of the system is illustrated in Figure 1 and consists of five main modules.

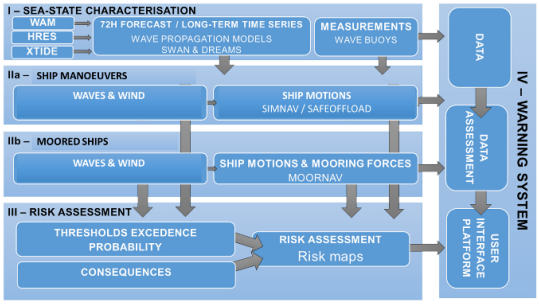

Figure 1. SAFEPORT-EWS architectural framework incorporating neural-network (NN) modelling.

2.2 *Module I – Sea-state characterisation.*

In this module, sea-state characteristics, water levels, and wind conditions are defined. The system employs a suite of numerical models that utilise forecasts of offshore wind and wave conditions, in conjunction with astronomical tide information.

Offshore wave and wind conditions, both hindcast and forecast, are provided by the European Centre for Medium-Range Weather Forecasts (ECMWF) and the Copernicus Marine Environment Monitoring Service (CMEMS). A 3-day forecast of offshore sea-state and wind conditions is downloaded daily from ECMWF's High-Resolution Forecast (HRES) system, which currently operates at a horizontal resolution of approximately 9 km. HRES provides detailed atmospheric predictions up to 3.5 days ahead and is updated twice daily, at 06 UTC and 18 UTC.

HRES is tightly integrated with two key numerical models:

- ECWAM (the ECMWF implementation of the WAM wave model; WAMDI, 1988), used to simulate and forecast wind-generated waves and sea-state conditions;
- NEMO (Nucleus for European Modelling of the Ocean), a dynamic ocean circulation model that supports the simulation of ocean currents and ocean–atmosphere interactions, particularly relevant for the development and tracking of tropical storms.

The ECWAM model provides predictions of the following wind and wave parameters:

- significant wave height (H_s),

- mean wave period (T_m),
- peak wave period (T_p),
- mean wave direction (θ_m),
- wind velocity components (V_x, V_y).

The spatial resolution of the ECMWF HRES wave and wind fields is 0.1° × 0.1°.

To complement the meteorological and oceanographic data, astronomical tide levels are computed using the XTide software (Flater, 1998), which implements the harmonic tide prediction algorithm of the U.S. National Ocean Service (NOS).

Wave propagation from offshore to nearshore regions is simulated using a nested modelling approach. The third-generation spectral wind-wave model SWAN (Booij et al., 1996) is applied at the regional scale to propagate wave conditions from the open ocean to the vicinity of the harbour. Simulations are carried out over several hundred kilometres around the study area using three nested computational grids with progressively finer spatial resolution.

SWAN is operated in stationary mode and includes key physical processes such as wave refraction, approximate diffraction, whitecapping, bottom friction, and depth-induced breaking. Due to the simplified representation of diffraction in SWAN, higher-resolution models are required for harbour-scale analysis.

For wave propagation into sheltered port basins, two local-scale models are employed: the mild-slope refraction–diffraction model DREAMS (Fortes, 2002) and the non-linear Boussinesq-type model BOUSS-WMH (Pinheiro et al., 2011). These models resolve complex wave transformations and harbour resonance phenomena, providing detailed sea-state information required for moored-vessel motion analysis.

Numerical simulations are executed on the National Distributed Computing Infrastructure (INCD), using a high-performance computing cluster with 64 nodes. A finite-element mesh generator supports the implementation of local-scale models, ensuring adequate spatial resolution for irregular coastal and port geometries. The runtime of a complete forecast cycle is approximately 30–40 minutes, as the 24 forecast instants are computed in parallel using 24 cluster nodes. Most of the computational time is associated with the high-resolution harbour-scale wave propagation model (DREAMS).

2.3 *Module II – Ship Manoeuvring and Mooring Safety*

The wind and sea-state conditions derived from Module I are used to assess: a) Ship manoeuvring safety, through the numerical evaluation of dynamic under-keel clearance (UKC) along approach routes; b) Mooring safety, including ship motions and forces acting on mooring lines and fenders, evaluated using the *Simulation of Wave Action on Moored Ships* (SWAMS) software (Santos, 1994; Pinheiro et al., 2013).

The central contribution of this paper is a novel methodology for assessing manoeuvring safety based on time-domain simulations of ship motions and dynamic UKC, as described in Section 3.

For moored-ship safety assessment, the SWAMS model computes vessel response to wave and wind loading. It integrates a three-dimensional hydrodynamic panel method (WAMIT; Korsmeyer et al., 1988) with a time-domain motion solver (BAS; Mynett et al., 1985), enabling dynamic modelling of ship behaviour. The system resolves the equations of motion using time series of environmental loads in combination with the mechanical properties of the mooring system.

2.4 *Module III – Risk assessment*

Simulated hourly ship motions and mooring line tensions are evaluated against predefined operational thresholds. Risk levels are quantified by comparing the model outputs with the maximum breaking load (MBL) of mooring lines, in accordance with OCIMF recommendations (OCIMF, 1992), and with allowable ship motion limits based on PIANC guidelines (PIANC, 1995, 2012).

2.5 *Module IV – Warning system*

This module generates and disseminates 72-hour forecasts, updated daily through a web-based platform, and issues daily bulletins containing alerts related to wave overtopping, moored-ship safety, and under-keel clearance (UKC). These bulletins are distributed via email to the relevant port authorities and stakeholders.

A four-tier alert system is implemented to communicate operational risk levels:

- Level 0 – Green: Normal operations; no restrictions.
- Level 1 – Yellow: Conditional operations; reinforcement of moorings recommended.
- Level 2 – Orange: Operations suspended; mooring reinforcement required.

- Level 3 – Red: Operations halted; high risk of mooring failure or structural damage.

The alert levels are represented using colour-coded indicators to support rapid decision-making by port operators with respect to loading and unloading activities, navigational safety, and mooring integrity.

3 METHODOLOGY

3.1 *Ship Manoeuvring Safety*

The proposed numerical methodology, based on the under-keel clearance (UKC) criterion, was developed to accurately assess ship accessibility and navigational safety. It combines the simulation of non-linear wave propagation and transformation in complex, sheltered environments—such as ports—with three-dimensional hydrodynamic flow around the ship hull, accounting for wind and current effects. This methodology can be applied both during the planning phase and operationally to support port management decisions.

A set of numerical models is used to propagate waves from the regional scale to the local scale. This modelling chain consists of the SWAN model (Booij et al., 1996), coupled with either a non-linear Boussinesq-type model (Pinheiro et al., 2011) or a linear mild-slope model (Fortes, 2002), depending on the required spatial resolution and physical processes.

The ship's response amplitude operators (RAOs) for the six degrees of freedom (6DoF) are then computed using a three-dimensional hydrodynamic panel method (Korsmeyer et al., 1988).

Heave and pitch are the main contributors to the vertical motion of the ship hull (Figure 2). The combination of these two motion components for each wave frequency yields the maximum vertical displacement of the stern, Δz, given by:

$$\Delta z = \Delta X_3 + \Delta X_5$$

where ΔX_3 is the vertical displacement of the ship's centre of gravity and $\Delta X_5$is the vertical displacement of the stern due to pitch rotation, expressed as:

$$\Delta X_5 = \frac{LOA}{2} \sin X_5$$

where LOA is the ship's length overall.

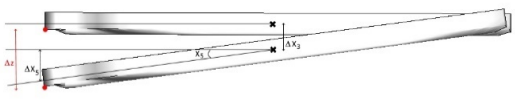

Figure 2. Motion amplitude of the ship hull.

This is followed by an assessment of the expected UKC given by:

$$UKC = D - d_1 - d_2 - \sum_{i=3}^{5} d_i - \sum_{i=6}^{9} d_i$$

Where:

D - is the local depth (varying with tide level);

$d_1 = \Delta z$ – is the draft of the ship (varying with ship loading);

d_2 – is the maximum vertical ship motion induced by waves;

d_3 – is the difference in draft between stern and bow (trim), dependent on ship loading;

d_4 – is the squat induced by current effects;

d_5 – is the set-down due to atmospheric pressure variations

d_6 – is a safety margin;

d_7 – is a tolerance accounting for measurement uncertainties;

d_8 – is a tolerance accounting for sediment accretion between dredging operations;

d_9 – is a tolerance accounting for dredging inaccuracies.

3.1.1 *Channel Design Based on Manoeuvring Safety Criteria*

During the planning phase of port development, the minimum safe depths and widths of entrance channels can be defined based on the local wave climate and the characteristics of vessels calling at the port. Using numerical wave propagation models, offshore wave conditions are transferred to a set of key locations along the access channel. This process enables the identification of the operational wave envelope—typically represented by peak period versus significant wave height (T_p–$H_{s,\max}$) pairs—under which the under-keel clearance (UKC) criterion must be satisfied.

The impact of wave conditions on the six-degrees-of-freedom (6DoF) ship motions is evaluated using three-dimensional hydrodynamic simulation tools. The maximum vertical ship motion at each location along the channel is determined by analysing the most critical combinations of wave parameters (T_p, $H_{s,\max}$, and wave direction). This approach defines the worst-case scenario for UKC compliance.

Alternatively, a required operability level—defined as the percentage of time during which port access must be ensured—can be specified. Based on this criterion, the minimum channel dimensions required to satisfy UKC

requirements under the expected wave regime can be systematically determined.

3.1.2 *Operational safety conditions*

During the operational phase, the same methodology applied in the planning stage can be used to assess the safety conditions for a specific vessel navigating into or out of the port. This assessment is based on short-term forecasts of offshore wind and wave conditions, combined with sea-level information. By applying numerical models to propagate the forecasted sea states into the port domain, ship motions and under-keel clearance can be evaluated along the intended navigation route.

This methodology forms the basis of the Operational Forecast and Early Warning System (EWS) for navigation safety, initially developed for the Port of Sines (Pinheiro et al., 2023) and currently being extended to additional locations, including the Port of Aveiro, within the framework of the C2Impress project (Co-creative Improved Understanding and Awareness of Multi-Hazard Risks for a Disaster-Resilient Society; www.c2impress.com).

The primary objective of the EWS is to reduce port vulnerability by enhancing situational awareness, improving planning capabilities, and enabling timely responses to adverse environmental conditions. In doing so, the system contributes to both navigational safety and port competitiveness by minimising disruptions to vessel traffic and operational activities.

4 CASE STUDY: PORT OF AVEIRO

The Port of Aveiro, located on the north-west coast of mainland Portugal, is a key hub for general cargo, containerised freight, and bulk transport. This case study illustrates the application of the proposed numerical methodology during both the planning and operational phases of port access management.

4.1 *Planning Phase: Channel Design and Ship Manoeuvring Safety*

During the planning phase, the methodology was applied to assess the minimum safety dimensions required for the entrance channel, based on the local wave climate and representative vessel characteristics. Offshore wave conditions derived from long-term hindcast datasets were propagated to key locations along the access channel using the SWAN model. This enabled the definition of the operational wave envelope, represented by T_p–$H_{s,\max}$ pairs, corresponding to the most critical sea states under which navigation must remain safe.

Figure 3 compares the current bathymetry (left panel) with the planned dredging configuration (right panel), designed to improve channel depth and safety margins. These modifications are expected to significantly influence wave transformation patterns and vessel manoeuvrability within the access channel.

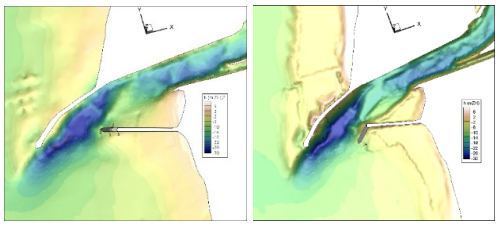

Figure 3. Present (left) and planned (right) bathymetry

Using three-dimensional numerical ship-motion models (WAMIT and BAS), the six-degrees-of-freedom (6DoF) responses of a representative container vessel were evaluated at multiple locations along the channel. Maximum vertical motions associated with worst-case wave combinations were used to verify compliance with under-keel clearance (UKC) criteria under operational conditions. The results informed recommendations for minimum channel depth and width, either for extreme scenarios or to achieve a specified operability target (e.g. 95% annual accessibility).

The ship's 6DoF response amplitude operators (RAOs) were computed using a 3D hydrodynamic panel method (Korsmeyer et al., 1988), as illustrated in Figure 6.

Figure 4 shows the wave transformation patterns along the port's access channel simulated with the DREAMS model. The results highlight the refraction and diffraction processes governing wave propagation into the channel, which are critical for assessing nearshore wave conditions relevant to vessel navigation.

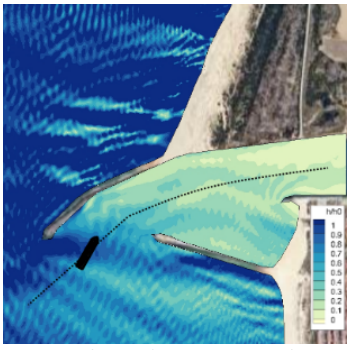

Figure 4. Wave transformation patterns along the access channel simulated with the DREAMS model.

Accurate prediction of ship motions requires detailed modelling of wave–ship hydrodynamic interaction.

Figure 5 presents the discretisation of the vessel hull into panels, forming the basis of the three-dimensional boundary element method used in the hydrodynamic simulations. This panelisation enables precise computation of wave-induced forces and moments acting on the vessel.

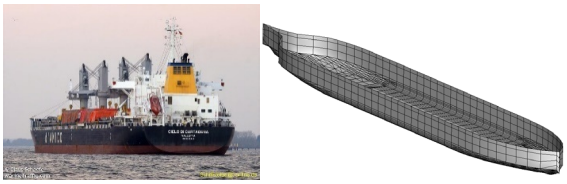

Figure 5. Ship hull panel discretisation.

The resulting ship motion response to wave forcing is characterised by the amplitude of hull motions, revealing spatial variations that influence overall vessel behaviour under different sea states.

To quantify this response, Figure 6 presents the RAOs for the two dominant vertical motion components—heave (X_3) and pitch (X_5)—for a general cargo vessel. These RAOs describe the ship's response across wave frequencies and are essential for estimating vertical motions affecting UKC.

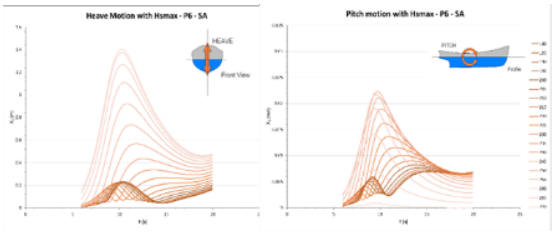

Figure 6. Heave (X_3) and pitch (X_5) RAOs for a general cargo vessel.

Environmental forcing conditions in the study area are summarised in Figure 7, which depicts the prevailing wind and wave regimes affecting the Port of Aveiro.

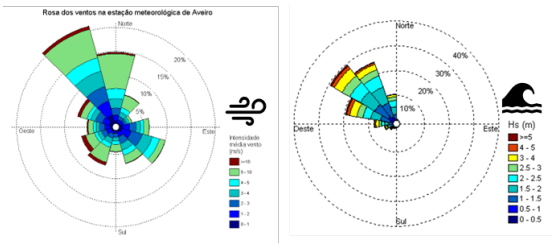

Figure 7. Wind and wave regimes.

Based on the joint distribution of significant wave height (H_s) and mean wave period (T_m) for the period from 1 January 1979 to 17 December 2020, the maximum $H_s$values associated with each $T_m$were identified (red circles in the first panel of

Figure 8). A third-degree polynomial was then fitted using a minimum root mean square error criterion, defining the maximum wave-height envelope as a function of wave period along the access channel and within the harbour.

This envelope was derived for both the current configuration (SA) and an alternative layout (ALT14).

Figure 8 shows the joint H_s–T_m distribution at monitoring point P6, comparing the present configuration (blue) with a hypothetical scenario involving a 200-m rotation of the south breakwater head (yellow). The red dots delineate the operational wave envelope).

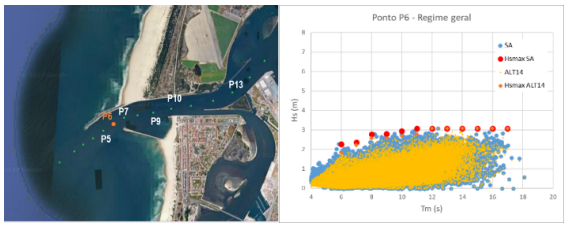

Figure 8. –T_m distribution at point P6. Red dots represent the envelope of maximum $H_s$for each T_m; blue indicates the current configuration (SA), and yellow the modified configuration (ALT14).

The effects of these wave conditions on the vessel's 6DoF motions were computed using the three-dimensional ship hydrodynamic models. The maximum vertical motion of the ship, resulting from the most unfavourable combination of wave parameters (T_p, $H_{s,\max}$, direction), was assumed to represent the worst-case scenario at each point along the channel.

Figure 9 presents the maximum vertical displacement of the vessel's stern (Δz) under two wave condition sets. The left panel includes all wave records, representing the full variability of the local sea state, including extreme conditions. The right panel considers operational harbour conditions only, defined here as $H_s < 3.0$m at the harbour entrance (point P1). The comparison demonstrates a substantial reduction in vertical motions during normal operational conditions, highlighting the importance of wave filtering in UKC assessments.

Using the computed vessel motions and local bathymetry, the minimum UKC along the vessel route was calculated.

Figure 10 shows the resulting minimum UKC values under wave forcing. These results identify potential bottlenecks within the access channel or harbour basin where safety margins may be insufficient, particularly during low tide or elevated wave conditions.

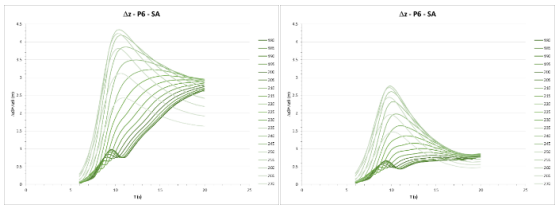

Figure 9. Maximum vertical displacement of the stern (Δz). Left: all wave records; right: operational harbour conditions ($H_s < 3.0$ m).

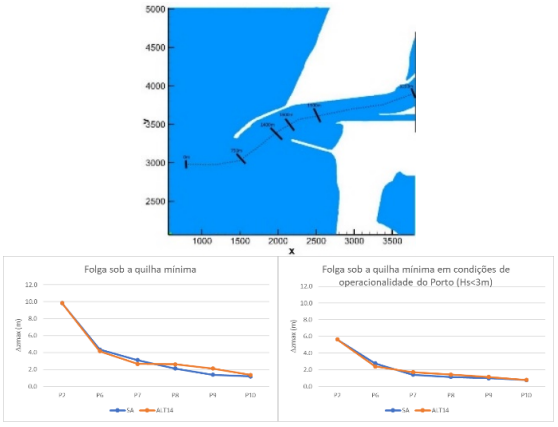

Figure 10. Minimum under-keel clearance under wave action.

Alternatively, an operability level—defined as the percentage of time that port access must be guaranteed—can be specified, and the corresponding minimum channel dimensions required to satisfy UKC criteria can be derived.

Figure 11 presents the average annual number of days at point P6 when $H_s$exceeds predefined operational thresholds, for both the current configuration (SA) and the planned configuration (ALT14). The results indicate that extending the south breakwater leads to a noticeable reduction in wave energy entering the channel, thereby improving operability by reducing the number of days with unsafe navigation conditions.

This information provides a key input for cost–benefit analyses of infrastructure upgrades, supporting decisions on dredging strategies, breakwater optimisation, and port accessibility targets (e.g. achieving 95% annual operability).

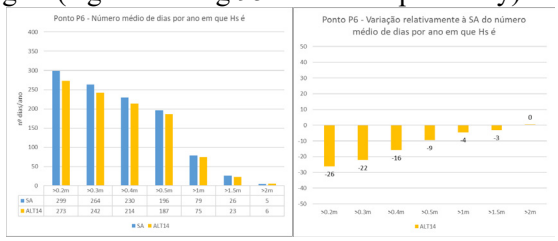

Figure 11. Average number of days per year at point P6 when $H_s$exceeds defined thresholds, for the present (SA) and planned (ALT14) configurations.

4.2 *Operational Phase: Forecast-Based Safety Assessment*

During the operational phase, the same modelling framework supports a real-time Early Warning System (EWS) that provides dynamic assessments of navigational safety. The EWS ingests daily forecasts of wind, wave, and sea-level conditions from ECMWF and CMEMS and propagates these conditions through nested computational grids down to the port entrance using the SWAN and DREAMS models.

For the Port of Aveiro, a representative container vessel scenario was simulated under a forecasted moderate storm event. Ship motions and under-keel clearance (UKC) were evaluated for both inbound and outbound routes. In this case, red alerts were issued for a six-hour time window along two segments of the vessel's route (see figures 12 and 13).

This application, developed within the C2Impress project, demonstrates how operational numerical modelling enhances port resilience by providing actionable information to support harbour master decision-making. The system enables real-time risk evaluation, optimises berth scheduling, and minimises operational downtime associated with uncertain or rapidly changing weather conditions.

Forecast data on sea states and tidal levels are dynamically integrated into the EWS to assess navigation safety conditions in near real time. This includes the continuous evaluation of UKC along the vessel's route and the issuance of risk-based alerts to guide operational decisions.

Figure 12 presents an alert map for the entrance channel of the Port of Aveiro, generated using forecasted wave and sea-level data. The map provides a spatial representation of navigational risk levels along the channel, using a colour-coded scale to highlight critical zones where UKC may be compromised. This visualisation supports operational planning by

indicating when and where transit restrictions should be considered for safety reasons. Complementarily, Figure 13 shows the forecasted UKC along the entrance channel, illustrating the temporal evolution of the clearance margin under the combined effects of bathymetry, tidal variation, and wave-induced vertical ship motions. This information allows the identification of safe navigation windows for both incoming and departing vessels.

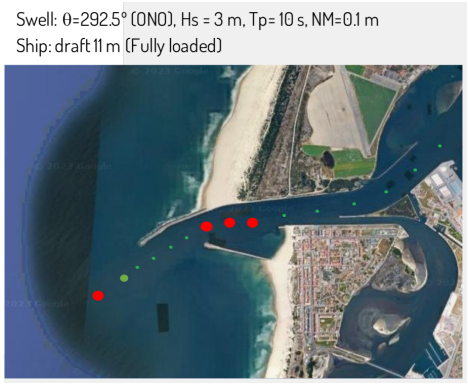

Figure 12. Alert map for the entrance channel of the Port of Aveiro

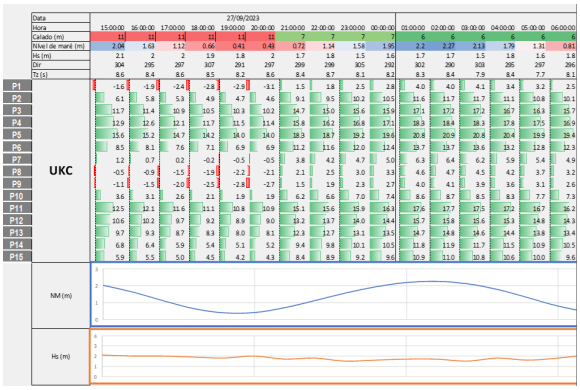

Figure 13. Under-keel clearance forecast for the entrance channel

5 CASE STUDY: PRAIA DA VITÓRIA

5.1 *Operational Phase: Forecast-Based Moored Ships safety*

The Port of Praia da Vitória is located on the eastern coast of Terceira Island, in the Azores archipelago, Figure 14. Wave propagation from offshore to nearshore regions is simulated using the SWAN model, implemented through a nested grid system with three spatial resolutions: 200 m (coarse), 100 m (medium), and 25 m (fine). Outputs from the finest grid are subsequently used as input to the DREAMS model, which resolves local wave transformations within the port basin.

Figure 14. Praia da Vitória Port. Aerial views of the port and the container ship quay.

For the simulation of moored ship response, the WAMIT and BAS models are applied, requiring a detailed definition of vessel characteristics and mooring system parameters. The prototype vessel considered is a generic container ship with a displacement volume of 12,717 m³, a length overall of 120 m, a beam of 19 m, and a draft of 8 m. The vessel is moored at a berth with a water depth of 10 m.

The mooring system consists of ten mooring lines and five pneumatic fenders. Each mooring line has a Maximum Breaking Load (MBL) of 931 kN and an elongation capacity of 8%. The fenders exhibit a maximum reaction force of 4,900 kN at a deflection of 1 m. This configuration ensures adequate resistance to the dynamic loads imposed by wave and wind action during both berthing and operational conditions.

The prototype harbour layout includes two main terminals: the multipurpose terminal (quay 12) and the container terminal (quay 10). Two vessel types—a general cargo ship and a container ship—are modelled using the described mooring arrangements. The mooring configurations for both vessels, comprising ten mooring lines and five fenders each, are illustrated in Figure 15.

The prototype system for the Praia da Vitória harbour includes the multipurpose terminal, quay 12, and the container terminal, quay 10. Two ships are modelled – a general cargo ship and a container ship. The mooring arrangement of each ship, comprising 10 mooring lines and 5 fenders, is shown in Figure 15.

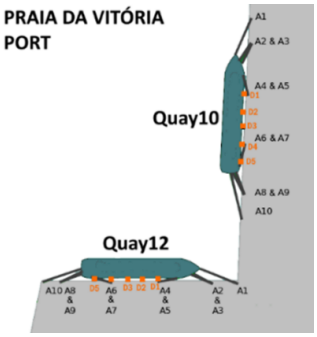

Figure 15. Mooring arrangements at quays 10 and 12.

A representative scenario illustrating system performance is presented for Hurricane Lorenzo. Forecasted mooring forces, significant wave height, and wind speed are shown in Figure 16 and form the basis for the risk-based alert system. The corresponding alert maps for the most critical hour are presented in Figure 17, highlighting the spatial distribution of mooring safety levels throughout the port.

With respect to mooring forces acting on the simulated vessels, no critical warnings were triggered during Hurricane Lorenzo. Mooring loads remained within the operational limits of the mooring system, indicating stable conditions for the prototype ships. Only Level 1 (yellow) alerts were issued, limited to the period between 03:00 and 06:00 UTC, primarily due to elevated wind speeds and wave heights. These conditions did not pose a significant risk to mooring integrity or overall operational safety.

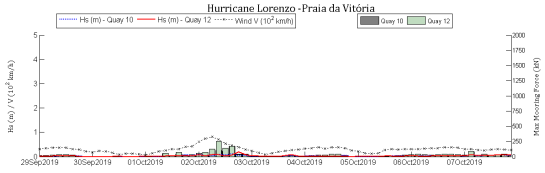

Figure 16. Hurricane Lorenzo: forecasted mooring forces, significant wave height, and wind speed.

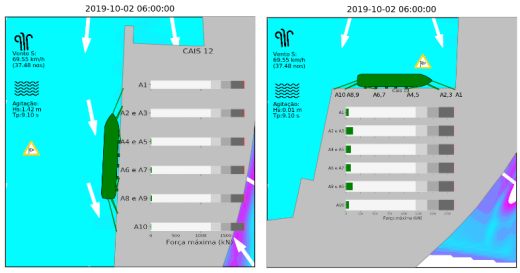

Figure 17. Hurricane Lorenzo alert maps for the critical hour.

6 CONCLUSIONS

The integration of medium-range wave forecasts with high-resolution numerical models for wave propagation enables the daily prediction of potentially hazardous sea states affecting coastal areas, port infrastructure, moored vessels, and port operations. This represents a significant advancement over traditional Early Warning Systems (EWSs), which typically rely solely on general sea-state parameters such as significant wave height and wave period.

Port and vessel safety are governed by complex wave–structure and wave–ship interactions, and associated risk assessments often require site-specific, dynamic modelling approaches. The HIDRALERTA system addresses this need by providing risk levels based on the actual physical impacts of forecasted waves on critical infrastructure and moored ships, rather than relying exclusively on environmental thresholds.

This impact-based approach enables port authorities and stakeholders to implement proactive mitigation strategies, enhancing personnel safety, preventing structural damage, and reducing operational downtime. By delivering real-time, actionable information, HIDRALERTA improves port resilience and preparedness in the face of extreme weather events, ultimately contributing to greater operational continuity and economic efficiency. In the case of Praia da Vitória, the EWS has been operational for more than five years, and feedback from pilots, port authorities, and civil protection services has been crucial for the ongoing fine-tuning and optimization of the system, particularly with respect to moored ship safety.

Complementing this framework, the newly proposed methodology for Under-Keel Clearance (UKC) assessment advances safety management for manoeuvring vessels during both the design and operational phases. In the design phase, the methodology combines numerical wave propagation and three-dimensional ship motion simulations to define minimum safety depths and widths for access channels based on the local wave climate and vessel characteristics. This ensures compliance with UKC criteria under the most critical wave conditions, thereby improving channel design reliability and operability.

During the operational phase, the same modelling framework integrates real-time forecast data to dynamically assess UKC and ship manoeuvring safety along navigation routes. This enables EWSs to issue timely alerts regarding access conditions, supporting informed decision-making, optimized vessel scheduling, and risk reduction. By explicitly linking environmental forecasts with ship dynamic response and clearance requirements, this methodology addresses a critical gap in maritime safety management.

Together, these developments support a holistic, physics-based approach to port safety, ensuring both infrastructure protection and safe vessel operations under variable and extreme sea conditions.

ACKNOWLEDGEMENTS

This work was supported by the LIFE-Garachico project *"Coastal Flooding Adaptation to Climate Change through Flexible Strategies in Macaronesia Urban Areas"* (co-financed by the EU LIFE Programme, LIFE20 CCA/ES/001641) and the C2IMPRESS project (funded by the European Union's Horizon Europe research and innovation programme under Grant Agreement No. 101074004).
The authors also acknowledge the collaboration of the Azorean and Aveiro Port Authorities *(Portos dos Açores and Administração do Porto de Aveiro)*, local authorities (Municipality of Praia da Vitória and the Regional Civil Protection Service of the Azores), the Portuguese Hydrographic Institute, and the Portuguese National Distributed Computing Infrastructure (INCD) for providing computational resources
.

REFERENCES

Auclair, Francis (2022) "Coastal and Regional Ocean COmmunity model". Zenodo. doi: 10.5281/zenodo.7415343.

Azevedo, E. B., Mendes, P., Gonçalo, V. 2008. Projectos CLIMAAT e CLIMARCOST Clima e Meteorologia dos Arquipélagos Atlânticos, Clima Marítimo e Costeiro, in Workshop Internacional sobre Clima e Recursos Naturais nos Países de Língua Portuguesa -WSCRA08.

Basher, R.E. (2006). Global early warning systems for natural hazards: systematic and people-centred. Philosophical Transactions of the Royal Society A: Mathematical, Physical and Engineering Sciences, 364, 2167 - 2182.

Booij, Holthuijsen, Ris, (1996). The SWAN wave model for shallow water. ICCE´96 Orlando, pp. 668-676.

Brownlee, J. (2019). How to Normalize and Standardize Time Series Data in Python. Available at: machinelearningmastery.com/normalize-standardize-timE-series-data-python (last visited on 05/2022).

BS 6349-1-1. (2013). "Maritime works – Part 1-1: General – Code of practice for planning and design for operations". The British Standards Institution 2013. Published by BSI Standards Limited 2013. ISBN 978 0 580 76228 4

Capitão, R., Fortes, C., (2011). A variabilidade das extrapolações do regime de extremos com a natureza das amostras: o caso de estudo do porto de vila do conde, in: 7as Jornadas Portuguesas de Engenharia Costeira E Portuária, 6 E 7 de Outubro de 2011. Porto, Portugal, p. 16.

Coeveld, E.M., van Gent, M.R.A. & Pozueta, B. (2005). "Neural Network: Manual NN_OVERTOPPING2". CLASH WP8 – Reharbour BV.

Cutter, S. L., Boruff, B. J., & Shirley, W. L. (2003). Social vulnerability to environmental hazards. *Social Science Quarterly*, 84(2), 242-261.
Distributions on Natural Beaches.
JCR7(4):1139-1152.

Dominguez, J., Resio, D. (2016). Statistical and machine learning methods in coastal inundation forecasting. *Journal of Marine Science and Engineering*, 4(2), 43.

Doong, D.-J & Chuang, L. & Wu, L.-C & Fan, Y.-M & Kao, C. & Wang, J.-H. (2012). Development of an operational coastal flooding early warning system. Natural Hazards and Earth System Sciences. 12. 379-390. 10.5194/nhess-12-379-2012.

Flater, D. (1998). *XTide Manual: Harmonic Tide Clock and Tide Predictor*. Technical Report, USA. URL: https://flaterco.com/xtide

Fortes, C.J.E.M. (2002) Non-linear wave transformations in ports. Analysis using the FEM. PhD thesis. Lisbon: IST/DEM

Fortes, C.J.E.M., Reis, M.T., Poseiro, P., Capitão, R., Santos, J.A., Pinheiro L.V., Craveiro J., Rodrigues, A., Sabino, A., Silva, S.F., Ferreira, J.C., Raposeiro, P.D., Silva, C., Rodrigues, M.C., Simões, A., Azevedo, E.B., Reis F. (2014). HIDRALERTA project – A flood forecast and alert system in coastal and port areas. *Proc. IWA World Water Congress & Exhibition 2014*, Shaping our Water Future, 21-26 September, Lisbon.

Garzon, J. L., Ferreira, A.M., Zózimo, A.C., Ferreira, Ó., Fortes, C.J.E.M. & Reis, M.T. (2022). *Early Warning System development: Quarteira and Praia de Faro*. http://dx.doi.org/10.34623/bdcs-3z27

Gracia, V., García-León, M., Sánchez-Arcilla, A., Gault, J., Oller, P., Fernández, J., Sairouní, A., Cristofori, E., & Toldrà, R. (2014). A new generation of early warning systems for coastal risk. The iCoast project. Coastal Engineering 2014 Proceedings, 1(34), management.18.
https://doi.org/10.9753/icce.v34.management.18.

Guza, R.T. e Thornton, E.B. (1982). Swash oscillations on a natural beach. J. Geoph. Res., 87 (C1), 483-491.

Holman, R.A. (1986). Extreme value statistics for wave run-up on a natural beach. Coastal Eng., 9, 527-544.

Hunt, I.A. (1959). Design of seawalls and breakwaters. J. of Waterways and Harbours Div., 85, 123-152.

International Strategy for Disaster Reduction. Platform for the Promotion of Early Warning. https://www.unisdr.org/2006/ppew/whats-ew/basics-ew.htm. Accessed on: 04/10/2022.

Korsemeyer, Lee, Newman, Sclavounos (1988). Analysis of wave effects on tension-leg platforms, *7th International Conference on Offshore Mechanics and Arctic Engineering*, Houston, Texas, pp. 1-14.

Lane, A., Hu, K., Hedges, T., & Reis, M.T. (2008). New north east of England tidal flood forecasting system. *Proceedings of FLOODrisk 2008, Flood Risk Management: Research and Practice*, 1377–1387.

Leitão, J. C., Leitão, P. C. Silva, A. Pedro Galvão, João Ribeiro, Madalena S. Malhadas, Hélio Santos, Eduardo Aires - João Lomba da Costa (2021) Sistema Aquasafe Nos Portos De Leixões E Viana Do Castelo. 8ªs Jornadas Portuguesas de Engenharia Costeira e Portuária. LNEC, 10 e 11 de Outubro de 2021.

Masatoshi, Y.; Naoya, O.; Mase, H.; Kim, S.; Umeda, S.; Altamore, C. (2019). Applicability enhancement of integrated formula of wave overtopping and runup modelling. Journal of JSCE, Ser. B2 (Coastal Engineering), 75. I_739-I_744. 10.2208/kaigan.75.I_739.

Mase, H.; Tamada, T.; Yasuda, T.; Hedges, T. S.; Reis, M.T. (2013). Wave runup and overtopping at seawalls built on land and in very shallow water. Journal of Waterway Port, Coastal, and Ocean Engineering, 139, 346–357.

Mileti, D. S., & Peek, L. P. (2000). *Shelter from the storm: Building community resilience for a changing climate*. Joseph Henry Press.

Mínguez, R., A. Espejo, A. Tomás, F. J. Méndez, and I. J. Losada, 2011: Directional Calibration of Wave Reanalysis Databases Using Instrumental Data. J. Atmos. Oceanic Technol., 28, 1466–1485, https://doi.org/10.1175/JTECH-D-11-00008.1.

Moore, A.M., J. Levin, and H.G. Arango, and J. Wilkin, 2021: Assessing the performance of an ocean observing, analysis and forecast System for the Mid-Atlantic Bight using array modes, *Ocean Modelling*, **164**, doi:10.1016/j.ocemod.2021.101821

Mynett, A.E., Keunig, P.J. e Vis, F.C. (1985). The dynamic behaviour of moored vessels inside a harbour configuration. *Int. Conf. on Numerical Modelling of Ports and Harbour* 23-25: Cranfield: BHRA. The Fluid Engineering Centre, April 1985. England: Birmingham.

Nielsen, P. & Hanslow, D.J. (1991). Wave Runup

OCIMF - Oil Companies International Marine (1992) *Mooring equipment guidelines*. Witherby e Co. Ltd.

Persson, A. (2001). *User Guide to ECMWF Forecast Products*. Meteorological Bulletin M3.2. ECMWF: 115.

PIANC - Permanent International Association of Navigation Congresses (1995*). Criteria for movements of moored ships in harbors*. Technical report Permanent International Association of Navigation Congresses. PIANC Supp.to bulletin no. 88.

PIANC (2014). "Harbour Approach Channels – Design Guidelines". MarCom WG 121.

PIANC. (2012). Guidelines for berthing structures related to thrusters. PIANC. Brussels, Belgium.

Pinheiro, C. J. Fortes, J. A. Santos, L. Fernandes, M. Walkley (2011) Finite Element Model for Wave Propagation Near Shore Based on Extended Boussinesq Equations. WSEAS Transactions on Fluid Mechanics. Issue 3, Volume 6, pp174-191. July 2011. ISSN: 1790-5087.

Pinheiro, Fortes, Reis, Santos, Guedes-Soares (2020): Risk Forecast System for Moored Ships. *Coastal Engineering Proceedings*, (36v), management.37.

Pinheiro, Fortes, Reis, Santos, Guedes-Soares (2022). Neural Networks for Optimization of An Early Warning System For Moored Ships In Harbors. *Coastal Engineering Proceedings*, (36v), management.37. https://doi.org/10.9753/icce.v36v.management.37.

Pinheiro, Fortes, Santos, Fernandes, (2013). Numerical software package SWAMS – Simulation of Wave Action on Moored Ships. *Proc. PIANC 3rd Mediterranean Days of Coastal and Port Engineering*, 22 a 24 de Maio, Marseille, France.

Pinheiro, L. V., Gomes, A. H., Fortes, C. J., & Santos, J. A. (2023). "Implementation and Validation of SAFEPORT System at Sines Harbour". In Defect and Diffusion Forum (Vol. 427, pp. 215–226). Trans Tech Publications, Ltd. DOI:10.4028/p-2sbfir

Pinheiro, L. V.; Fortes, C.J.E.M.; Santos, J.A.; Fernandes, L.; Walkley, M.A. (2011). Boussinesq-type Numerical Model for Wave Propagation Near Shore and Wave

Penetration in Harbors. 1st International Conference on Maritime Technology and Engineering, MARTECH 2011, IST, Lisbon, may 10-12, 2011

Poseiro, Gonçalves, Reis, Fortes, (2017) – Early warning systems for coastal risk assessment associated with wave overtopping and flooding. *Journal of Waterway, Port, Coastal, and Ocean Engineering*.

Poseiro, P.G.G. 2019. *Forecast and Early Warning System for Wave Overtopping and Flooding in Coastal and Port Areas: Development of a Model and Risk Assessment*, PhD Thesis, Instituto Superior Técnico, University of Lisbon, 502 pp.

Roelvink, D., Reniers, A., van Dongeren, A., van Thiel de Vries, J., McCall, R., & Lescinski, J. (2009). Modelling storm impacts on beaches, dunes and barrier islands, in Coastal Engineering, 56(11–12), 1133–1152.

ROM 3.1-99. (1999). "Proyecto de la configuración marítima de los puertos, canales de acceso y áreas de flotación". Puertos del Estado, Madrid.

Ruggiero, P., Komar, P.D., McDougal, W.G., Marra,J.J. e Beach, R.A. (2001). Wave Runup, Extreme Water Levels and the Erosion of properties backing beaches. J.C.R., 17, 407-419.

Sabino, A., Poseiro, P., Rodrigues, A., Reis, M.T., Fortes, C.J.E.M., Reis, R. & Araújo, J. 2018. Coastal Risk Forecast System, in *Journal of Geographical Syst*., 20(2), 159-184. https://doi.org/10.1007/s10109-018-0266-5

Santos, J. A. (1994). MOORNAV – *Numerical model for the behaviour of moored ships*. Final report, Lisbon: Report 3/94-B, Proj NATO PO-Waves.

Stockdon, H.F., Holman, R.A., Howd, P.A. e Sallenger Jr., A.H. (2006). Empirical parameterization of setup, swash, and runup. Coastal Eng., 53, 573-588.

Stokes, K., Poate, T., Masselink, G., King, E., Saulter, A., & Ely, N. (2021). Forecasting coastal overtopping at engineered and naturally defended coastlines. *Coastal Engineering, 164* (103827). https://doi.org/10.1016/j.coastaleng.2020.103827.

Teixeira, S.B. (2009). Demarcação do leito e da margem das águas do mar no litoral sul do Algarve. ARH Algarve. Faro.

Thoresen, C.A. (2003). "Port Designer's Handbook: Recommendations and Guidelines". Thomas Telford Limited, ISBN: 978-07277-3228-6.

Trotta, F., Federico, I., Pinardi, N., Coppini, G., Causio, S., Jansen, E., Iovino, D. and Masina, S. (2021). A Relocatable Ocean Modeling Platform for Downscaling to Shelf-Coastal Areas to Support Disaster Risk Reduction. Frontiers in Marine Science, 8, 317, https://doi.org/10.3389/fmars.2021.642815

van Dongeren, A., Ciavola, P., Martinez, G., Viavattene, C., Bogaard, T., Ferreira, O., Higgins, R., & McCall, R. (2018). Introduction to RISC-KIT: Resilience-increasing strategies for coasts, *Coastal Engineering, 134*, 2–9. https://doi.org/10.1016/j.coastaleng.2017.10.007

WAMDI Group (1988). The WAM Model - A third generation ocean wave prediction model. *J. Physical*

Zijlema, M., Stelling, G.S., Smit, P. (2011). SWASH: An operational public domain code for simulating wave fields and rapidly varied flows in coastal waters, in *Coastal Engineering*, 58(10), pp. 992–1012.

DOI: https://doi.org/10.53256/COSE_240105

Electrochemical Treatment of Membrane Cleaning Wastewater in Desalination and Drinking Water Treatment Plants: A Study on Free Chlorine Removal

K. Licht[a,*], K. Gulam[a], D. Vouk[a], I. Halkijevic[a]
[a]*Faculty of Civil Engineering, University of Zagreb, Zagreb, Croatia*

[*]*Corresponding author:* katarina.licht@grad.unizg.hr

ABSTRACT: Chemical cleaning of membranes in desalination and drinking water treatment plants generates wastewater characterized by high concentrations of free chlorine and elevated pH values. This study investigates the potential of electrocoagulation (EC) for the treatment of such effluents, with particular emphasis on the removal of free chlorine and its conversion to chloride ions. Experiments were conducted using synthetic wastewater representative of typical membrane cleaning solutions, employing iron and aluminium electrodes under varying current intensities (5, 10, and 15 A), treatment durations (up to 60 min), and pH conditions. The results demonstrate that EC effectively removes free chlorine, achieving up to 100% removal efficiency, particularly under neutral pH conditions. The conversion of free chlorine to chloride was confirmed by a corresponding increase in Cl^- concentrations. These findings highlight electrocoagulation as a promising and efficient method for the treatment of chlorine-rich membrane cleaning wastewater prior to discharge.

1 INTRODUCTION

The increasing global demand for clean and safe freshwater has led to the widespread adoption of membrane-based technologies in modern water and wastewater treatment facilities. Processes such as ultrafiltration (UF), nanofiltration (NF), and reverse osmosis (RO) are now essential components of both desalination and drinking water treatment plants. These technologies are highly effective in removing salts, organic pollutants, and microbial contaminants (Anwar et al., 2020). However, membrane systems are particularly vulnerable to fouling caused by organic matter, microbial growth, and inorganic scaling, which significantly reduces membrane permeability and overall operational efficiency (Maeda, 2024; Mahmoud et al., 2023).

To maintain membrane performance and extend service life, frequent cleaning-in-place (CIP) procedures are required. These procedures typically employ chemical cleaning agents such as sodium hypochlorite (NaOCl) for biofouling control and sodium hydroxide (NaOH) for the removal of organic deposits (Ang et al., 2011; Wang et al., 2011). As a result, CIP operations generate large volumes of chemically reactive wastewater characterized by high concentrations of free chlorine, elevated pH values, and strong oxidizing conditions (Saleh et al., 2016). If discharged without appropriate treatment, such effluents may pose serious environmental risks. Free chlorine and its transformation products, including chlorate and chlorite, are toxic to aquatic organisms and can cause persistent ecological damage in receiving water bodies (Deborde et al., 2008; Richardson et al., 2007).

Conventional treatment methods for CIP wastewater include chemical neutralization using reducing agents (e.g., sodium thiosulfate), pH adjustment, and dilution or mixing with municipal wastewater. Although these approaches can be effective, they are often associated with secondary pollution, increased sludge generation, and higher operational costs (Madaeni et al., 2007). Consequently, there is a growing need for alternative treatment strategies

that are both efficient and environmentally sustainable.

Electrocoagulation (EC) has emerged as a promising alternative technology for wastewater treatment. This process involves the application of an electric current to sacrificial metal electrodes, typically composed of iron or aluminium. The dissolution of the electrodes releases metal ions, which subsequently hydrolyse in water to form amorphous hydroxide flocs. These flocs remove contaminants through adsorption, destabilisation, complexation, and sweep flocculation mechanisms (Mollah et al., 2004). In addition, electrochemical reactions occurring at the anode and cathode can transform reactive chemical species, including free chlorine, into less harmful forms (Hakizimana et al., 2017; Ammar et al., 2023).

Numerous studies have demonstrated the effectiveness of EC in treating a wide range of wastewaters, including those containing heavy metals, suspended solids, organic pollutants, and disinfection by-products (Chen, 2004; Emamjomeh et al., 2009; Sahu et al., 2014; Tang, 2024). Electrocoagulation has also been applied in membrane-related systems, particularly for pretreatment and fouling control. For instance, in the food industry, the integration of EC with membrane filtration has achieved high removal efficiencies of chemical oxygen demand (COD) and proteins from detergent-rich CIP effluents (Ates et al., 2017). Despite these advances, research focusing specifically on the treatment of chlorine-rich CIP wastewater from drinking water and desalination plants using EC remains limited.

This study investigates the application of electrocoagulation for the treatment of synthetic membrane cleaning wastewater. The model wastewater simulates CIP effluents from a real water treatment plant, with NaOCl concentrations ranging from 0.05% to 0.25%. The primary objective is to evaluate the effectiveness of EC in removing free chlorine from this chemically aggressive wastewater. The influence of key operational parameters—namely current intensity, treatment duration, initial pH, and electrode material—on chlorine removal and overall treatment performance is also examined. In addition, the transformation of free chlorine into chloride ions is assessed. Ultimately, the study aims to determine whether electrocoagulation can serve as a practical and sustainable solution for managing membrane cleaning wastewaters in desalination and drinking water treatment facilities.

2 MATERIALS AND METHODS

2.1 *Experimental set-up*

This study was designed to evaluate the effectiveness of electrocoagulation (EC) in removing free chlorine from synthetic wastewater simulating membrane cleaning effluents generated in a drinking water treatment plant. All experiments were conducted in batch mode using a 10 L Plexiglas EC reactor (Fig. 1), equipped with six horizontally arranged iron (Fe) electrodes (three anodes and three cathodes) connected to a DC power supply. The inter-electrode distance was 1 cm, and the total surface area of each electrode was 9 cm^2. Continuous mixing was provided by an overhead mechanical stirrer to ensure solution homogeneity throughout each experimental run.

Two types of synthetic wastewater were prepared to represent typical membrane cleaning processes. The first solution, hereafter referred to as Solution A, consisted of 0.05% (w/v) NaOCl in tap water and simulated the daily backwashing of ultrafiltration membranes. The second solution, Solution B, contained 0.25% (w/v) NaOCl and 0.1% (w/v) NaOH, representing a more aggressive weekly chemical cleaning procedure. The initial physicochemical properties of the synthetic wastewaters are summarised in Table 1.

Table 1. Physicochemical characteristics of the simulated wastewaters

SOLUTION	pH	TDS, mg/L	Ƙ, µS/cm	Cl_2, mg/L	Cl^-, mg/L
A	8.25	976	1977	276	470
B	11.57	4230	6670	2400	1970

2.2 *EC treatment and analysis*

Electrocoagulation experiments were conducted under three direct current intensities: 5 A, 10 A, and 15 A, as summarised in Table 2. Samples were collected at 10-minute intervals over a total treatment duration of up to 60 minutes. In addition, secondary treatment of the effluent was performed after each experiment using aluminium (Al) electrodes for an additional 10 minutes to evaluate whether a sequential electrode configuration could enhance overall removal performance. In Experiment 7, the initial pH was adjusted to 7 to assess the influence of pH on electrochemical treatment efficiency.

Table 2. Experimental matrix

Run	Solution	Applied current
1	A	5 A
2	A	10 A
3	A	15 A
4	B	5 A
5	B	10 A
6	B	15 A
7	B, pH 7	15 A

The primary parameters monitored throughout the experiments were free chlorine (Cl_2) concentration, chloride (Cl^-) concentration, pH, temperature, electrical conductivity, and total dissolved solids (TDS). Free chlorine and chloride concentrations were determined using Nanocolor® colorimetric test kits in combination with a Nanocolor® 500D photometer. Physicochemical parameters were measured using a multiparameter probe (HI9829, Hanna Instruments).

All experiments were carried out under controlled laboratory conditions, following strict safety protocols, including the use of personal protective equipment and chemical fume extraction. Upon completion of each experiment, all treated solutions were neutralised with sodium thiosulfate ($Na_2S_2O_3$) prior to disposal.

The experimental data were used to calculate the percentage removal of free chlorine and the corresponding increase in chloride concentration as an indicator of chemical conversion. All experiments were performed in triplicate, and mean values were used to determine treatment efficiencies.

3 RESULTS AND DISCUSSION

3.1 *Efficiency of EC treatment*

Electrocoagulation (EC) demonstrated a high capacity for the removal of free chlorine (Cl_2) from synthetic wastewater simulating membrane cleaning effluents. Process efficiency was influenced by current intensity, treatment duration, initial pH, and wastewater composition. The efficiency of each experimental run, expressed as the percentage of free chlorine removed, is summarised in Table 3.

Table 3. Experimental results

Run	Solution	Current density	Treatment time	Efficiency
1	A	18 A/dm^2	50 min	100 %
2	A	37 A/dm^2	30 min	100 %
3	A	55 A/dm^2	20 min	100 %
4	B	18 A/dm^2	60 min	37.6 %
5	B	37 A/dm^2	60 min	79.8 %
6	B	55 A/dm^2	60 min	92.7 %
7	B , pH 7	55 A/dm^2	50 min	99.9 %

In experiments using the low-strength NaOCl solution (Solution A, 0.05%), free chlorine removal was rapid and nearly complete across all current intensities tested. At 5 A, more than 99% of Cl_2 was removed within 60 minutes, with concentrations decreasing from 276 to 0 mg L^{-1}, accompanied by a corresponding increase in chloride (Cl^-) from 470 to 550 mg L^{-1}. This indicates that electrochemical reduction of Cl_2 to Cl^- was the dominant removal mechanism, likely occurring at the cathode via electron transfer reactions.

Increasing the applied current intensity to 10 A and 15 A resulted in significantly faster chlorine removal. Complete removal was achieved in less than 30 minutes at 10 A and in less than 20 minutes at 15 A (Fig. 2), consistent with enhanced anodic dissolution and increased generation of coagulant species at higher current densities.

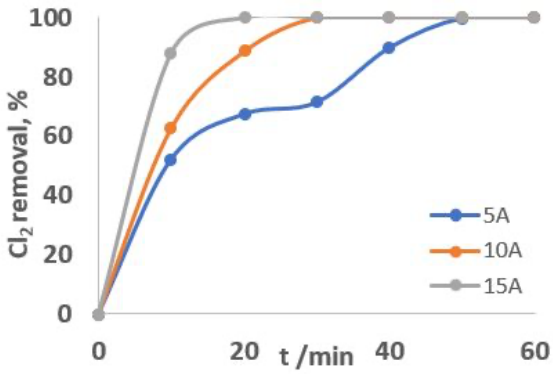

Figure 2. Efficiency of the EC process for experiments 1–3.

For the high-strength cleaning solution (Solution B, 0.25% NaOCl + 0.1% NaOH), initial free chlorine concentrations were substantially higher, reaching approximately 2400 mg L^{-1}. Under these conditions, chlorine removal was more challenging due to the strongly alkaline environment (pH > 11.5). In Experiment 6 (15 A, no pH adjustment), Cl_2 removal reached 92.7% after 60 minutes. However, when the initial pH was adjusted to neutral conditions, nearly

complete chlorine removal was achieved within the same treatment duration (Fig. 3.).

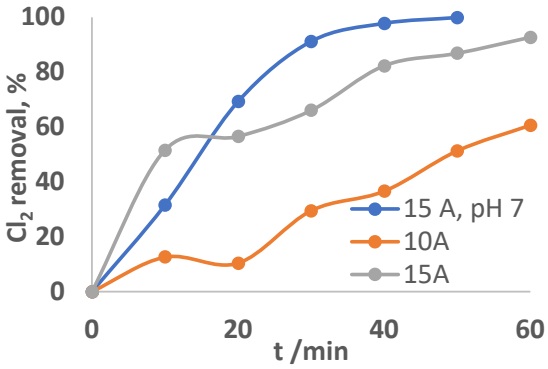

Figure 3. Efficiency of the EC process for experiments 5–7.

Under otherwise identical operating conditions (15 A, 10 L reactor volume, Fe electrodes), adjusting the initial pH to 7 resulted in a reduction of Cl_2 concentration from 2400 to 1.6 mg L^{-1}, corresponding to a removal efficiency of 99.93%. At neutral pH, metal hydroxide flocs exhibit enhanced destabilisation capacity, and electrochemical reduction reactions are thermodynamically more favourable. These findings are consistent with previous studies reporting improved EC performance under near-neutral pH conditions, owing to optimal coagulant speciation and surface charge characteristics (Mollah et al., 2004; Hakizimana et al., 2017).

3.2 *The mechanism of Cl_2 removal*

The removal of free chlorine during electrocoagulation (EC) is primarily governed by electrochemical reduction and associated chemical transformations occurring at the cathode surface. In aqueous solution, chlorine exists predominantly as hypochlorous acid (HOCl) and hypochlorite ions (ClO^-), with their relative proportions depending on the pH. Under near-neutral to alkaline conditions, ClO^- is the dominant species.

During EC, cathodic reactions facilitate the reduction of ClO^- to chloride ions (Cl^-). This reductive pathway is enhanced by increasing current density and extending reaction time, both of which increase the electron flux available at the cathode. In addition to electrochemical reduction, chlorine species may also be removed through adsorption onto in situ generated metal hydroxide flocs, such as $Fe(OH)_3$ or $Al(OH)_3$. This mechanism is particularly relevant under conditions that promote strong electrostatic interactions or sweep flocculation. Although adsorption is generally considered a secondary removal pathway, it may contribute significantly under specific conditions, such as elevated pH or excessive coagulant generation.

Importantly, the conversion of reactive and potentially hazardous chlorine species (e.g., Cl_2 and ClO^-) into chloride ions (Cl^-), which are considerably less toxic and more environmentally benign, highlights the suitability of EC for treating oxidative membrane cleaning wastewater. This reductive transformation is especially advantageous in preventing the formation of harmful disinfection by-products (DBPs) in downstream receiving waters.

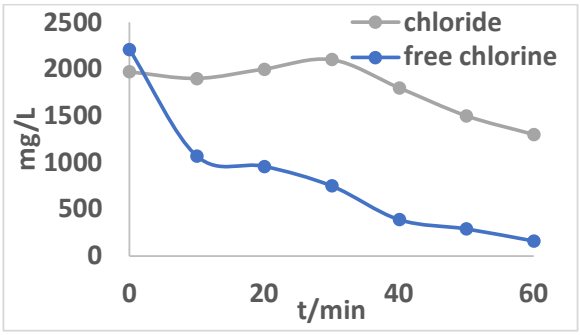

Figure 4. Changes in chloride and free chlorine concentrations during experiment 6

In all experiments, an increase in chloride ion concentration was observed, confirming the conversion of chlorine species to Cl^-. However, in some cases, as illustrated in Fig. 4, the chloride concentration began to decrease after reaching a maximum. This behaviour may be attributed to the entrapment or co-precipitation of Cl^- within the forming $Fe(OH)_3$ flocs.

This hypothesis is supported by previous studies reporting significant chloride removal during EC treatment of saline and industrial wastewaters. Wang et al. (2023) demonstrated that EC using aluminum electrodes can reduce chloride concentrations to below 250 ppm through mechanisms involving co-precipitation and electrostatic adsorption onto aluminum hydroxide flocs. They also reported that operational parameters, such as current density, electrode spacing, and the presence of competing ions, play a critical role in determining removal efficiency. Similarly, Al Raad et al. (2019) achieved up to 93% chloride removal from saline lake water using aluminum electrodes at a current density of 2 mA cm^{-2}, a reaction time of 80 minutes, and a pH of 8.

3.3 *Secondary treatment with Al electrodes*

After 60 minutes of primary electrocoagulation (EC) treatment using Fe electrodes, a secondary treatment step employing Al electrodes was performed to evaluate potential improvements in residual chlorine removal and overall water quality. The results indicate that post-treatment with Al electrodes did not result in a substantial additional removal of free chlorine, as chlorine concentrations were already close to or below the detection limit following Fe-based electrocoagulation.

Nevertheless, slight reductions in chloride concentrations were observed in some cases. This behaviour may indicate limited adsorption of chloride ions onto freshly formed $Al(OH)_3$ flocs or minor co-precipitation effects. In addition, the pH remained stable or exhibited a slight decrease during the aluminum treatment phase, likely due to the buffering effect associated with aluminum hydrolysis reactions.

Although no significant improvements in chlorine-related parameters were observed, aluminum post-treatment may offer benefits in practical applications involving real wastewaters, where additional removal of turbidity, residual organic matter, or colour is required. Further research is therefore needed to assess the full potential of sequential Fe–Al electrocoagulation in more complex matrices, particularly in wastewaters containing natural organic matter or disinfection by-products.

3.4 *Potential formation of disinfection by-products*

Although the present study focused on the removal of free chlorine, the potential formation of disinfection by-products (DBPs), such as trihalomethanes (THMs), haloacetic acids (HAAs), chlorates, and chlorites, remains an important consideration when treating chlorinated effluents. DBPs are typically formed through reactions between chlorine and natural organic matter (NOM), bromide, or ammonia—constituents commonly present in natural waters and membrane backwash streams (Richardson et al., 2007).

In this study, however, synthetic wastewater composed of NaOCl solutions prepared in tap water was used, without the addition of organic or nitrogenous compounds. Consequently, DBP formation was neither expected nor observed, and DBP-specific analyses were not performed. This approach is consistent with the characteristics of the real wastewater represented in this case study, as chemical analyses of treated samples indicated negligible organic content.

Nevertheless, the application of electrocoagulation to real membrane cleaning effluents—particularly those derived from brackish or surface water sources with elevated NOM or bromide concentrations—may lead to DBP formation prior to or during treatment. Future studies should therefore include systematic monitoring of relevant DBPs to fully assess the environmental safety and regulatory compliance of treated effluents, as well as to evaluate the potential role of electrocoagulation in mitigating or removing such by-products.

4 CONCLUSIONS

The results of this study demonstrate that electrocoagulation is an effective technology for the removal of free chlorine from membrane cleaning wastewater, particularly when the solution pH is adjusted to near-neutral values and appropriate current densities are applied. The consistent increase in chloride concentrations provides direct evidence of redox transformation, confirming the conversion of toxic free chlorine into less harmful chloride ions and thereby reducing the potential for disinfection by-product formation.

These findings highlight electrocoagulation as a promising alternative to conventional chemical neutralization methods for managing oxidative residues in desalination and drinking water treatment facilities. Future work should focus on the application of this approach to real wastewater streams and on its integration with complementary treatment processes to ensure full compliance with discharge regulations and environmental protection requirements.

ACKNOWLEDGEMENTS

This work was fully supported by the Croatian Science Foundation under project UIP-2020-02-1160 – *Purification of Microbiologically and Chemically Contaminated Drinking Water by Electrochemical and Ultrasonic Processes*.

REFERENCES

Al-Raad, A., Hanafiah, M.M., Naje, A.S., Ajeel, M.A., O. Basheer, A., Ali Aljayashi, T., Ekhwan Toriman, M. (2019). Treatment of Saline Water Using

Electrocoagulation with Combined Electrical Connection of Electrodes. *Processes* 7: 242. https://doi.org/10.3390/pr7050242

Ammar, M., Yousef, E., Mahmoud, M. A., Ashraf, S., Baltrusaitis, J. (2023). A comprehensive review of the developments in electrocoagulation for the removal of contaminants from wastewater. *Separations, 10(6):* 337. https://doi.org/10.3390/separations10060337

Ang W. S., Yip N. Y., Tiraferri, A., Elimelech, M. (2011). Chemical cleaning of RO membranes fouled by wastewater effluent: Achieving higher efficiency with dual-step cleaning. *Journal of Membrane Science, 382*: 100-106. https://doi.org/10.1016/j.memsci.2011.07.047.

Anwar, N., Rahaman, S. (2020). Membrane desalination processes for water recovery from pre-treated brewery wastewater: Performance and fouling, *Separation and Purification Technology,252:* 117420, https://doi.org/10.1016/j.seppur.2020.117420.

Ates, H., Ozay, Y., Dizge, N. (2017). Treatment of dairy-industry cleaning-in-place wastewater by electrocoagulation supported with immersed membrane process. *Clean - Soil, Air, Water, 45(11):* 1600654. https://doi.org/10.1002/clen.201600654

Chen, G. (2004). Electrochemical technologies in wastewater treatment, *Separation and Purification Technology,38(1):*11-41. https://doi.org/10.1016/j.seppur.2003.10.006.

Deborde, M., von Gunten, U. (2008). Reactions of chlorine with inorganic and organic compounds during water treatment - Kinetics and mechanisms: A critical review. *Water Research, 42(1–2)*: 13–51. https://doi.org/10.1016/j.watres.2007.07.025

Emamjomeh, M. M., Sivakumar, M. (2009). Review of pollutants removed by electrocoagulation and electrocoagulation/flotation processes. *Journal of Environmental Management, 90(5):* 1663–1679. https://doi.org/10.1016/j.jenvman.2008.12.011

Hakizimana, J. N., Gourich, B., Chafi, M., Stiriba, Y., Vial, C., Drogui, P., & Naja, J. (2017). Electrocoagulation process in water treatment: A review of electrocoagulation modeling approaches. *Desalination, 404*: 1–21. https://doi.org/10.1016/j.desal.2016.10.011

Maeda, Y. (2024). Fouling of Reverse Osmosis (RO) and Nanofiltration (NF) Membranes by Low Molecular Weight Organic Compounds (LMWOCs), Part 1: Fundamentals and Mechanism. *Membranes*, *14*(10): 221. https://doi.org/10.3390/membranes14100221

Madaeni, S. S., Ghaemi, N. (2007). Evaluation of self-cleaning RO membranes coated with TiO2 particles under UV irradiation. *Journal of Membrane Science 303:* 221-233. https://doi.org/10.1016/j.memsci.2007.07.017

Mahmoud A. A., Sherif A., Ashraf A. M. (2023). Fouling in reverse osmosis membranes: monitoring, characterization, mitigation strategies and future directions, *Heliyon 9(4):* 14908. https://doi.org/10.1016/j.heliyon.2023.e14908.

Mollah, M.Y.A., Schennach, R., Parga, J.R., Cocke, D.L. (2004). Electrocoagulation (EC) - Science and applications. *Journal of Hazardous Materials, 114(1–3)*: 199–210. https://doi.org/10.1016/j.jhazmat.2004.08.009

Richardson, S.D., Plewa, M.J., Wagner, E.D., Schoeny, R., DeMarini, D.M. (2007). Occurrence, genotoxicity, and carcinogenicity of regulated and emerging disinfection by-products in drinking water: A review and roadmap for research. *Mutation Research/Reviews in Mutation Research, 636(1–3):* 178–242. https://doi.org/10.1016/j.mrrev.2007.09.001

Sahu O., Mazumdar B., Chaudhari P.K. (2014). Treatment of wastewater by electrocoagulation: a review. *Environmental Science and Pollution Research International, 21(4):* 2397-413. https://doi.org/10.1007/s11356-013-2208-6

Saleh, A., Gupta, V.K. (2016). Membrane Fouling and Strategies for Cleaning and Fouling Control. *Nanomaterial and Polymer Membranes, 27:* 25-53, https://doi.org/10.1016/B978-0-12-804703-3.00002-4.

Tang, G. (2024). A literature review of electrocoagulation integrated systems on wastewater treatment. T*heoretical and Natural Science, 47(1)*: 102–109. https://doi.org/10.54254/2753-8818/47/20240169

Wang, Z., An, X., Wang, P. (2023). Removal of high concentration of chloride ions by electrocoagulation using aluminium electrode. *Environmental Science and Pollution Research, 30*: 50567–50581 https://doi.org/10.1007/s11356-023-25792-1

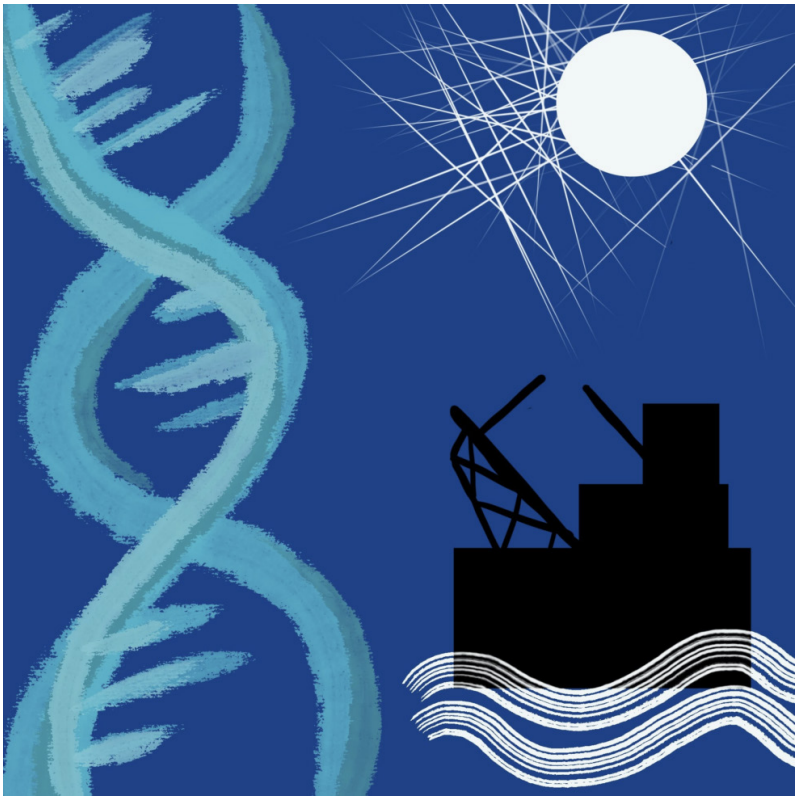

Concept:
Stefano Pagliai

Cover credits:
Cover image by ©**Marialuisa Sabato**

Web-site
https://www.ecampusuniversitypress.it/riviste/coastal-and-offshore-science-and-engineering/

Contact
editore@uniecampus.it

Publisher
Studium Srl
via Matera, 18 – 00182 – Roma
via Isimbardi, 10 – 22060 – Novedrate (CO)
www.studiumeditore.it

Registration with the Court of Como n. 2, March 7, 2022.

Coastal and Offshore Science and Engineering

an International open-access Journal

4/2024
ISSN 2785-7972

STUDIUM EDITORE

eCAMPUS UNIVERSITÀ

eCAMPUS UNIVERSITY PRESS